November 2022

Reducing Instrumentation Barriers of Diffuse Correlation Spectroscopy for Low-Cost Deep Tissue Blood Flow Monitoring

Arindam Biswas
University of South Florida

Reducing Instrumentation Barriers of Diffuse Correlation Spectroscopy for Low-Cost Deep Tissue Blood Flow Monitoring

by

Arindam Biswas

A dissertation submitted in partial fulfillment
of the requirements for the degree of
Doctor of Philosophy
Department of Electrical Engineering
College of Engineering
University of South Florida

Major Professor: Ashwin B. Parthasarathy, Ph.D.
Arash Takshi, Ph.D.
Stephen E. Saddow, Ph.D.
Andrew Hoff, Ph.D.
W. Scott Burgin, M.D.
John Murray-Bruce, Ph.D.

Date of Approval:
November 23, 2022

Keywords: Cerebral blood flow (CBF), Wearable hemodynamic, Near-infrared spectroscopy (NIRS), Laser speckle contrast imaging, Multi-exposure speckle imaging

Dedication

To my parents Archana Sarker & Milon Kumar Biswas and my loving wife Sweety Sarker Sristy.

Acknowledgments

My doctoral degree is the most critical milestone in my professional and personal life. I couldn't have finished it without the help of my mentors, friends, and family. Throughout my journey, I received extensive support from the department of Electrical Engineering at the University of South Florida. I am forever grateful for their support.

I would like to extend my cordial gratitude toward my supervisor Dr. Ashwin B. Parthasarathy, without whom this journey wouldn't have been possible with such ease. I am grateful to him for his guidance, teaching, research financial support and friendly advice on life. I would also like to extend my gratitude to my committee member, Dr. Arash Takshi, for his extensive help regarding my thesis project. I want to thank Dr. Stephen Saddow, Dr. Andrew Hoff, Dr. John Murray-Bruce and Dr. William Burgin for their guidance and time during the coursework and my dissertation. It is a privilege to be able to present my work in front of these prestigious scholars.

Working with the research group at TROPICS lab at USF was enjoyable. My lab mates' day-to-day support and humor have helped me get through academic and research challenges. I am blessed to have colleagues who also became excellent friends in life. I want to thank Penaz Parveen for her help during the *in-vivo* experiments. I thank Sadhu Moka and Abdul Mohaimen Safi for helping me characterize the laser systems and phantom preparation. I want to acknowledge the extensive experimental help I got from Mitchel Hurrah and Stephen Cini, their support was crucial for the successful completion of the validation studies.

I want to express my gratitude to the institutions who supported my projects financially during this long academic period, especially, the USF College of Engineering, Southeastern Center for Electrical Engineering Education (SCEEE), National Institutes of Health, and USF Office of Graduate Studies. Financial support from these organizations have ensured the continuation of this research work. I express my gratitude to Diana, Kristen and Gabriella, staff members in the Electrical Engineering department. They always extended their help promptly when needed.

I want to extend my gratitude to all my friends who supported me in this journey from close and afar. Specifically, I want to thank Kerem Can Celebi, Asfaq Mohammad Saad and ATM Golam Bari for their life advice and company.

My family members have been a constant support both mentally and financially. I want to thank my siblings Nandita Biswas and Diganta Biswas for always being there for me. They have attended to all family responsibilities that I could study abroad and finish my PhD. I want to express my gratitude to my father, Milon Kumar Biswas. Although he is in heaven; his life lessons were crucial for developing my inquisitive nature toward the physical world.

Finally, I want to thank my mother Archana Sarker and my wife Sweety Sarker for always being the mental support I needed. Their encouragement and comfort keep me going. Finally, I want to thank the almighty God for giving me the mental strength to keep going through all the challenges in life.

Table of Contents

List of Tables

List of Figures

Abstract

Cerebral blood flow (CBF) is a good indicator of brain health as blood carries necessary nutrients, oxygen, and metabolic byproducts. Quantitative blood flow information can be used in several clinical and therapeutic applications such as stroke detection, measuring autoregulation, evaluating brain injury, or determining neuronal activity. Over the past few decades, light-based deep tissue hemodynamic detection modalities have become popular for non-invasive CBF measurements. In particular, noninvasive Diffuse Correlation Spectroscopy (DCS), has become a tool of choice for research and clinical applications due to its depth sensitivity (>1 cm), portability, validity against other technologies such as Magnetic Resonance Imaging (MRI) or Computed Tomography (CT), and its use of non-ionizing light radiation that permits prolonged and continuous real-time *in-vivo* measurements. Although the measurement accuracy of DCS is excellent, instrumentational complexity, cost, processing burden, and size constraints limit wide adoption.

In recent years, several alternative implementations of DCS have been proposed addressing its limitations, such as Diffuse Speckle Contrast Analysis (DSCA) and Speckle Contrast Optical Spectroscopy (SCOS). Briefly, in DCS a point detector, i.e., Single Photon Counting Avalanche Photodiode (SPAD), is used to measure temporal fluctuations of light intensity to compute the intensity autocorrelation function and estimate blood flow. DSCA and SCOS measure light intensity fluctuations with a camera, and compute second order speckle statistics to estimate tissue hemodynamics. Use of a camera as photodetector reduces instrumental complexity and data processing burden. These modalities provide a relatively easy measurement framework. However,

they are not suitable for portable multichannel operation due to the use of fiber coupled high coherence lasers and camera or APD array as a photodetector. Moreover, realizing a multichannel detection system with this technique would be expensive.

In this dissertation, I address the hardware limitations of DCS and speckle-based blood flow measurement. First, I introduce a novel digital hardware based TTL (Transistor to Transistor Logic) pulse counting technique, Compressed DCS (CDCS), which achieved 87.5% data compression for DCS data acquisition. Aside from excellent data compression, it provides a cost-effective (i.e., >100x cost efficiency) hardware scheme to implement multi-channel hardware acquisition for a DCS instrument. Second, I developed a fiber-less portable low power laser system for DCS – fiber-less DCS (FBDCS). I validated the capability of FBDCS to probe deeper into the tissue surface, up to 3.5 cm. Finally, I have introduced a novel deep tissue blood flow modality, Integrated Diffuse Speckle Contrast Spectroscopy (iDSCS), a simple photodiode based deep tissue blood flow detection technique. iDSCS utilizes an off-the-shelf, low-cost photodetector in photo-voltaic mode to detect temporal speckle fluctuations. A model-based fitting was then performed to compute relative blood flow (rBF).

All three technologies have been validated in phantom and *in-vivo* measurements. I further investigated noise in these systems thus providing a guide for future implementation. In combination, these techniques could pave the way for the development of a portable, multi-channel deep tissue blood flow detection device.

Chapter 1: Introduction

Blood flow is a significant biomarker for tissue health. Blood supplies necessary nutrients to tissue and clears metabolic byproducts. Chronic reduction in blood flow can diminish organ functions and lead to cell death [1]–[3] especially in critical tissues like the brain, whereas increased flow can indicate immune response, internal injury and recovery states, and in some cases cancer [2], [4]–[6]. In particular, cerebrovascular hemodynamics may be associated with various disease states (such as stroke and brain injury), with measurement of autoregulation and vascular tone potentially useful for diagnostic, therapeutic, and research purposes [2], [7]–[11]. Furthermore, functional brain activation is often reflected by alterations in CBF due to increased metabolic activity within regions of interest. Thus, an accurate, portable, and non-invasive device capable of monitoring or mapping CBF would aid neuropsychiatric research [12], [13].

Clinical measurement of CBF has several applications. Reduction in cerebral blood flow can induce irreversible brain injury resulting in loss of function, whereas normal or enhanced blood flow may enable and promote brain recovery [14]–[17]. For example, infants are susceptible to brain damage from reduced CBF during early development phases, potentially resulting in cognitive, visual, language, or sensory-motor disabilities [18], [19]. Thus, real-time monitoring of cerebral hemodynamics may provide information for physicians to better plan therapeutic and preventative interventions. The measurement of cerebral blood flow and metabolism has been utilized in the study of acute and chronic cerebral ischemia [20], [21]. Intra-operative hemodynamic measurement can aid in proper anesthesia administration and promote positive pre-

and post-operative outcomes [22]. Beyond its use for acute and chronic management, precise measurements of CBF have aided in developing stroke models in animals [23].

Traditionally, several non-invasive and non-optical methods such as MRI [24] and CT [25] and transcranial Doppler have been utilized to image or measure blood flow. CT and MRI are excellent radiological imaging techniques that can be used to noninvasively image structural features in the body. However, in part due to the size and cost of these imagers, they are not suitable for continuous bedside monitoring of CBF. In addition, CT has the added risk of using ionizing radiation. Transcranial Doppler [26] provides a better bedside solution to monitor blood flow, however it can only measure blood velocity in proximal cerebral arteries (it does not measure perfusion), and therefore lacks the capabilities to measure flow in the microvasculature. In addition, TCD can only be used via small, limited visualization windows in the head. These shortcomings have provided the opportunity to develop advanced optical cerebral hemodynamic detection technologies.

Diffuse Correlation Spectroscopy (DCS) [27] is an excellent near infrared deep tissue blood flow measurement technique. DCS utilizes a single point source and detector to quantify temporal fluctuations in light intensity to quantitatively estimate blood flow. DCS senses and quantifies an index of blood flow (F) in tissue microvasculature from intensity fluctuations in coherent laser light that has diffused through tissue. DCS blood flow indices have been validated against a variety of gold standard modalities including Doppler ultrasound [28], Computed Tomography (CT) [29] and Magnetic Resonance Imaging (MRI) [30]. DCS's utility has been demonstrated for noninvasive deep-tissue blood flow measurements in adult/pediatric brain [27], [31]–[33] in muscle [34], [35] and in spinal cord [36]–[38]. Despite these advantages and increased recent interest, instrumental/operational complexity and high implementation cost have limited

DCS's wide adoption by the medical community. DCS requires sophisticated circuits to drive its detector (single photon counting avalanche photodiodes) and long-coherence length, single frequency laser sources, all of which are bulky and expensive. Further, high data sampling frequencies and necessity to post-process data with non-linear curve fitting impose significant software and hardware burdens, limiting DCS' wide adoption.

Laser Speckle Contrast Imaging (LSCI) is a related optical technology to image blood flow often from tissues at relatively shallow depths (i.e., 0.5 -1 mm), using simple instrumentation and algorithms [39]. In LSCI, temporal intensity (speckle) fluctuations caused by a single dynamic scattering events are imaged using a camera and processed to estimate blood flow. The critical difference between conventional implementations of DCS and LSCI is that DCS records and analyzes fluctuations in light that has diffused through tissue experiencing multiple scattering events, whereas LSCI measures and analyzes light that has reflected from the tissue surface, with single/few dynamic scattering events. Thus, LSCI is limited in measurement depth due to its measurement geometry, and it is also susceptible to errors due to the presence of static scatters. Multi-exposure Speckle Imaging (MESI) [21] is an improvement to LSCI, to address some of its limitations, and enable quantitative baseline blood flow imaging. MESI is a full-field imaging technique where multiple images of the sample are recorded while varying the exposure time of the camera. Therefore, MESI enables the measurement of the speckle visibility over multiple time scales, thus accounting for the contribution of both static (i.e., skull) and dynamic (i.e., red blood cell) scatterers.

The objective of this dissertation is to develop and validate methods that can dramatically reduce the cost and instrumentation burden of optical deep-tissue blood flow monitoring. Specifically, this dissertation addresses changes to three facets of conventional DCS

instrumentation, with an overall goal of arriving at a design for a cost effective, low power, small footprint blood flow monitor. Realizing such technology requires innovation in three major areas.

1. Data acquisition: Conventional DCS instruments require the use of digital photon counters to record intensity fluctuations. Existing digital counters are inefficient for recording low DCS photon counts, thereby posing a burden to scaling DCS for imaging applications. This dissertation introduces a compressed sensing approach using custom hardware counters to alleviate this cost and instrumentation limitation.

2. Light source: Conventional DCS instruments have used expensive and large single frequency diode laser modules to illuminate tissue via fiber optic cables. This dissertation realizes the tissue illumination without fibers, permitting use of smaller, off-the-shelf, cheaper single mode laser diodes.

3. Light detection: Conventional DCS instruments require the use of high-sensitivity, large, expensive single photon counting avalanche photodiode modules. This dissertation realizes light collection using small, off-the-shelf, cheap photodiodes, and develops a custom electronic circuit to implement MESI-processing schemes for DCS.

The rest of this dissertation is organized thusly:

- Chapter 2 introduces the theory of DCS and speckle-based modalities for deep tissue blood flow measurement.
- Chapter 3 reports the development and of a compressed data acquisition system using 4-bit binary counters to replace traditional DCS photon counters. This compact data acquisition system is validated in phantom and *in-vivo* experiments.
- Chapter 4 reports the development, validation, and characterization of a novel fiberless laser source for deep tissue blood flow measurement with DCS.

- Chapter 5 reports the development of a new deep tissue blood flow detection technique, integrated Diffuse Speckle Contrast Spectroscopy (iDSCS), which comprises of a simple unbiased photodiode to detect temporal speckle intensities, and a custom electronic circuit to implement MESI data processing schemes for DCS
- Chapter 6 concludes the dissertation with discussions on future directions.

Chapter 2: Deep Tissue Blood Flow Detection Technologies

2.1 Flow Measurement with Dynamic Speckle

When a coherent light source is used to illuminate tissue, the light reflected from the surface is the superposition of waves that have travelled multiple distances through the sample. When detected (e.g., by a camera), these waves coherently combine to create an interference image called a speckle pattern. Interactions of light with moving particles in the tissue (typically red blood cells) cause the pathlength of the waves to change, which in turn cause temporal fluctuations in the speckle pattern. The time scale of these 'dynamic speckles' can be used to infer the speed of particles moving in the tissue. This speckle pattern is the basis of numerous wide field imaging techniques such as Laser Speckle Contrast Imaging [39], Multi-exposure Speckle Imaging [21], Diffuse Speckle Contrast Analysis [40], Speckle Contrast Optical Spectroscopy [41], [42]. Instead of a wide field image, if light is sampled with a point detector, the temporal intensity fluctuations can be used for light diffusion based spectroscopic technologies to measure blood flow, such as Diffuse Correlation Spectroscopy [27], [43].

Over the past several decades, multiple imaging and spectroscopy approaches have used dynamic speckle to quantify the dynamics of moving particles such as red blood cells [44]–[46]. Most of these works have improved or devised instrumentation and mathematical models to analyze dynamic speckle fluctuations and estimate a blood flow index (F). These methods calculate the decorrelation or variance of the dynamic speckle fluctuations, often over multiple time scales. In essence, fast flow in tissue would result in the dynamic speckle fluctuations that

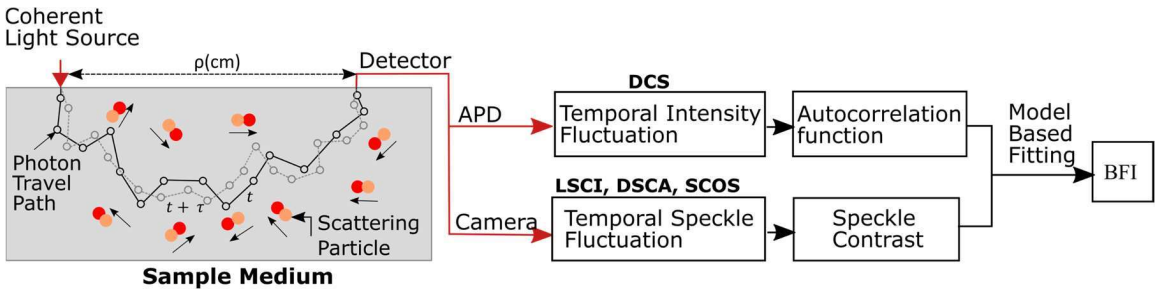

Figure 2.1 Outline of CBF measurement by different optical methods. The DCS technique characterizes the correlation of temporal intensity fluctuations whereas speckle-based measurement such as LSCI, DSCA and SCOS quantifies spatio-temporal speckle contrast. Model based fitting results in blood flow information (BFI) in underlaying tissue microvasculature.

decorrelate faster and vice versa for slow flow. Model based fitting of these speckle decorrelations yield a blood flow index (F) that is proportional to tissue perfusion (in units of ml/100g tissue/min).

Figure 2.1 outlines a summary of blood flow measurement using different light-based technologies. Typically, a wavelength stabilized laser is used to illuminate the sample. A photodetection element – APDs in DCS and cameras in LSCI, MESI, DSCA and SCOS – is configured to record temporal speckle intensity fluctuation. The acquired data is then fit to mathematical models to calculate a blood flow index (F). In the following sections, I describe the instrumentation and theory of DCS and LSCI, to estimate flow.

2.2 Diffuse Correlation Spectroscopy

Diffuse Correlation Spectroscopy (DCS) is a noninvasive optical method to measure deep tissue blood flow. DCS detects blood flow from temporal intensity fluctuations of diffusely scattered light. A typical DCS measurement (Figure 2.2) consists of a wavelength stabilized laser source (coherence length >5m) to illuminate the tissue, a single photon counting avalanche photodiode to detect the light and hardware for acquiring and processing the photon counts. The photons diffuse through tissue and scatter off red blood cells; the motion of red blood cells impart

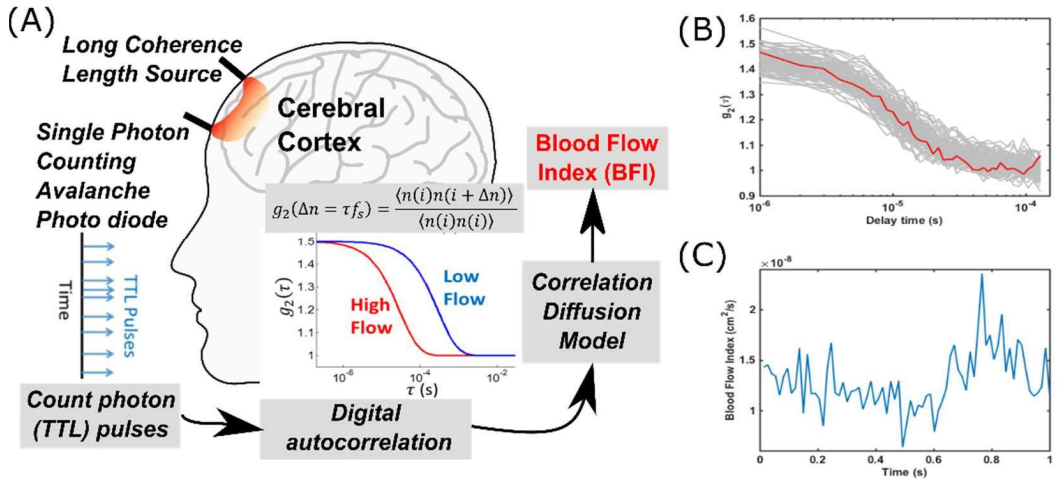

Figure 2.2 (A) Schematic outlining a typical DCS setup. It consists of long coherence laser source and photon counting avalanche photodiode module which generates a TTL pulse for each detected photon. The pulses are counted by an embedded system board (DAQ, FPGA, Microcontroller, etc.). The digital intensity autocorrelation ($g_2(\tau)$) is computed on a computer for data fitting and visualization. (B) Representative intensity autocorrelation functions measured from forearm of a healthy volunteer. The gray lines represent 73 $g_2\ (\tau)$ curves and the red line is the average. (C) Temporal trace of the blood flow index (F) in diffusion units (cm^2/s) over 1 second. Each point is from the fit of one $g_2\ (\tau)$ curve to the DCS model.

temporal intensity fluctuations. The photon counting APDs generate an electrical TTL pulse for every detected photon. Data acquisition hardware samples the TTL pulses within a defined sample time ($t_{sample} \approx 100ns - 1\mu s$). The samples are stored in a vector for the duration of the integration time ($t_{int} \approx 10ms - 1s$). Data sampled during one integration cycle is considered as an individual data frame to compute the intensity autocorrelation function, i.e., multiplying the detected photon vector $I(t)$ with its time-shifted copy $I(t + \tau)$ [47]–[49]. Autocorrelation can be performed using slow hardware correlators or faster software correlators. With the advancement in embedded hardware, software-based correlators are now popular. These are capable of fitting and displaying the BFI index [47], [50] in real-time. In prior work, NI DAQ [47], [51] and FPGA [50] based systems have been shown capable of extracting fast flow changes in different scenarios.

Formally, the light intensity fluctuations in tissue can be modeled by the Correlation Diffusion Equation [52],

$$\left[\nabla \cdot (D(r)\nabla) - v\mu_a(r) - \frac{\alpha}{3} v\mu_s' k_0^2 \langle \Delta r^2(\tau) \rangle\right] G_1(r,\tau) = -vS(r) \tag{2.1}$$

here, $G_1(r,\tau)$ is the unnormalized electric field autocorrelation function, μ_a , μ_s' are tissue absorption and reduced scattering coefficients $\left(\mu_s' = \mu_s(1-g)\right)$, D is photon diffusion coefficient of the medium, calculated from the absorption and reduced scattering coefficients μ_a and μ_s' as $D = [3(\mu_a + \mu_s')]^{-1}$, $k_0 = 2\pi/\lambda$ is the wavenumber of the source, $S(r)$ is isotropic source term, α is the fraction of dynamic photon scattering in the medium, and $< \Delta r^2(\tau) >$ is the mean square displacement of dynamic scattering particle in the tissue geometry (e.g., red blood cells). The solution of the correlation diffusion equation (CDE) for homogeneous semi-infinite tissue geometry is,

$$G_1(r,\tau) = \frac{v}{4\pi D}\left[\frac{\exp(-K(\tau)r_1)}{r1} - \frac{\exp(-K(\tau)r_2)}{r_2}\right] \tag{2.2}$$

Here,

$$K(\tau) = \sqrt{\frac{\left(\mu_a + \frac{\alpha}{3}\mu_s' k_0^2 \langle \Delta r^2(\tau) \rangle\right) v}{D}} \tag{2.3}$$

$$r_1 = \sqrt{l_{tr}^2 + \rho^2} \tag{2.4}$$

$$r_2 = \sqrt{[(2z_b + l_{tr})^2 + \rho^2]} \tag{2.5}$$

$$l_{tr} = \frac{1}{\mu_a + \mu_s'} \tag{2.6}$$

$K(\tau)$ is the decay constant, τ is the correlation time. $\langle \Delta r^2\ (\tau) \rangle$ represents the mean square particle displacement in time τ. For Brownian motion,

$$\langle \Delta r^2(\tau) \rangle = 6D_B\tau \tag{2.8}$$

D_B is particle diffusion coefficient. Empirically, dynamics of blood flow in tissue is well-modeled with Brownian diffusion[52]. The normalized intensity autocorrelation function is represented by $g_2\ (\tau)$ as,

$$g_2(\tau) = \frac{\langle I(t)I(t+\tau) \rangle}{\langle I(t) \rangle^2} \tag{2.9}$$

The well-known Siegert relation [53], resolves the relationship between the normalized electric field autocorrelation function (g_1), and the intensity temporal autocorrelation function (g_2) as,

$$g_2(\tau) = 1 + \beta |g_1(\tau)|^2 \tag{2.10}$$

here, β is constant depending on the optical setup for the instrumentation. DCS measures $g_2\ (\tau)$ from the recorded intensities using equation 2.9. The measured $g_2(\tau)$ is fit to the model described in equation 2.10, recognizing that $g_1(\tau) = G_1(\tau)/G_1(0)$, and that $G_1(\tau)$is given by equation 2.2. The blood flow index (F) is extracted from this non-linear curve fit. It is apparent that the blood

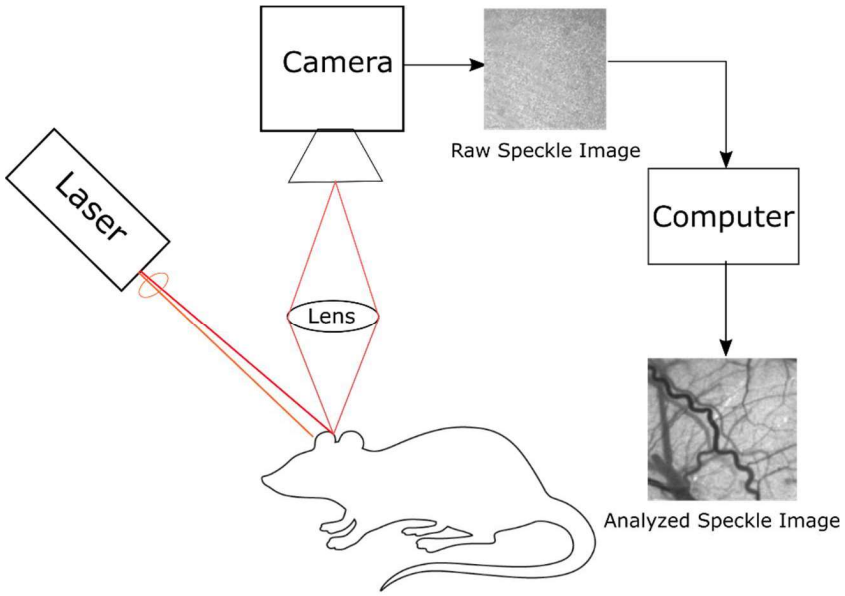

Figure 2.3 Schematic showing the setup for LSCI for cerebral blood flow imaging. A single mode laser diode illuminates a sample (exposed rat cortex) while a CCD camera images the spatio-temporal varying speckle pattern. The speckle image is processed, and 2-D image of cerebral blood flow is computed. Speckle images adapted from [18].

flow index $F = \alpha D_B$. Experimentally, it has been shown that the Brownian model $\langle \Delta r^2(\tau) \rangle = 6D_B$ fits better for a wide variety of tissue types [28], [29], [34], [35], [48], [54].

2.3 Laser Speckle Contrast Imaging (LSCI)

Laser speckle contrast imaging functions on the same physical basis as DCS, but with different imaging geometries, and simpler data processing schemes. As described below, the mathematical models describing flow measured with LSCI need to account for the integration of detected intensities by the camera. In Chapter 5, I will describe how LSCI processing schemes can be used to simplify deep tissue blood flow monitoring with DCS.

An LSCI instrument consists of three major components, as shown in Figure 2.3 – a long coherence length laser source (typically 650-900 nm wavelength), a conventional CMOS/CCD camera, and a computing system for analysis. Unlike DCS, LSCI is often used in an imaging

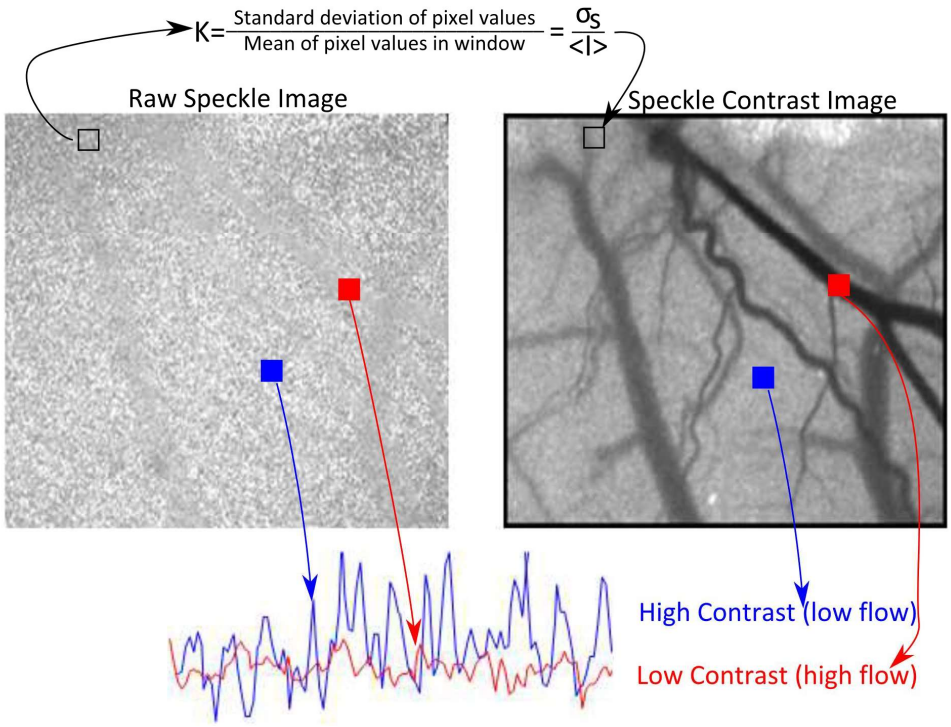

Figure 2.4 (left) Raw speckle image showing the temporal blurring of the speckle. In the field of view in which the speed of moving particle in the sample is indicated by the extent of spatial blurring. (right) Blood flow map of the brain surface obtained by spatial speckle contrast analysis of the raw speckle image using a 7 x 7 window. Image adapted from [18].

configuration. Here the laser is collimated/slightly divergent to illuminate the entire field of view imaged by the camera. Speckle pattern acquired by a CCD camera is recorded on a computer, and raw speckle images are analyzed by the methods described below to yield a 2-D blood flow map.

LSCI calculates the localized variance of the detected intensities as a speckle contrast. The speckle contrast is calculated from a spatial/temporal window that is translated across the image(s), and is defined as the ratio of standard deviation to the mean of intensities within the window-

$$K = \frac{\sigma}{\langle I \rangle} \tag{2.11}$$

Here, K is the speckle contrast, σ is the standard deviation, and $\langle I \rangle$ is the mean of intensities. Subscripts s and t (K_s, K_t and σ_s, σ_t) are often used to denote spatial or temporal speckle contrast/standard deviation.

Table 2.1 Comparison between the DCS and LSCI technology.

Characteristics	LSCI	DCS
Theory	Single dynamic scattering	Light diffusion
Illumination source	Long coherence laser (>5m)	Long coherence laser (>5m)
Bedside monitoring	No	Yes
Penetration depth	~1 mm	~20 mm
Non-invasive CBF measurement	No	Yes
Quantitative	Yes	Yes
Instrument cost and complexity	Low and easy	Relatively Higher and more complex
Portability	Yes	Yes
Temporal resolution	100 Hz (depends on camera exposure time)	20-100 Hz

A raw speckle image of a rat brain taken through a thinned skull is shown in Figure 2.4. The raw image depicts a grainy speckle image with localized motion manifesting as spatial/temporal blurring. This represents the averaging of speckle intensities over the camera integration time. When local speed is high, the intensity fluctuations are rapid, which when averaged over the camera exposure appears as regions of low contrast. When local speed is slow (or static), the intensity fluctuations are slow (or constant), which when averaged over the camera exposure appears as regions of high contrast. The reconstructed 2-D map of the image is calculated using equation 2.11. The darker areas have lower contrast and higher moving particles. More quantitatively, the speckle contrast K can be expressed as a function of exposure time T by equation 2.12,

$$K^2(T) = \frac{\sigma_s^2(T)}{\langle I \rangle^2} = \frac{2\beta}{T}\int_0^T \left(1 - \frac{\tau}{T}\right)[g_1(r,\tau)]^2 d\tau \tag{2.12}$$

where τ is the decorrelation time, T is the exposure time, and β is the speckle averaging factor accounting detector size, speckle size, and polarization. Now the speckle contrast is dependent on the form of $g_1(r,\tau)$. For a single dynamic scattering $g_1\ (r,\tau)$ is approximated as,

$$g_1(\tau) = \exp\left(-\frac{\tau}{\tau_c}\right) \tag{2.13}$$

As described earlier, the LSCI technique can use spatial and temporal analysis of the variance. Spatial analysis has a higher temporal resolution at the cost of lower spatial resolution. in which an image M× N pixels (512× 512 pixels used in [55]) is taken, and a 7× 7-pixel window is defined, the spatial processing will blur some high resolution features. A smaller window compromises the statistics, while a higher number of pixels in the window cause a reduction in spatial resolution. The temporal statistics of speckle contrast can provide a greater spatial

resolution in which a single point is sampled over a finite time. Speckle contrast calculation is then carried out from the sampled vector. Several drawbacks of traditional LSCI measurement techniques are addressed by Parthasarathy et al. [56]. These include the inability of LSCI to perform quantitative blood flow measurements, calibration difficulties [55], use of an approximation measurement model, inability for non-invasive CBF measurement, and inaccurate CBF prediction in the presence of static scatterers.

A robust multi-exposure speckle imaging technique was developed and validated to obtain quantitative baseline flow measurements. The measurement protocol consists of image acquisition over multiple exposure times and fitting it to a model developed for extracting flow information τ_c.

$$K(T,\tau_c) = \left\{ \beta\rho^2 \frac{e^{-2x} - 1 + 2x}{2x^2} + 4\beta\rho(1-\rho)\frac{e^{-x} - 1 + x}{x^2} + v_{ne} + v_{noise} \right\} \tag{2.14}$$

where, $x = \frac{T}{\tau_c}$, $\rho = \frac{I_f}{I_f + I_s}$ is the fraction of dynamically scattered light, β is normalization factor accounting for speckle averaging effects, T is the camera exposure time, τ_c is the correlation time of the speckles, and v_{noise} and v_{ne} account for the constant variance for experimental and nonergodic light.

2.4 Diffuse Speckle Contrast Analysis

The simpler instrumentation of LSCI can be used to obtain deep-tissue blood flow measurements, using Diffuse Speckle Contrast Analysis (DSCA). [40] Briefly, DSCA performs measurements in a diffuse geometry (as in DCS) but using cameras as a detector rather than single photon counting detectors. The speckle intensity fluctuations recorded by the camera are analyzed using speckle contrast processing schemes, to yield a speckle visibility curve – the normalized speckle variance of the detected intensities (K^2) as a function of camera exposure time. DSCA

then relates K^2 to the measurement dynamics as in equation 2.12. Here $g_1(\tau)$ is modeled from the solution to the correlation diffusion equation (Equation 2.2) rather than the single dynamic scattering model in Equation 2.13.

Chapter 3: Lossless Compressed Sensing of Photon Counts for Fast DCS

3.1 Introduction

Blood flow is a biomarker for tissue health because it correlates with metabolism and disease state in different parts of the body [1], [3], [57]–[59]. In recent years, DCS [27], [52], [60], [61] has emerged as a popular method for portable, noninvasive, bedside monitoring of deep tissue blood flow.

As described earlier, a typical DCS instrument, (Figure. 3.1) comprises a long coherence laser to illuminate the tissue and single photon counting detectors to record light reflected from the tissue. Paying more attention to the data processing/analysis scheme, a custom correlator, samples TTL pulses generated by the detectors (typically at 1-10 MHz) and computes an intensity autocorrelation function that quantifies temporal fluctuations in the light. Recently, we [47] and

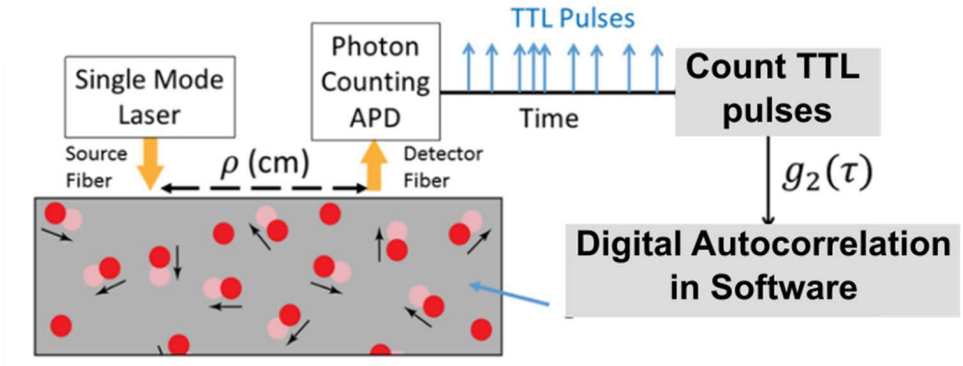

Figure 3.1 Schematic outlining the DCS technique. A wavelength stabilized laser is configured as an illumination source. Dynamic scatterer in the tissue (i.e., red blood cells) causes deviation in individual photon travel path thus result in temporal fluctuations at the detector surface. These fluctuations are sensed by a series of APDs and converted to TTL pulses. A counter module is configured to sample these TTL pulses. The autocorrelation function $g_2(\tau)$ of this sampled vector is fit to a model to calculate the blood flow.

others [62]–[64] have demonstrated the use of customized National Instruments (NI) counter/timers or FPGAs for data acquisition and software computation of DCS blood flow indices at speeds up to 100 Hz. These improvements to the temporal resolution have facilitated vital new measurements such as noninvasive quantification of cerebral autoregulation [65]–[67], critical closing/intracranial pressure [68], [69], and brain arteriole compliance [68], [69]. In DCS, single mode fibers are used to sample light from one speckle, which prevents speckle averaging at the detector and expands the dynamic range of measured intensity autocorrelation functions. However, since single-mode detection comes at the expense of signal levels, DCS intensity autocorrelation functions measured at a single channel are noisy. To overcome this limitation, typical DCS instrument implementations often have more than one detection channel (3-6) at a single measurement site (or for a single source-detector separation) to improve the signal-to-noise ratio of measured autocorrelation functions and hence blood flow estimates. Expansion of DCS measurements to an imaging configuration (e.g., Diffuse Correlation Tomography [70], [71]) would multiply the need for multiple detection channels. For example, tomography with eight detection positions would require 32-48 detection channels.

Two significant technical limitations restrict the use of multiple detection channels in DCS. Most commercial data acquisition systems limit the number of available counters/timers on a single board to 16. More significantly, parallel counting of photons and parallel computation of intensity autocorrelation functions from multiple detection channels will be a memory and computationally expensive process. These requirements for multiple digital counting elements (i.e., counters) increase instrument cost, complexity, and data bandwidth.

In this chapter, I introduce a new approach – compressed DCS (CDCS) – for fast, computationally efficient, multi-channel measurement of DCS intensity autocorrelation functions

without using processor embedded counter modules. This approach implements photon counting using eight 4-bit Binary Coded Decimal (BCD) counters rather than digital in-processor (32-bit) counter modules typically used in DCS data acquisition systems. The CDCS system achieves an 87.5% data compression without compromising on measurement accuracy or SNR, while maintaining low data burden and cost. I present experimental validation of the CDCS approach, comparing it with a conventional eight-channel DCS system in tissue-simulating phantoms and in-vivo experiments on humans. The following sections briefly describe the traditional DCS technique and the CDCS approach.

3.2 Theory and Background

A schematic of a typical DCS system is shown in Figure 3.1. Light from a long coherence length near-infrared laser source illuminates the tissue through an optical fiber. Near-infrared light diffuses through tissue and is detected by a single mode optical fiber positioned 1-3 cm away from the source and is redirected to Single Photon Counting Avalanche Photodiode modules (APDs), that produce a TTL pulse for each detected photon [47]. Due to the high temporal coherence of the laser source, changes in the optical pathlength of light diffusing through the tissue (i.e., due to scattering off moving particles/red blood cells) impart fluctuations in the intensity recorded at the detector, which is then used to compute the digital normalized intensity autocorrelation function. Blood flow is estimated by fitting the computed autocorrelation function to a diffusion model appropriate for the tissue geometry [52]. Here, I expand on the discussions from earlier (Chapter 2), to highlight the photon counting scheme.

Photon counts are detected as a stream of TTL pulses, which are sampled by counter/timer modules at a fixed sampling frequency f_s . If we consider the stream of photon counts as $n(i)$, then the normalized intensity autocorrelation function, $g_2\ (\tau)$, is:

$$g_2(\Delta n = \tau f_s) = \frac{\langle n(i)n(i+\Delta n)\rangle}{\langle n(i)n(i)\rangle} \tag{3.1}$$

here, τ is the autocorrelation delay time and $\Delta n = \tau f_s$ is the integer number of shifts of the photon count vector for a given delay time. The angle brackets ($\langle\,\rangle$) indicate averaging of the autocorrelation function over a duration denoted by the integration time t_{int}, which determines the overall speed of the measurement. For example, a system with a 10 ms integration time will yield a 100 Hz acquisition rate. The size of the individual photon count vector is defined by the integration time t_{int} and sampling time t_{sample}. For, $t_{int} = 10\ ms$ and $t_{sample} = 1/f_s = 1\ \mu s$, $n(i)$ is a 10,000-point vector. The measured intensity autocorrelation function is fit to solution of Correlation Diffusion Equation (Equation 2.10 and 2.2) to compute the blood flow index (F). In a typical implementation, DCS photon counts are sampled and recorded using in-processor

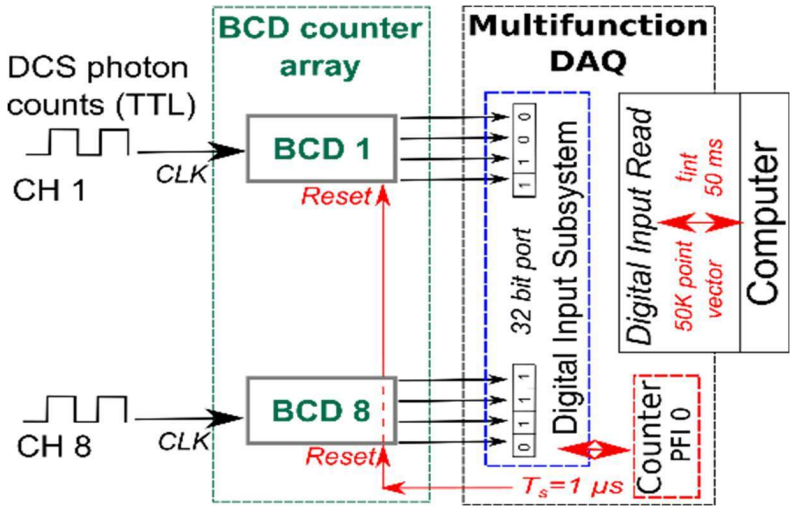

Figure 3.2 Block diagram outlining the compressed DCS photon counting system. The outputs from individual single photon counting APDs were routed to the clock pin (CLK) of a BCD counter. The output from the 8-BCD counters (i.e., 4-bit output for each BCD counter for a total 32-digital lines) was sampled through a 32-bit digital I/O port of a multifunction DAQ and recorded on a computer for processing. A timer from DAQ (NI PCIe-6353) was configured to reset all BCD counters at a frequency of $f_s = 1MHz$. For an integration time of $t_{int} = 50\ ms$ a total of 50,000 sample 32-bit vector was recorded.

Counter/Timer modules (for example, using a National Instruments PCIe/PXIe6612 board with eight counter/timers [47]). DCS intensity autocorrelation functions were computed in software (LabVIEW), and blood flow indices were estimated offline.

3.3 Compressed DCS: Multiple Channel Sampling with BCD Array

Here, I outline the approach for compressed DCS, using custom electronics for memory efficient recording of photon counts. Prior implementations of DCS involved using in-processor counter/timer modules (typically 32-bit). For example, we [47] and others [72] have used 32-bit counters on an NI PCIe/PXIe-6612 board or similar. Recall that DCS detects light using single mode fibers with output powers in the order of a few pW; the typical photon count rate in a DCS measurement ranges from 10-1000 KHz in one channel. Indeed, most single photon counting detectors have a maximum count rate of 2-4 MHz. At a sampling frequency of 1 MHz ($t_{sample} = 1\ \mu s$), these intensity levels result in counts of either 0, 1 or 2 for each microsecond, i.e., elements of the vector $n(i)$ are either 0, 1 or 2. Using a 32-bit counter for these low-light (low-count) applications is highly inefficient. Indeed, only 1/16 or 1/32 of the data capacity of the 32-bit register is being used when counts are 0, 1 or 2 and only 2 least-significant bits of the 32-bit counter change with each sampling. In other words, a maximum photon count rate of 2 MHz can be represented with just two data bits of an incremental counter capable of storing a minimum of 2-bits. With 32-bit counters, most memory and data communication bandwidth are largely underutilized. Note that these inefficiencies worsen for systems/experiments with faster sampling rates (e.g., $t_{sample} = 100\ ns$).

Practically, CDCS is implemented using widely available low-cost Binary Coded Decimal (BCD) chips (e.g., 74LS90). The schematic of one such implementation is shown in Figure. 3.2. BCD counters use 4-bits to store decimal values up to 10. The TTL outputs from a single photon

counting module are connected to the clock input of the BCD counter, which increments its internal register with every TTL pulse (photon). Thus, an array of eight BCD counters can simultaneously sample DCS photon counts from eight single photon counting modules, forming a single 32-bit integer output (i.e., 4-bit output of 8 BCD counter). The 32-bit integer is recorded via general purpose digital input/output lines of a multifunction data acquisition system (National Instruments PCIe-6353). The data acquisition process is controlled by two software-controlled counter/timers on the data acquisition board. The first, operating at 1MHz, clocks the digital I/O read operation, and simultaneously resets the BCD counters. The second controls the integration/averaging time of the photon counts. Thus, an integration time of $t_{int} = 50\ ms$ would yield a 50K point vector of photon counts. A custom LabVIEW based GUI was used to control the data acquisition process and perform bit-wise operations to separate photon counts from individual channels (i.e., combination of 4-bits) to compute the DCS intensity autocorrelation functions as described earlier [47]. For a single channel, the CDCS system utilizes 4-bits to record photon counts, compared to the conventional DCS system which uses 32 bits. This gives the CDCS system a data compression efficiency of 87.5%.

3.4 Experiments and Results

All experiments were carried out with a custom DCS instrument. Briefly, light from a wavelength stabilized laser (Toptica Photonics, iBeam Smart, 785nm, 120mW, coherence length >50m) was coupled to a multi-mode fiber and used to illuminate the sample (i.e., tissue phantom or human forearm). Reflected light from the sample was collected using single mode fibers placed 1 cm and 2.5 cm away from the source and redirected to single photon counting Avalanche Photo Diode (APDs) modules (Excelitas, SPCM-AQ4C); three detection channels were used at 1 cm source-detector separation, while five detector channels were used for the 2.5 cm source detector

separation. All fibers were set in place using a custom silicon mold to create an optical probe as described earlier [47], [73]. TTL outputs from each single photon counting APD were directed to both the BCD counter array (for CDCS software autocorrelation measurements as described in section 3.3) and 32-bit counters on an NI-9174/NI-9401 for conventional DCS autocorrelation measurement with a software correlator [47], [73] . In both cases, autocorrelation functions recorded from the same source-detector separation were averaged.

3.4.1 Intensity Autocorrelation Functions Measured with Compressed DCS: Validation on a Solid Tissue Simulating Phantom

I first demonstrate the ability of the CDCS system to acquire and compute autocorrelation curves from a solid tissue simulating phantom. For this experiment the DCS probe was secured to the surface of a solid phantom with an absorption coefficient $\mu_a = 0.1\ cm^{-1}$ and reduced

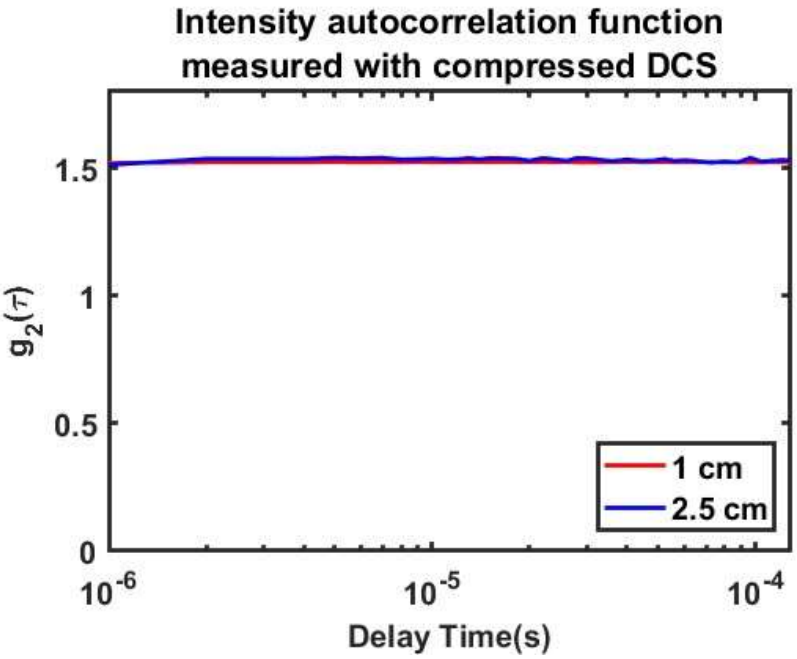

Figure 3.3 DCS intensity autocorrelation curves $g_2\ (\tau)$ acquired from a solid phantom using the compressed DCS system at source-detector separations of 1 cm (red curve) and 2.5 cm (blue curve). The solid phantom had optical properties of $\mu_a = 0.1\ cm^{-1}$ and $\mu_s' = 10\ cm^{-1}$ at 850 nm. A total of 100 $g_2\ (\tau)$ curves were averaged for these plots.

scattering coefficient $\mu_s' = 10\ cm^{-1}$ at 850 nm (INO Biomimic Phantoms, Quebec, CA). The phantom was illuminated with an optical power of 72 mW. The CDCS software correlator was configured to a sampling frequency of $f_{sampling} = 1\ MHz$, and an integration time of $t_{int} = 100\ ms$, resulting an effective acquisition frequency of 10 Hz. Each frame (i.e., photon counts recorded over 100 ms integration time) contained 100,000 vectors of 32-bit data for a single detection channel. For each channel an autocorrelation function was calculated with digital shifts of 1 to 250 samples, corresponding to delay times (τ) of $1\ \mu s$ to $250\ \mu s$. Figure.3.3 shows an average of 100 DCS intensity autocorrelation functions measured from a solid phantom at 1 and 2.5 cm source detector separation (red and blue curves respectively) using the CDCS software correlator. The autocorrelation curves do not decay, indicating no dynamic fluctuations (as expected with a solid phantom). These results offer the first validation of the CDCS system.

3.4.2 Intensity Autocorrelation Functions and Flow Indices Measured with Compressed DCS: Validation on a Liquid Tissue Simulating Phantom

Next, I demonstrate the accuracy of flow estimates measured with the CDCS system, by comparing it to conventional DCS autocorrelation measurements on a liquid tissue simulating phantom. A tissue simulating liquid phantom was prepared from Intralipid (20% emulsion, Sigma-Aldrich, MO), India ink, and distilled water, to realize a sample with an absorption coefficient $\mu_a = 0.1\ cm^{-1}$ and reduced scattering coefficient $\mu_s' = 10\ cm^{-1}$ at 785 nm. The DCS probe was placed on the surface of the liquid phantom, and DCS intensity autocorrelation functions were recorded using both traditional DCS and CDCS at a 10 Hz acquisition rate. Figure 3.4 shows representative intensity autocorrelation functions acquired by the CDCS system from the liquid phantom at 1 cm (red line) and 2.5 cm (blue line) source detector separations. These curves represent an average of 600 $g_2(\tau)$ curves acquired over 1 minute at an acquisition rate of 10 Hz.

Here, the decay in the autocorrelation function is caused by fluctuations in the photon intensity that manifest dynamic scattering from Brownian motion of fat molecules in the intralipid. The decay at 2.5 cm source detector separation is higher than at 1 cm because of increased photon travel length at the higher source-detector separation allows for more dynamic scattering to influence the intensity fluctuations.

To further validate the CDCS system, I compared the blood flow indices estimated from the CDCS measured intensity autocorrelation function with those estimated using a conventional DCS instrument. Using the methods and probes described earlier, intensity autocorrelation functions were recorded simultaneously from the liquid phantom using both CDCS and conventional DCS instruments. DCS intensity autocorrelation functions measured at 10 Hz from source detector separations 1 cm and 2.5 cm were fit to the semi-infinite solution to the correlation

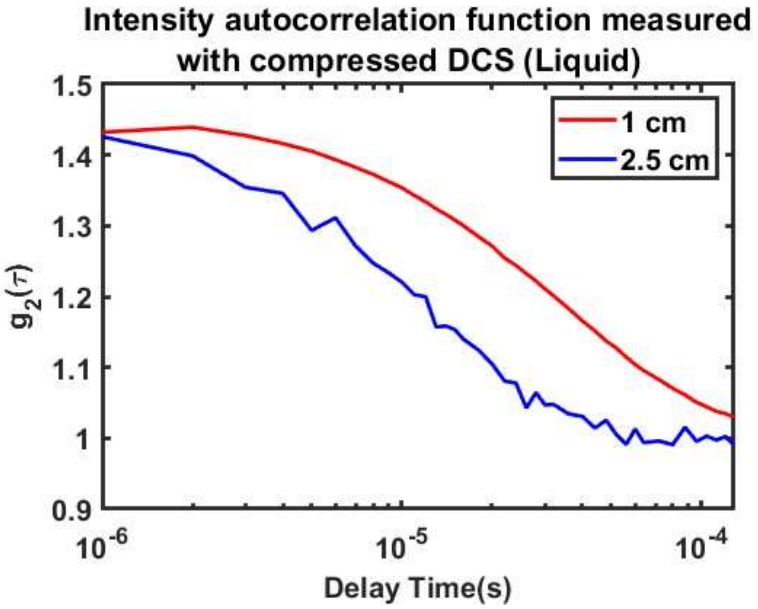

Figure 3.4 Intensity autocorrelation function ($g_2(\tau)$) acquired from a tissue simulating liquid phantom using the compressed DCS system at 1 cm (red) and 2.5 cm (blue) source detector separations. The liquid phantom had optical properties of $\mu_a = 0.1\ cm^{-1}$ and $\mu_s' = 10\ cm^{-1}$ at 785 nm. Results shown are an average of 1 min data collected at a data acquisition rate of 10 Hz.

diffusion equation (Equation. 2.10 and 2.2) to estimate the flow index F. Figure 3.5 shows the results of this comparison. Figure 3.5(A) and 3.5(C) show scatter plots of flow indices simultaneously measured using the two systems, for source-detector separations of 1 and 2.5 cm respectively. Here, flow indices estimated with the CDCS system are in the y-axis, while those

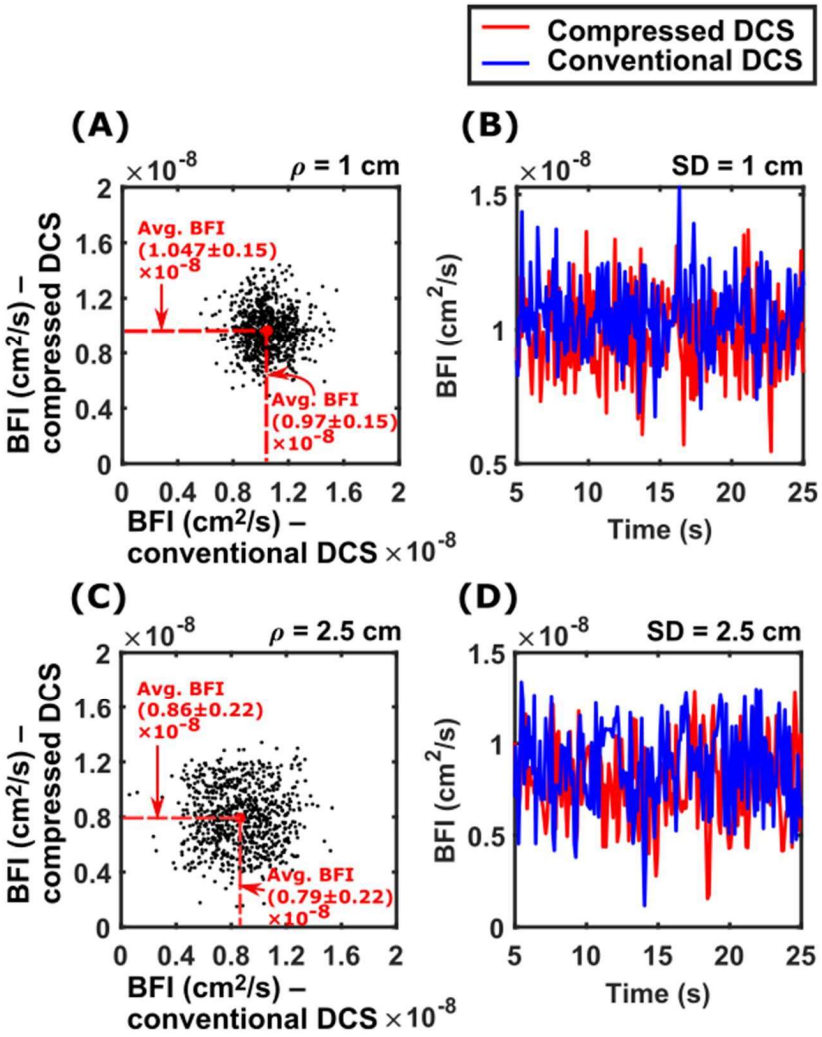

Figure 3.5 Comparison of blood flow indices (BFI) estimated with the compressed and conventional DCS systems from a liquid phantom. (A) and (C) show the scatter plot of the flow indices estimated by compressed DCS (y-axis) and conventional DCS (x-axis) for source detector separations $\rho = 1\ cm$ and $\rho = 2.5\ cm$ respectively. (B) and (C) show the comparative temporal traces of flow index measured with compressed DCS (red curve) and conventional DCS (blue curve). Results show good 1:1 correspondence, including similar average flow indices (no statistically significant difference, two-sample t-test).

estimated with the conventional DCS system are in the x-axis. Figure 3.5 (B) and (D) show the respective time courses of these flow indices, with the red curve depicting flow indices measured with CDCS and the blue curve depicting flow indices measured with conventional DCS. At 1 cm source-detector separation, the CDCS system estimated an average flow index of $F_{cmpDCS}^{1cm} = (1.047 \pm 0.15) \times 10^{-8}\ cm^2/s$, while the conventional DCS system estimated an average flow index of $F_{cnvDCS}^{1cm} = (0.97 \pm 0.15) \times 10^{-8}\ cm^2/s$. At 2.5 cm of source-detector separation, the CDCS system estimated an average flow index of $F_{cmpDCS}^{2.5c} = (0.86 \pm 0.22) \times 10^{-8}\ cm^2/s$, while the conventional DCS system estimated an average flow index of $F_{cnvDCS}^{2.5cm} = (0.79 \pm 0.22) \times 10^{-8}\ cm^2/s$. The errors represent the standard deviation of flow index estimates over the measurement period. A two-sample t-test revealed no statistically significant difference in the flow

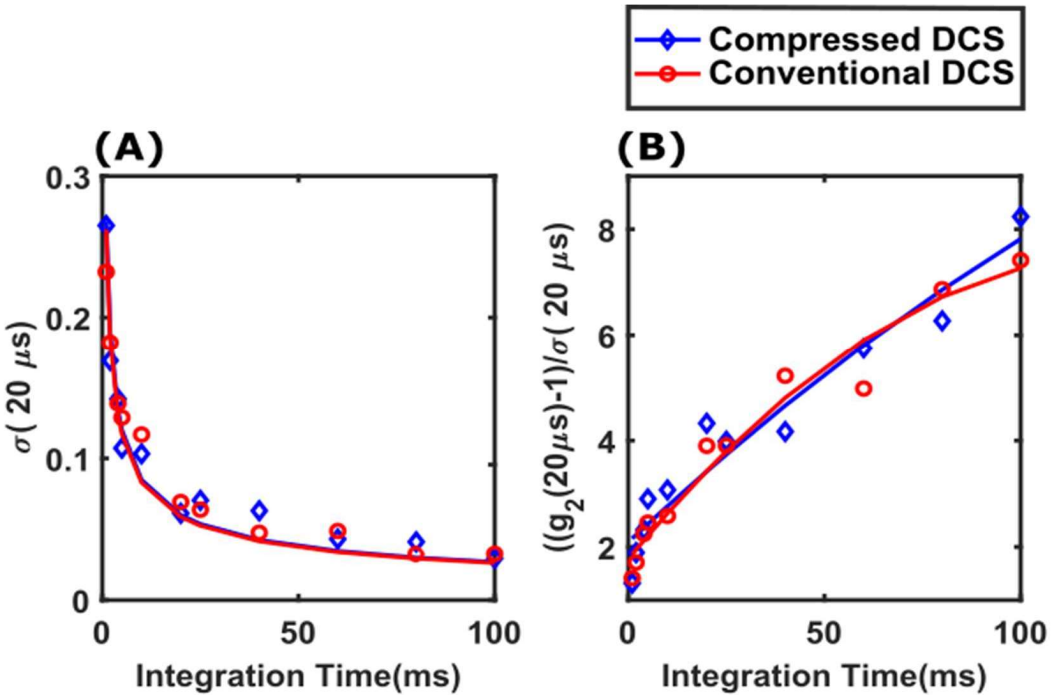

Figure 3.6 Noise (A) and Signal-to-Noise Ratio (B) of intensity autocorrelation functions measured using compressed DCS (blue) and conventional DCS (red) for representative delay time of $20\mu s$. Measurements were performed on a liquid phantom at source-detector separation of 1 cm and detection photon count rate of $100kHz$. Markers show individual data points while the solid lines are fits to the DCS correlation noise model. [70]

estimates estimated by the two instruments for both source-detector separations. These results validate the accuracy of the flow indices estimated by the CDCS system.

3.4.3 Signal-to-Noise Ratio of Autocorrelation Functions Measured with Compressed DCS: Validation on a Liquid Simulating Phantom

The final tissue phantom validation experiment concerns the comparison of the signal-to-noise ratios of intensity autocorrelation functions measured using CDCS and conventional DCS systems. Following the well-established DCS correlation noise model [70], I defined 'noise' ($\sigma(\tau)$ as the standard deviation of the measured intensity autocorrelation function $g_2(\tau)$, and SNR as $\zeta(\tau) = (g_2(\tau) - 1)/\sigma(\tau))$. DCS intensity autocorrelation functions were recorded simultaneously from the liquid phantom (1 cm source-detector separation) using both CDCS and conventional DCS systems. Since SNR depends on signal intensity, the light intensity for the measurement was fixed such that the detectors recorded an average photon count rate of $100\ kHz$. Autocorrelation functions were acquired at different rates by varying the integration time (t_{int}) of the measurements from 1 ms to $100\ ms$ (i.e., acquisition frequency of $1000\ Hz$ to $10\ Hz$). Figure. 3.6(A) shows the noise in the measurement of autocorrelation function at $20\mu s$ delay time, i.e., $\sigma(20\ \mu s)$, measured with both CDCS (blue) and conventional DCS (red). Figure. 3.6(B) shows the corresponding SNR. In both cases, the markers represent measurements from the liquid phantom, while the solid lines represent fits of the noise/SNR measurement to the correlation noise model [70] . It is readily apparent that the noise model fits well with the measured noise/SNR data. Moreover, the noise/SNR of CDCS measurements are comparable to those recorded with conventional DCS. This is an important validation step, because it shows that the data compression affected by the BCD counters is not at the expense of measurement SNR. Here, $20\mu s$ has been selected as a delay time to illustrate the noise performance, because it represents a section of the

autocorrelation function that is sensitive to changes in flow (Figure. 3.4). These results are in-line with our previous experiments to characterize the SNR of DCS systems [47], [73].

I further extend the SNR characterization of the CDCS system. In proceeding experiments the noise $\sigma(\tau)$, SNR $\zeta(\tau)$ and $g_2(\tau)$ variation is acquired as a function of integration time t_{int} and light intensity I. The results are shown in Figure 3.7. The variability of the intensity autocorrelation

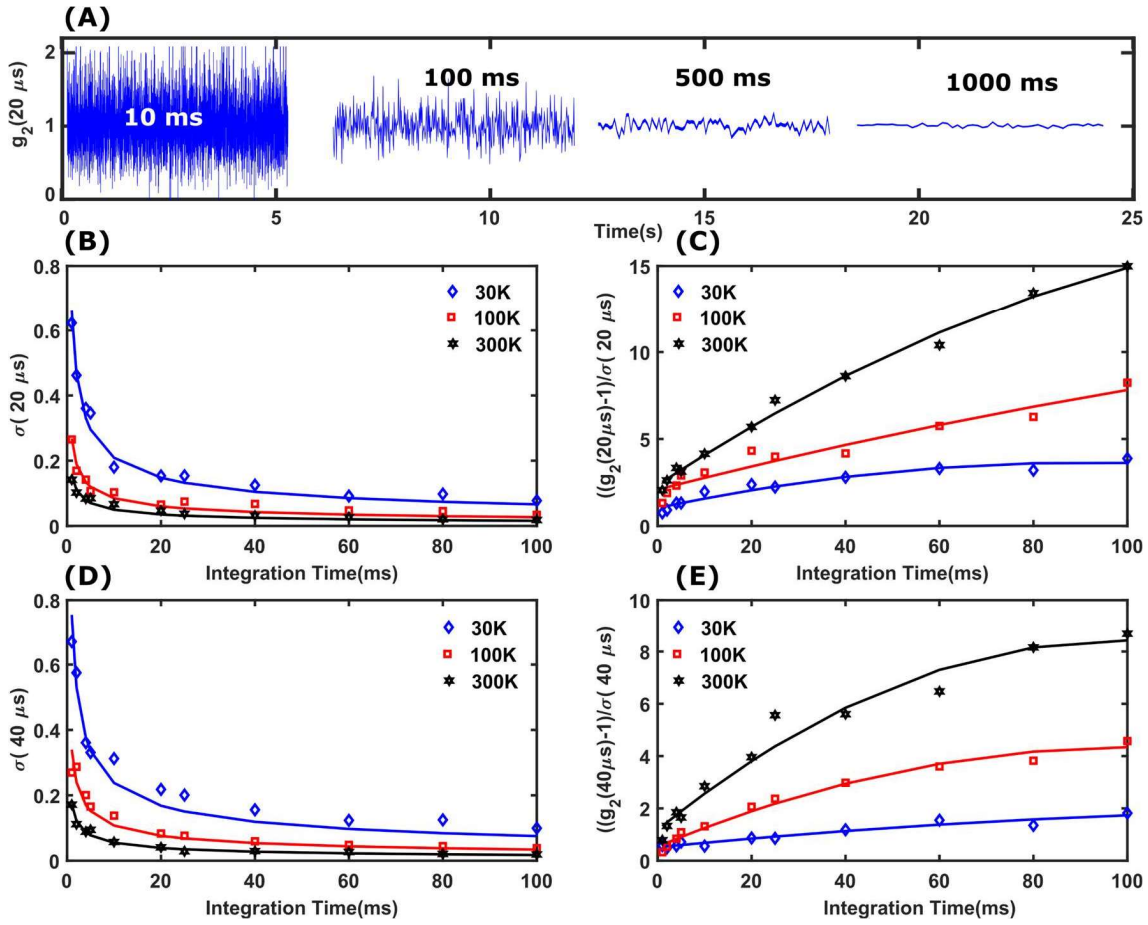

Figure 3.7 Experimental measurement of signal-to-noise ratio of DCS intensity autocorrelation functions with the compressed DCS. (A) Representative fluctuation of the measured autocorrelation function at delay time 20 μs for integration times 10ms, 50ms ,100ms and 1s. longer integration time increases the averaging of measurements and reduces noise. (B) and (D) Noise in measurement of $g_2(\tau)$ for delay times 20 μs and 40 μs respectively. (C) and (E) SNR of $g_2(\tau)$ measurements for delay times 20 μs and 40 μs respectively. The noise and SNR estimates for photon count rates of 30 KHz, 100 KHz and 300 KHz are marked with blue, red and black markers respectively, while the corresponding solid lines are fits to a DCS correlation noise model. [70]

function $g_2(\tau)$ is plotted in the Figure 3.7 (A) for an intensity of $I = 100\ kHz$. As the integration time is increased from 10 ms to 1 s, the $g_2(20\ \mu s)$ variability decreases. This is mainly due to more signals being averaged over time for a given intensity. Next, I characterized the system noise $\sigma(\tau)$ and SNR $\zeta(\tau)$ for three different light intensity levels i.e., 30 KHz 100 KHz and 300 KHz. Figures 3.7(B) and 3.7 (D) show the noise $\sigma(\tau)$ and 3.7(C) and 3.7(E) show the SNR for $20\ \mu s$ and $40\ \mu s$ delay times respectively. The data and fits are plotted as dots and solid lines respectively, with colors blue for 30 KHz intensity, red for 100 KHz, and black for 300 KHz. Increase in light intensity or integration time reduces system noise while boosting the SNR. However, increase in integration time would reduce temporal resolution, restricting detection of fast flow change features. These experiments provide a guideline for optimal light intensity and integration time indices to achieve a target SNR with the CDCS system.

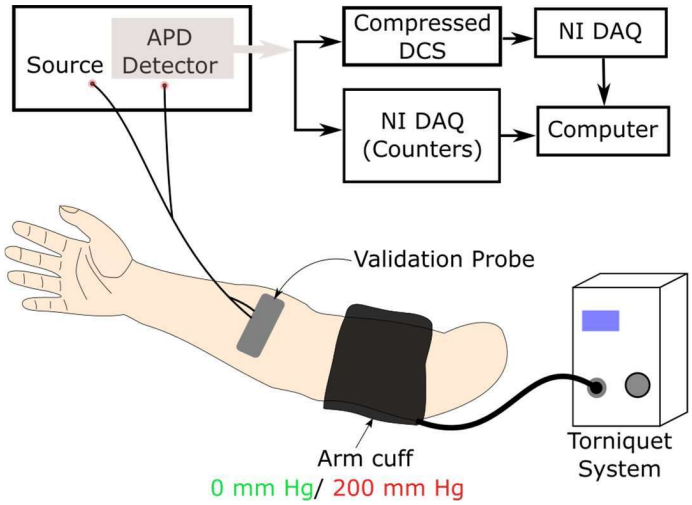

Figure 3.8 Schematic of in vivo arm-cuff occlusion experiment to validate compressed DCS blood flow measurements. The arm cuff was wrapped around the bicep of a volunteer. The optical probe was placed on the forearm and was connected to the light source and detectors via optical fibers. The output of the detector (i.e., TTL pulse output) is connected in both compressed DCS system (i.e., BCD counter) and conventional DCS software correlator (i.e., NI DAQ counters). An automatic tourniquet system was used to inflate the arm cuff to 200 mmHg to effect occlusion.

3.4.4 Dynamic Blood Flow Measurement in Human Arm with Compressed DCS

Finally, I demonstrate and validate that the CDCS system can accurately measure blood flow changes *in vivo*. To this end, I measured the blood flow dynamics on a human forearm during arm cuff occlusion using CDCS and conventional DCS instruments. In vivo experiments were approved by the Institutional Review Board of the University of South Florida (Protocol number Pro00039832_CR000002, approved 11/16/2021). Figure. 3.8 shows a schematic of the experiment. An optical probe (described earlier) was placed on the forearm of an adult volunteer (male, 25 years old), and was connected to the light source and single photon counting detectors using fiber optic cables. The output of the detector (i.e., TTL pulses for each detected photon) was connected to both the CDCS system (i.e., BCD counters) and a conventional DCS software

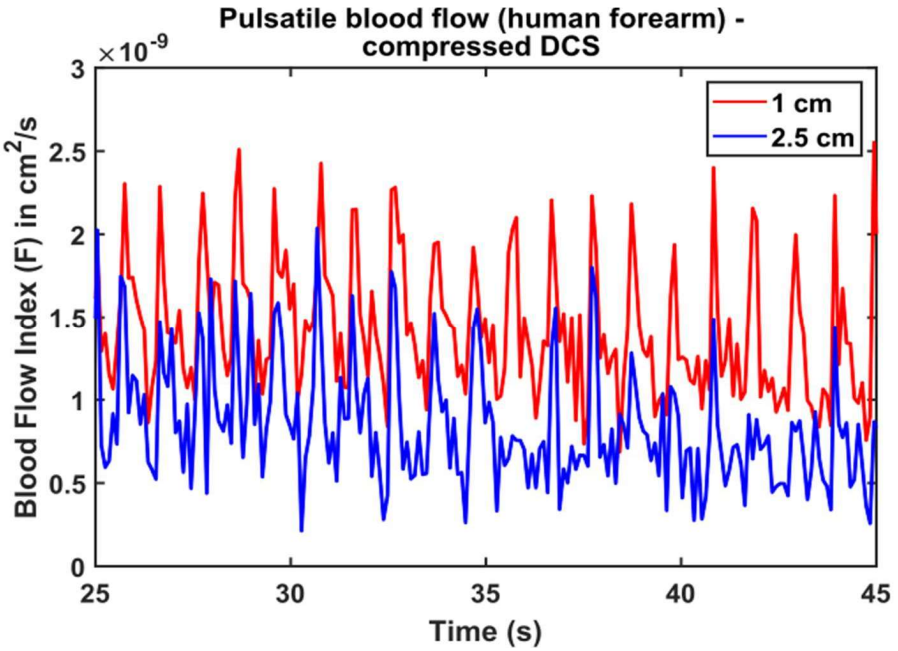

Figure 3.9 Pulsatile blood flow measured on a human forearm with compressed DCS. The red/blue lines indicate time courses of blood flow indices measured at source detector separations of 1 cm/2.5 cm. Both cases can clearly resolve flow changes similar to to the QRS peak and the dicrotic notch.

correlator (NI-DAQ counters). Data acquisition was realized using custom LABVIEW software for both instruments. An arm cuff was wrapped over the subject's bicep and was connected to an automatic pump (A.T.S. 4000, Zimmer, USA). The experiment protocol consisted of a 1-minute baseline, a 1-minute occlusion period (arm-cuff inflated to 200 mmHg), and a 1-minute recovery period. Laser power was controlled to be within ANSI limits of safe exposure for skin [74].

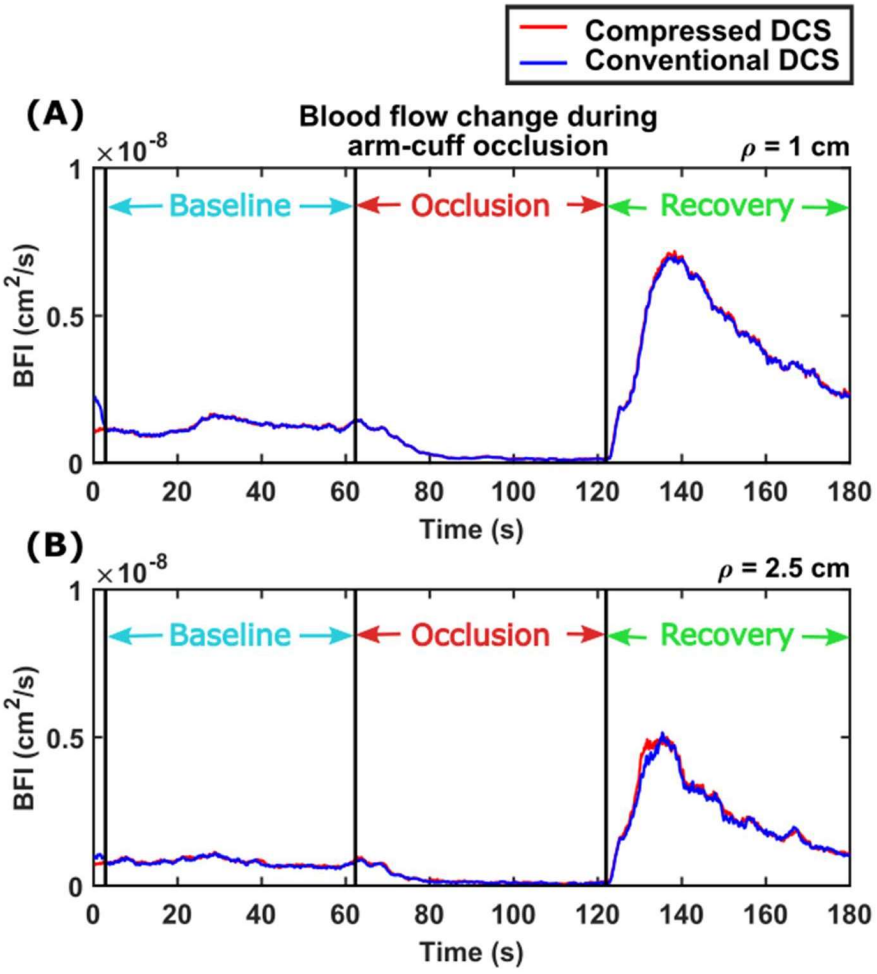

Figure 3.10 Quantitative changes in forearm blood flow measured during an arm-cuff occlusion with compressed (red curve) and conventional (blue curve) DCS systems. The time courses of blood flow indices are averaged with a 20-point (2 second) moving average window. (A) represents the blood flow changes measured at source-detector separation $\rho = 1$ cm and (B) represents the blood flow changes measured at source-detector separation $\rho = 2.5\ cm$. Blood flow changes measured with compressed and conventional DCS systems are in good agreement with each other, both records almost 100% reduction in blood flow during occlusion, and a strong reperfusion response during the recovery period.

DCS intensity autocorrelation functions were recorded at $10Hz$ using both systems, and a blood flow index was computed by methods described earlier. Figure. 3.9 shows a representative time course of blood flow dynamics measured with the CDCS system under baseline conditions. Blood flow measured at both 1cm, and 2.5 cm source detector separation show dynamic blood flow changes; the pulsatility of blood flow due to the heartbeat is clearly resolved. In addition, some high frequency waveform features similar to the QRS peak and the dicrotic notch are well resolved; the dicrotic notch represents a transient increase in blood pressure and blood flow following the closure of the aortic valve in the cardiac cycle. I note that the noise in the measurements is greater at 2.5 cm source detector separation. This is expected as the measured photon count rates are lower for longer source-detector separation. The pulsatile blood flow measurements demonstrate that the CDCS system can resolve small flow changes and can be used for high-speed blood flow measurements. These results are similar to our prior work on pulsatile blood flow detection with conventional DCS systems [47], [73].

Figure 3.10 shows the results of the arm-cuff occlusion experiment, for source-detector separations of 1 cm (Figure 3.10(A)) and 2.5 cm (Figure 3.10(B)). The time course of the blood flow index is displayed during three phases of the experiment – baseline, occlusion, and recovery. Time courses of the blood flow index were smoothed with a 20-point (2-second) moving average window. The dynamics of blood flow changes are clearly visualized by both CDCS (red curve) and conventional DCS (blue curve). During the 1-minute occlusion phase, blood flow reduces by almost 100%, which is accurately measured with the CDCS system. Both CDCS and conventional DCS systems also track the reperfusion in blood flow in the recovery phase. Notably, the data compression does not impact the estimated blood flow indices over a large flow change, showing that the CDCS has a dynamic range comparable to conventional DCS instruments.

3.5 Discussion

Here, I have described a new approach to high-speed sampling of DCS photon counts and fast software computation of intensity autocorrelation functions using resource- and cost-efficient data acquisition units. The key innovation is developing a data compression approach (Section 3.4) that identifies and exploits inefficiencies in conventional photon counting for DCS. The lossless data compression is 87.5% efficient and can be implemented using simple, low-cost digital circuits. I validated the accuracy of blood flow measured with the CDCS system with experiments on tissue simulating phantoms (Figure 3.3-3.5). I further characterized and validated the signal-to-noise ratio of measured DCS intensity autocorrelation functions, by comparing the performance of the CDCS system to conventional DCS systems, and by fitting measurement noise to a DCS correlation noise model (Figure. 3.6). Finally, I performed in vivo validation of the CDCS system, by measuring the blood flow dynamics in a human forearm during arm-cuff occlusion. The demonstrations of blood flow pulsatility (Figure 3.9) and measurements of larger blood flow changes (Figure 3.10) *in vivo* highlight the sensitivity and dynamic range of the CDCS system. In all cases, the performance of the CDCS system met benchmarks set by conventional DCS instruments.

The current implementation of the CDCS approach, used a generic multi-function data acquisition device to read photon-counts off the BCD counters as a stand-alone realization of the CDCS instrument. Critically, the data compression (photon counting with an array of BCD counters) can be readily implemented in other realizations of fast DCS instruments, such as those that use FPGAs [62], [63], FFT-based software correlators[75], [76], or multi-core microcontroller

units/MCUs (e.g., Texas Instrument TMS320F28379D, Infineon TC275Dx) that are capable of multithreaded operations for real-time sampling of DCS photon counts and computation of blood flow indices [77]. Since the data compression occurs at the photon counting stage, I expect our approach to be just as effective in any implementation of DCS.

More generally, the data compression approach presented here can be extended to other high-speed photon counting applications, with optimizations to account for the highest expected photon count rate. Per optical techniques, typical photon counting APDs have a response time of 25 ns and a 'dead-time' of 50 ns, which translates to a maximum detectable count rate of 10-13 MHz (i.e., 10-13 counts/μs) [47] – this is within the capability of the BCD counter. Thus, the compressed photon counting approach can be readily adapted to other optical technologies such as Fluorescence Correlation Spectroscopy, time-domain NIRS, or fluorescence lifetime measurements.

Finally, I note a few design considerations and limitations of the CDCS approach. The current implementation of CDCS used 4-bits of the BCD counter to sample photon counts from one channel. Eight such channels form a single 32-bit number recorded via a digital I/O line. Scaling this approach to more channels would require the availability of several such digital lines. Practical implementations of these lines will be straightforward in FPGAs or dedicated digital I/O boards but will also require careful bit-wise operations to parse the data accurately, and sufficient data throughput to transfer the counts. The bandwidth required for transferring 32-bit integers (i.e., 8 channels) every μs over 1 second is ~3.8 MB/s. Note that the bandwidth requirements for conventional DCS systems in these cases would be 16 times greater. Furthermore, depending on the expected photon count rate, the bits per channel can be reduced to 2, which will help alleviate this limitation. Compared to a standard DAQ counter based acquisition system the CDCS system

may experience some count loss (<2% at 1 MHz sampling frequency) due to the overlapping of TTL pulses with reset duration. However, our experimental results show that this data loss does not affect the calculation of autocorrelation functions or blood flow estimates.

Chapter 4: Fast Diffuse Correlation Spectroscopy with a Low-cost, Fiber-less Embedded Diode Laser

4.1 Introduction

Conventional implementations of Diffuse Correlation Spectroscopy (DCS) use light from lasers with long coherence length to illuminate tissue through long fiber optic cables. Fiber optic cables also collect and direct diffusely reflected light, a few centimeters away from the illumination position on the tissue surface, to photon-counting avalanche photodiode modules for detection. The use of these lasers and detection systems results in a relatively expensive and bulky instrument, especially when compared to more commercial and ubiquitous optical sensors based on NIRS. I and others have recently made several technical improvements to the detection and processing of DCS photon counts that have resulted in simpler and faster instruments. These include fast software autocorrelators[36], [37] and fast field programmable gate arrays/microcontrollers[47], [50] for measuring pulsatile blood flow, as well as new detection systems based on CCD cameras [40], [64], [78], multipixel SPAD arrays [79] and single photo diodes [42], [80]. However, the need to use heavy/bulky laser systems limit the portability of DCS instruments. Here, I report the development of a portable and fiber-less approach that can be used as a low-cost alternative to illuminate tissue in DCS instruments.

[1]This chapter has been adapted from, A. Biswas, S. Moka, A. Muller, and A. B. Parthasarathy, "Fast diffuse correlation spectroscopy with a low-cost, fiber-less embedded diode laser," Biomed. Opt. Express, BOE, vol. 12, no. 11, pp. 6686–6700, Nov. 2021, doi: 10.1364/BOE.435136. Permission is included in Appendix A.

Recently, several studies have implemented illumination systems for DCS with relatively low coherence length laser diode (<1m) to detect deep tissue blood flow [78], [81]. In these experiments, a low-coherence length laser source was coupled directly on top of the skin without the help of a collimation lens. While these experiments exemplified the use of bare laser diode to probe for deep tissue blood flow, they present several key technical challenges such as temperature management and beam divergence. These problems are addressed by the work presented in this chapter and a standard design method is presented for the wide adoption of low-coherence length laser sources for deep tissue flow measurements.

As described earlier DCS blood flow estimates are derived from diffusion-based analysis of the autocorrelation of coherent fluctuations in light intensity backscattered from the tissue surface [3], [82]. Thus, the phase coherence of the scattered field is an essential factor in the design of DCS instruments/light sources [3], [60], [83]. Diffusion theory and Monte Carlo simulations of light transport [84] have shown that the minimum coherence length for DCS light sources must be greater than the pathlength distribution of the photon travel in tissue – estimated to be five to ten times the source-detector separation [43], [83] (e.g., 100 mm for a source-detector separation of 10 mm). Nevertheless, since DCS instruments typically utilize long fiber optic cables, laser sources with significantly longer coherence lengths (~50 m) need to be used, in order to compensate for the additional length of photon travel through the fiber [3], [36]. Given that the coherence requirement is significantly lower than the laser sources traditionally used for DCS measurements, a light source with a relatively low coherence length could help simplify the instrumentation, enable wearable designs, and reduce system costs and power consumption. Here, I have designed one such small-form factor laser system, fiberless DCS (FBDCS), using a single mode laser diode (coherence length ~3.72 m) with a collimating lens to couple the light directly to the tissue surface,

eliminating the need for coherence length overhead introduced by long fiber optic cables. In tissue simulating phantoms and in-vivo experiments, I show that the FBDCS light source compares favorably with fiber-coupled wavelength stabilized laser sources traditionally used in DCS, regarding the accuracy and fidelity of estimated blood flow indices, but also in terms of the signal-to-noise ratio of measured intensity autocorrelation functions.

4.2 Instrumentation

4.2.1 Coherence Length Considerations for DCS Light Source

Since blood flow contrast in DCS arises from temporal fluctuations in the intensity of the backscattered speckle interference pattern, the coherence length of the laser source (l_c) is an important design consideration. For photon correlation measurements based on quasi-elastic light scattering, the dynamics of intensity fluctuations is a function of flow (dynamic scattering) when l_c is greater than the maximum photon travel distance inside the tissue sample [43], [53]. In DCS, the detected speckle pattern is from the coherent addition of an ensemble of light pathlengths. Therefore, the coherence length of DCS light sources should be sufficiently long to account for the spread of light path lengths from the source to the detector in tissue and be greater than the maximum distance the photon travels inside the tissue [43], [83]. While the exact probability

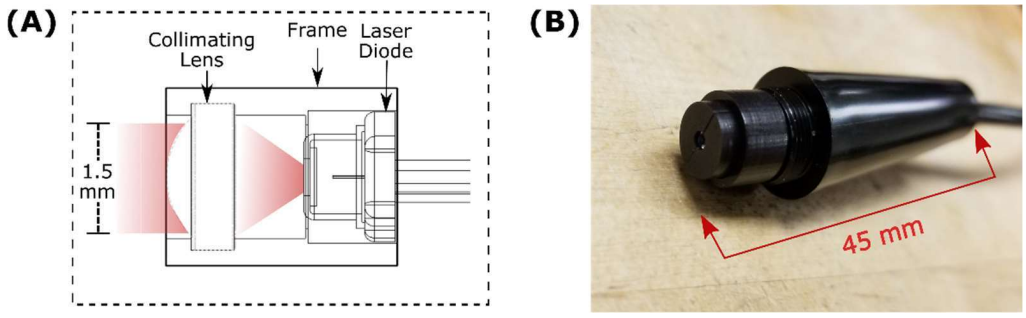

Figure 4.1 Fiber-less laser diode source for DCS. (A) Schematic of the Fiber-less laser source (FBDCS) with an optical assembly consisting of a laser diode (L785P090), a collimating lens enclosed within a custom 3D printed enclosure. (B) A prototype showing the FBDCS source with collimation assembly.

distribution of light pathlengths can be estimated for different tissue geometries using analytical [82] or computational methods [85], [86], a simpler alternative is to utilize the differential pathlength factor (DPF), which when multiplied by the source detector separation (ρ) yields the average distance traveled by the photon inside tissue [85], [87], [88]. Delpy et al. [87], measured the DPF to be 5.3±0.3 for rat brain at 783 nm and ~6 for the human brain at 744 nm; DPFs are typically larger for longer wavelengths [87]. Note that most DCS instruments use lasers at a wavelength of 785 nm. Furthermore, the DPF is independent of source-detector separation for ρ>2.5 cm [87]. Accounting for the variation of DPF with wavelength and tissue optical properties, I conservatively suggest that the coherence length of DCS light sources be at least 10~15 times that of the source detector separation. Most practical DCS systems utilize source-detector separations up to 3.5 cm. Thus, the minimum coherence length of a DCS light source should be 35~50 cm.

4.2.2 Fiber-less Laser Diode Source for DCS (FBDCS)

Considering the coherence requirements of a DCS source, the approach was to build a custom FBDCS using a single mode diode laser. Figure 4.1(A) shows a schematic of the FBDCS source. Light from a single mode laser diode (L785P090, Thorlabs, NJ, 785 nm, 90 mW, 5.6 mm TO can package) is collimated with an aspheric lens (355230-B, Thorlabs, NJ; 4.51 mm focal length, 0.55 NA) to yield a 1.5mm laser beam for use as an illumination source. The laser and lens are aligned and packaged in a custom 3-D printed ABS enclosure (Proto Labs, Inc., USA). The diode was driven by current from a standard laser diode controller (LDC205C, Thorlabs, NJ). At typical operating currents (120 mA) I measured the system's output power to be 65 mW (72% collimation efficiency). enclosure provides electrical and thermal isolation between the diode and tissue. Our prototype's Figure 4.1(B) shows a realized prototype of the FBDCS source, with the

laser diode connected to the current controller using a standard ESD protected strain relief cable (SR9C-DB9, Thorlabs, Newton, NJ).

The laser diode was typically operated near its rated operating current (120 mA) without an optical isolator. Therefore, unpredictable laser mode hops can occur due to feedback at optical interfaces during measurements. However, as the DCS measurements below validate, the laser coherence length during the relatively short DCS correlation interval of relevance (typically < 1 ms) is likely to be more than ~1 m. To verify the coherence properties of the laser, I measured the optical linewidth of the laser diode, in its intended mode of operation, with a scanning Fabry-Perot interferometer (Thorlabs, SA30-73, 1.5GHz FSR), utilizing 10ms sweeps of the full spectral range. The spectrum was fit to the Lorentzian model [89], to measure a frequency bandwidth of 12.8 MHz (full width half maximum, FWHM), and a spectral bandwidth of $\Delta\lambda = 2.61 \times 10^{-14}$ nm. The coherence length was then calculated as $l_c = \frac{\lambda^2}{2*\pi*\Delta\lambda} = 3.72\, m$, here λ is the central wavelength and $\Delta\lambda$ is the optical bandwidth. Thus, the selected single mode diode satisfies the coherence requirements for DCS experiments (>50 cm). To further validate that the laser diode is

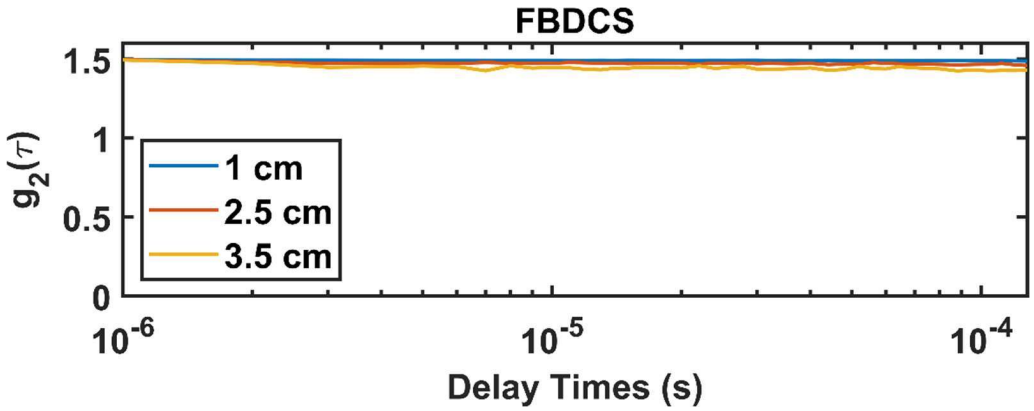

Figure 4.2 Plot showing DCS intensity autocorrelation curves ($g_2(\tau)$) acquired from a solid phantom using the FBDCS source at three source-detector separations. The solid phantom had optical properties of $\mu_a = 0.154\ cm^{-1}, \mu_s' = 4.4 cm^{-1}$ at 830 nm. Results shown are an average of 10 min data collected at a frequency of 5 Hz. A total of 3000 $g_2(\tau)$ frame average is plotted (each frame duration 200 ms).

sufficiently coherent within the timescale of our intended DCS experiments, I measured DCS intensity autocorrelation curves from a solid phantom (750019, ISS Inc., $\mu_a = 0.154\ cm^{-1}, \mu_s' = 4.4 cm^{-1}$ at 830 nm). Light traveling through the solid phantom would experience no dynamic scattering events - thus any decay of the intensity autocorrelation function would be an effect of loss in phase coherence of the source or noise. Figure 4.2 shows the average intensity autocorrelation curves collected from a solid phantom; data were collected at 5Hz for 10 min, photon intensity at source-detector separations of 1 cm, 2.5 cm and 3.5 cm were ~500 KHz, ~100 KHz and ~10 KHz respectively. Autocorrelation curves at each SD separation do not decay throughout the DCS experiment (0.1 ms). Laser coherence length measurements and experiments on the solid phantom directly and indirectly validate that the selected single mode diode satisfies the coherence requirements for DCS experiments.

4.2.3 Optical Probe and Diffuse Correlation Spectroscopy Instrument for Validation Experiments

I designed and realized a custom optical probe and DCS instrument to validate the performance of the FBDCS source against a traditional fiber coupled DCS source. Figure 4.3(A)

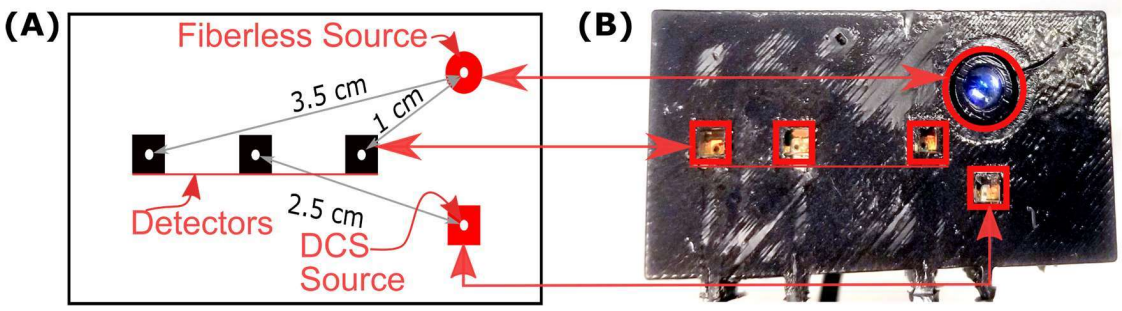

Figure 4.3 Custom optical probe used in validation experiments. (A) Schematic of the validation probe consisting of the fiber-less DCS source (red circle) and traditional wavelength stabilized fiber coupled DCS source (red square) at equal distances from three DCS detector fibers (black squares) placed 1 cm, 2.5 cm, and 3.5 cm away. (B) A prototype of the experimental validation probe incorporating the laser source and detector fibers.

Table 4.1 Flow indices measured from liquid phantom using both fiber-less (FBDCS) and wavelength stabilized sources (WSS).

Source-detector separation	Flow index F $(cm^2/s$ $)$	
	FBDCS	WSS
1 cm	(0.89±0.04)×10^(-8)	(0.89±0.04)×10^(-8)
2.5 cm	(0.84±0.13)×10^(-8)	(0.87±0.18)×10^(-8)
3.5 cm	(0.75±0.19)×10^(-8)	(0.84±0.19)×10^(-8)

depicts the schematic of the validation probe with two sources: the red circle denoting the position of the FBDCS source and the red square denoting the position of a multi-mode fiber (GIF625, Fiberoptic Systems Inc, USA). The multi-mode fiber was connected to a traditional fiber coupled wavelength stabilized source (WSS) (Toptica Photonics, iBeam Smart, 785nm, 120mW, $l_c > 50\ m$). The probe was configured with three source detector (SD) separations, diagonal distances of 1 cm, 2.5 cm, and 3.5 cm from both sources. At each detector position (denoted by black squares), one or more collocated single mode fibers coupled light to a standard DCS detector (Avalanche photo diode modules, SPCM-AQ4C, Excelitas). Both source and detection fibers were affixed to a prism at the proximal end for ease of light-tissue coupling. DCS autocorrelation functions were computed from all detectors simultaneously using a custom software correlator [36]. Autocorrelation functions derived from the same source-detector position were averaged. Experiments were performed by sequentially illuminating the tissue with the two sources.

Figure 4.3(B) depicts a realized prototype of the validation probe manufactured by methods described elsewhere [29]. Briefly, prism coupled single (for detectors) and multi-mode (for WSS source) fibers along with the FBDCS source were placed per the schematic in a custom 3D printed

mold (RenShape SL 7820, Proto Labs, Inc., USA). A two-part silicone elastomer (VytaFlex, Smooth-On, USA) was mixed with carbon black (JAC-JPX1640, Jacquard, USA) and poured into the mold and cured for 12 hours to realize the validation probe.

4.3 Experiments and Results

4.3.1 Blood Flow Index (BFI) Estimated Using the FBDCS Source Is Comparable to a Wavelength Stabilized Laser in a Tissue Simulating Phantom

I first demonstrate that the FBDCS source can measure DCS intensity autocorrelation functions at multiple source-detector separations and validate the blood flow indices (BFI) estimated using the FBDCS as the light source by comparison to traditional DCS sources. The

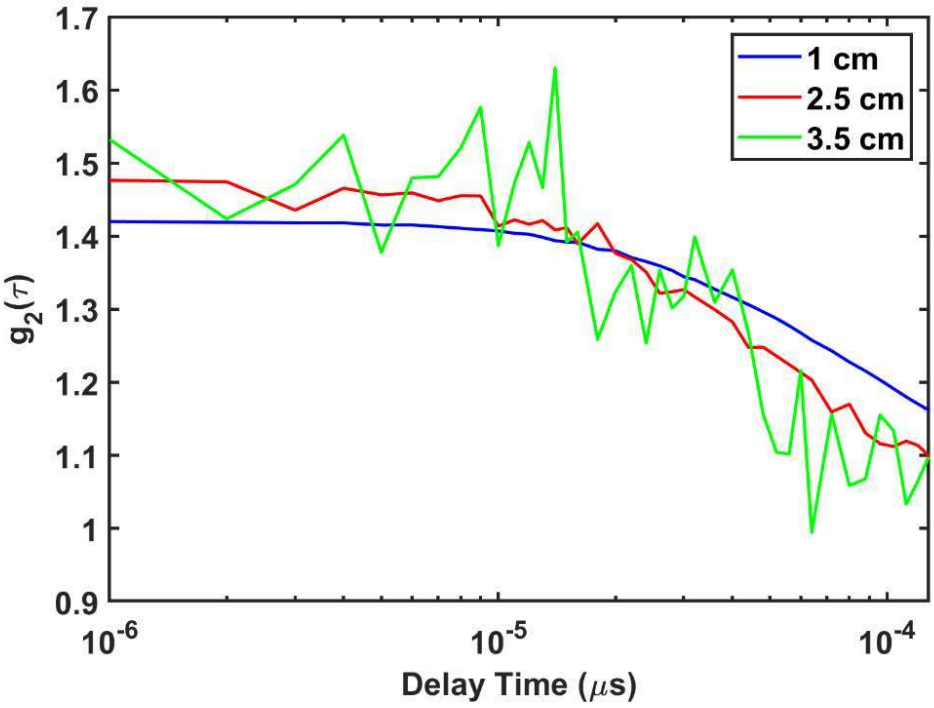

Figure 4.4 Representative DCS intensity autocorrelation functions recorded using the fiber-less laser diode source (FBDCS) from a tissue simulating liquid phantom at source detector separations of 1 cm (blue curve), 2.5 cm (red curve) and 3.5 cm (green curve). Autocorrelation curves were recorded at 10 Hz. Each curve is an average of 50 temporal frames with each frame consists of photon collection over 100 ms.

optical probe (Figure 4.3) measured intensity autocorrelation functions from a tissue simulating liquid phantom. The liquid phantom was prepared from Intralipid (20% emulsion, Sigma-Aldrich, MO), India ink and distilled water, to realize a sample with an absorption coefficient $\mu_a =$

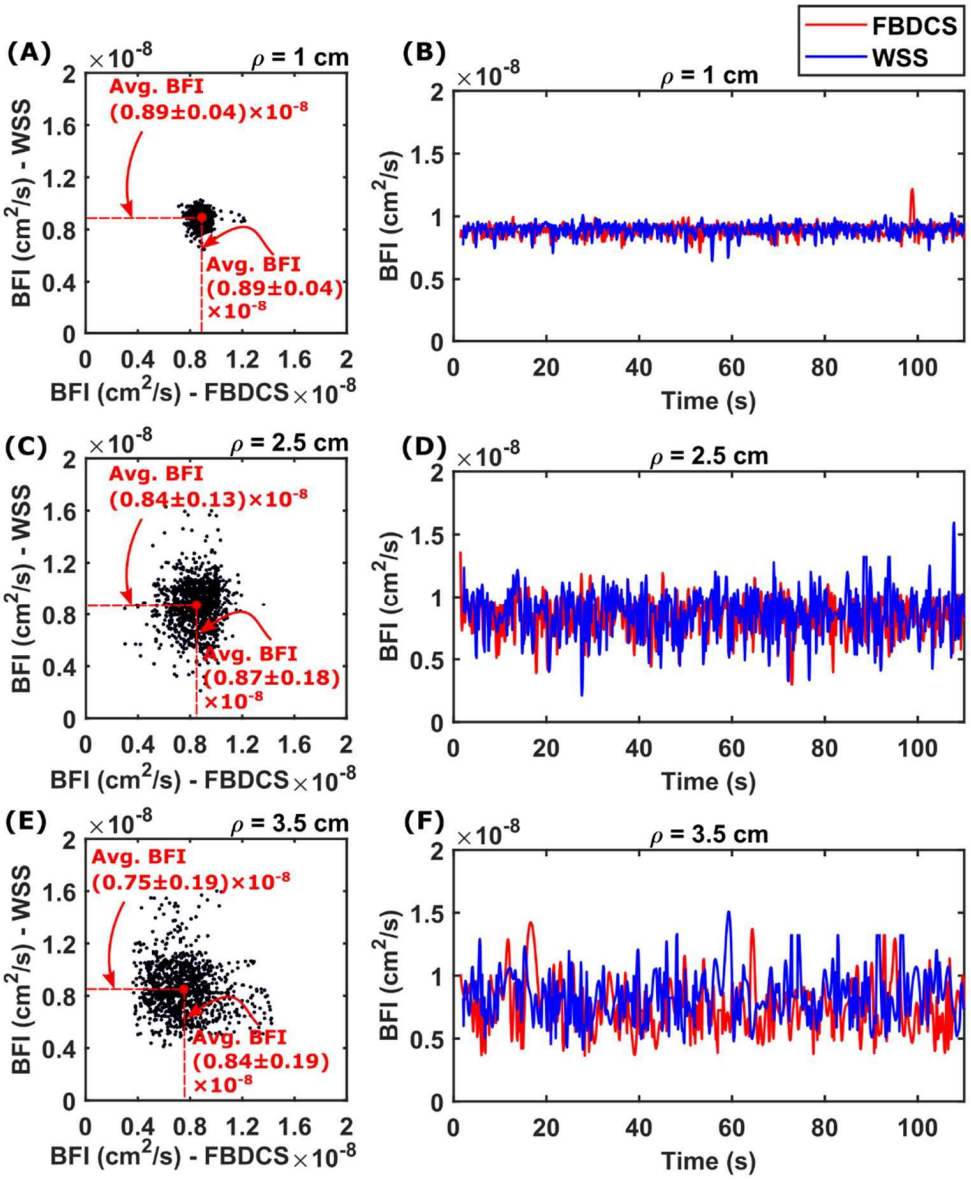

Figure 4.5 Comparison of flow measured from tissue simulating phantom using the fiber-less (FBDCS) and wavelength stabilized (WSS) laser sources. Time courses of flow indices measured at source detection separations 1 cm, 2.5 cm and 3.5 cm are shown in (B), (D) and (F) respectively. Panels (A), (C), and (E) show scatter plots comparing the flow measured with one source against the other. The scatter plots highlight that the mean flow measured with the two sources are in good agreement, with symmetrical spreads in flow estimates along both dimensions.

$0.1\,cm^{-1}$ and reduced scattering coefficient $\mu_s' = 10\,cm^{-1}$ at 785 nm. DCS intensity autocorrelation functions were recorded from both sources (FBDCS and WSS) asynchronously for 120 seconds each, at an acquisition frequency of 10 Hz. A blood flow index (F) was computed by

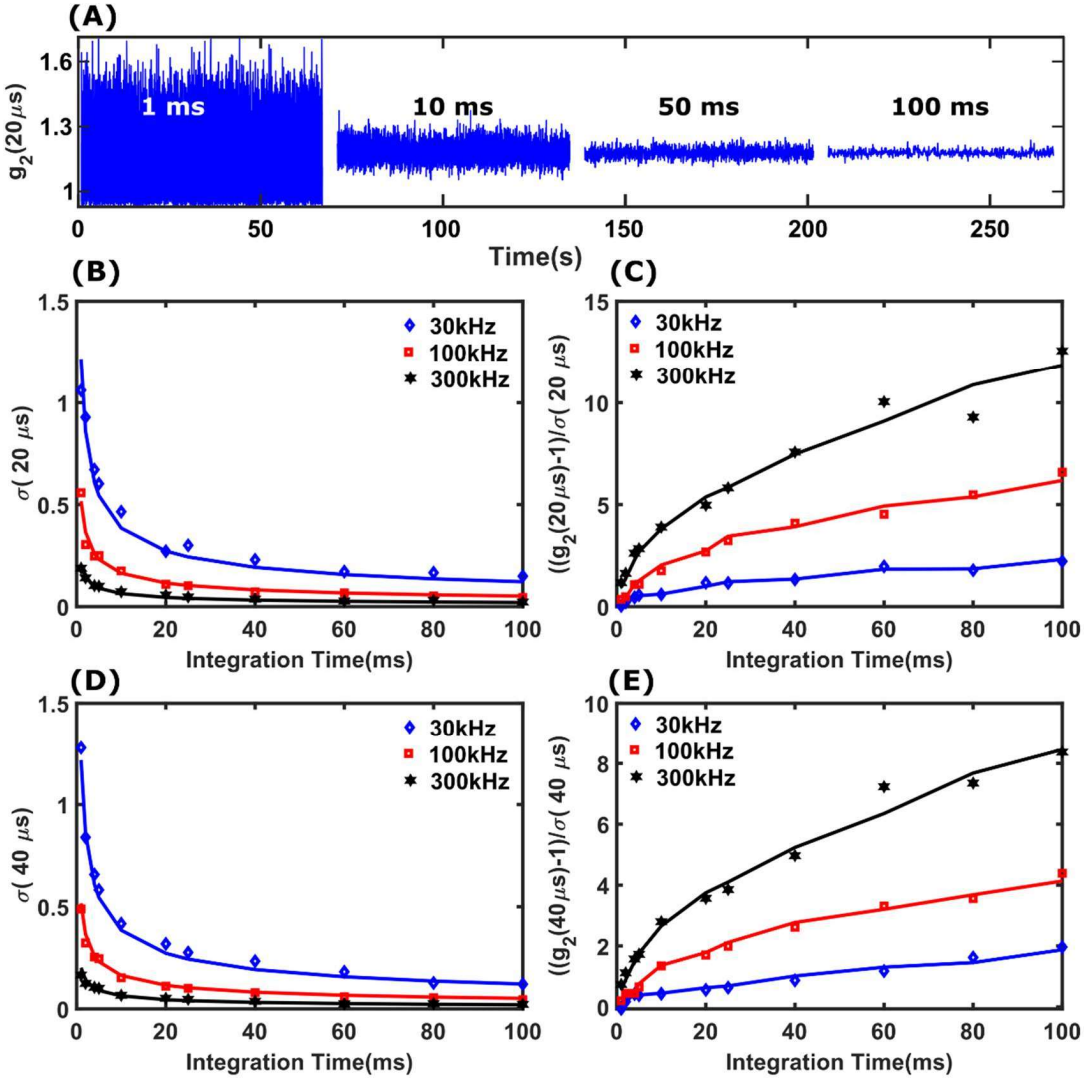

Figure 4.6 Experimental measurement of signal-to-noise ratio of DCS intensity autocorrelation functions with the fiber-less DCS (FBDCS) source. (A) Representative fluctuation of the measured autocorrelation function at delay time $20\,\mu s$ for integration times 1ms, 10ms, 50ms and 100ms. Longer integration time increases the averaging of measurements and reduces noise. (B) and (D) Noise in measurement of $g_2(\tau)$ for delay times $20\,\mu s$ and $40\,\mu s$ respectively. (C) and (E) SNR of $g_2(\tau)$ measurements for delay times $20\,\mu s$ and $40\,\mu s$ respectively. The noise and SNR estimates for photon count rates of 30 KHz, 100 KHz and 300 KHz are marked with blue, red and black markers respectively, while the corresponding solid lines are fits to a DCS correlation noise model.

fitting the measured intensity autocorrelation functions to the solution of CDE in Equation 2.2. The measurements were performed at room temperature.

Figure 4.4 displays representative DCS intensity autocorrelation functions measured from the liquid phantom at three source-detector separations, $\rho = 1\ cm$ (blue curve), 2.5 cm (red curve), and 3.5 cm (green curve). These curves are a 50-frame average of intensity autocorrelation functions measured at 10 Hz. Each frame consists of the photon collection for 100 ms at a sampling frequency of 1MHz. The average photon intensity was 490 KHz, 43 KHz, and 4 KHz at each source-detector separation, respectively. An exponential decay of the intensity autocorrelation function is observed, typical of Brownian motion of fat particles in the intralipid. Notably, these curves were comparable to those measured with the WSS.

Figure 4.5 displays each source's estimated blood flow indices from the liquid phantom. Figures 4.5(B), 4.5(D) and 4.5(F) show the time courses of the flow index throughout the experiment at source detector separations of $\rho = 1\ cm, 2.5\ cm$ and $3.5\ cm$ respectively. In each plot, the flow index measured by the FBDCS source is indicated by the red curve, while those measured with the WSS source are in blue. The curves have been smoothed with a 20-frame moving average filter. At all three source-detector separations, the flow indices measured by the FBDCS compare favorably with those measured with the WSS, highlighting that a fiber-less diode laser source can accurately and quantitatively estimate blood flow. A more quantitative comparison of the respective blood flow indices is depicted in the scatter plots in Figures 4.5(A), 4.5(C) and 4.5(E). Here, the blood flow index measured with the FBDCS source is plotted along the x-axis, while those measured with the WSS source are along the y-axis. The distribution of flow indices are symmetric about the mean (indicated by the dashed red lines) in both directions,

indicating good one-to-one agreement between the sources. Table 4.1 summarizes the mean and standard deviation of flow indices estimated from the liquid phantom using both FBDCS and wavelength stabilized sources (WSS). A two-sided two-sample t-test (MATLAB, Mathworks, USA) revealed no statistically significant difference in the mean flow measured by the two sources ($p > 0.05$) for 1 and 2.5 cm source detector separation. Statistical testing was unreliable for measurements at 3.5 cm due to the higher incidence of noise. The measurements are noisier at longer source-detector separations (both sources) because of decreased measured photon intensity.

4.3.2 SNR of Intensity Autocorrelation Function Measurements Are Comparable Between FBDCS and WSS.

Our second validation experiment concerns the signal-to-noise ratio of intensity autocorrelation functions measured using the FBDCS. The DCS correlation noise model offers a framework to evaluate the SNR of the measured intensity autocorrelation function as a function of measurement integration time (or measurement speed) and measured photon intensity [70]. Accordingly, I define noise ($\sigma(\tau)$) as the standard deviation of the intensity autocorrelation

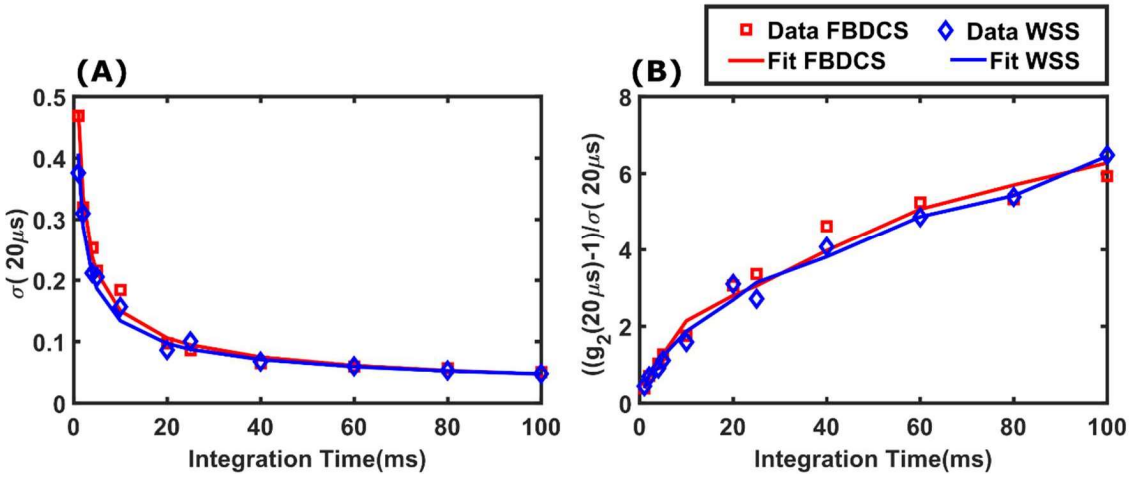

Figure 4.7 Comparison of noise (A) and signal-to-noise ratio (B) of DCS intensity autocorrelation functions measured using the fiber-less source (FBDCS, red markers) and the wavelength stabilized source (WSS, blue markers). Solid lines are fits to a DCS correlation noise model [70].

function $g_2(\tau)$ and $SNR(\zeta(\tau))$ as $\zeta(\tau) = ((g_2\,(\tau) - 1))\,/\,\sigma(\tau)$. DCS intensity autocorrelation functions were recorded from the tissue simulating liquid phantom with the FBDCS source, at source detector separation of 1 cm. In separate measurements, the optical power of the laser was varied to effect a measured photon count rate of 30KHz, 100KHz and 300KHz. At each power level, intensity autocorrelation functions were recorded at different integration times ranging from 1ms to 100ms. Figure 4.6 shows the noise and SNR of the measurements for 20 μs and 40 μs delay times. Figure 4.6(A) shows the representative decrease in variability of $g_2\,(\tau)$ with increasing integration time at delay time of 20μs. Figures 4.6(B) and 4.6(C) show the noise and SNR of the $g_2(\tau)$ measurements at $\tau = 20\mu s$ respectively; Figures 4.6(D) and 4.6(E) show the corresponding curves for $\tau = 40\mu s$. In each panel, measurements at 30KHz, 100KHz and 300KHz are indicated

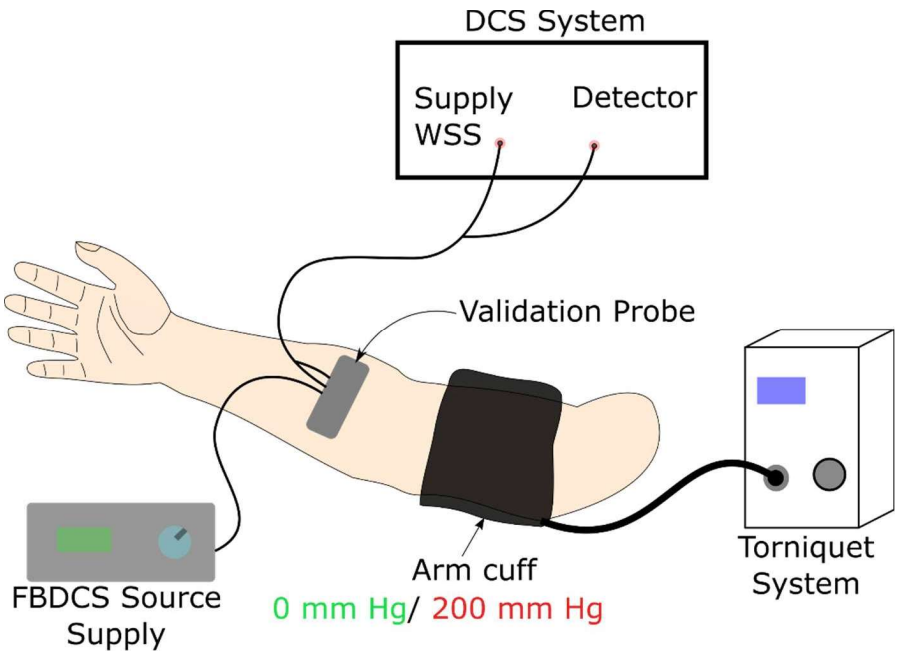

Figure 4.8 Schematic illustrating the in-vivo cuff-occlusion experiment. The validation probe (Figure 4.3) was placed on the forearm of a volunteer, with the detectors centered on the radial artery and two sources illuminating the artery from either side. The distal end of the validation probe was connected to a standard DCS instrument. An arm cuff (connected to a tourniquet system) was wrapped around the bicep to effect transient cuff-ischemia.

by blue, red and black markers, while the solid blue, red and black lines are fits to a DCS correlation noise model [90, p. 2020]. As expected, the noise of correlation measurements decreases (and SNR increases) with an increase in integration time and photon count rate. At 30KHz photon count rates, an SNR of 1 is achieved at integration times of 20 ms for $\sigma = 20\ \mu s$ and 40 ms for σ=40 μs. These results are similar to those obtained with standard DCS instruments [36], [90].

Figure 4.7 compares the noise and SNR of $g_2(\tau)$ measurements obtained with FBDCS and WSS sources. Noise and SNR were estimated from sequential measurements of $g_2(\tau)$ with the FBDCS and WSS source, with source optical powers varied to effect a 100 KHz photon count rate at the detector (source-detector separation of 1 cm). Figure 4.7(A) and 4.7(B) display a plot of noise and SNR of $g_2(\tau)$ at $\tau = 20\mu s$; data from the FBDCS/WSS source is indicated with red/blue markers respectively, while the solid lines represent fits to a DCS correlation noise model. The noise and SNR measured with the two sources are remarkably similar, with the FBDCS source showing marginally higher noise at lower integration times.

4.3.3 Blood Flow Dynamics Measured *In-vivo* with FBDCS Are Comparable to Those Measured with WSS.

Finally, I characterized the ability of the FBDCS to measure blood flow dynamics in-vivo and validated it by comparison with a wavelength stabilized source (WSS). I measured deep tissue changes in blood flow in the arm of a healthy volunteer during an arm-cuff occlusion study. The Institutional Review Board approved all experimental protocols at the University of South Florida. Figure 4.8 shows the experiment setup. Briefly, the validation probe (Figure 4.3) was placed on the forearm of a healthy volunteer. A blood pressure cuff, connected to a tourniquet system (A.T.S. 4000, Zimmer, USA), was placed around the bicep and used to produce transient cuff ischemia.

The validation probe was connected to a standard DCS instrument as described earlier. The cuff-occlusion protocol consisted of a 2-minute baseline, followed by a 1-minute cuff ischemia where the blood pressure cuff was inflated to 200mmHg, and a 2-minute post occlusion recovery. The protocol was repeated twice, with tissue illuminated by FBDCS in the first trial and the Wavelength Stabilized Source (WSS) in the second. A 10-minute resting period between trials was observed to restore the arm blood flow to baseline. DCS intensity autocorrelation functions were recorded at 10Hz and fit to Equation 3 to derive blood flow estimates. The source power of both the lasers (FBDCS and WSS) were adjusted to illuminate the tissue with 50mW optical power; this yielded an average photon count rate of 700, 45 and 6 KHz at 1, 2.5 and 3.5 cm source-detector separations respectively.

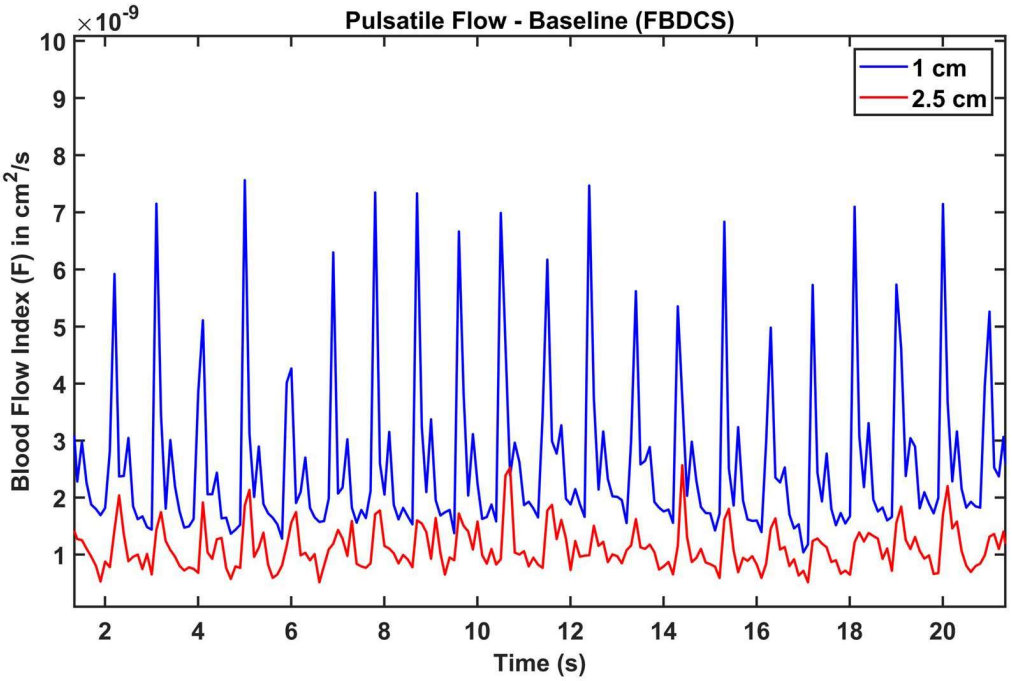

Figure 4.9 Representative time courses of pulsatile blood flow (baseline) measured on a subject's forearm using the fiber-less DCS source. Flow data was acquired at 10 Hz. A clear flow response to the QRS peak (ECG) was observed at both the 1 cm (blue) and 2.5 cm (red) source-detector separations.

Figure 4.9 shows a representative 20 second time course of forearm blood flow measured at baseline using the fiber-less source. Blood flow pulsatility is observed in measurements at both

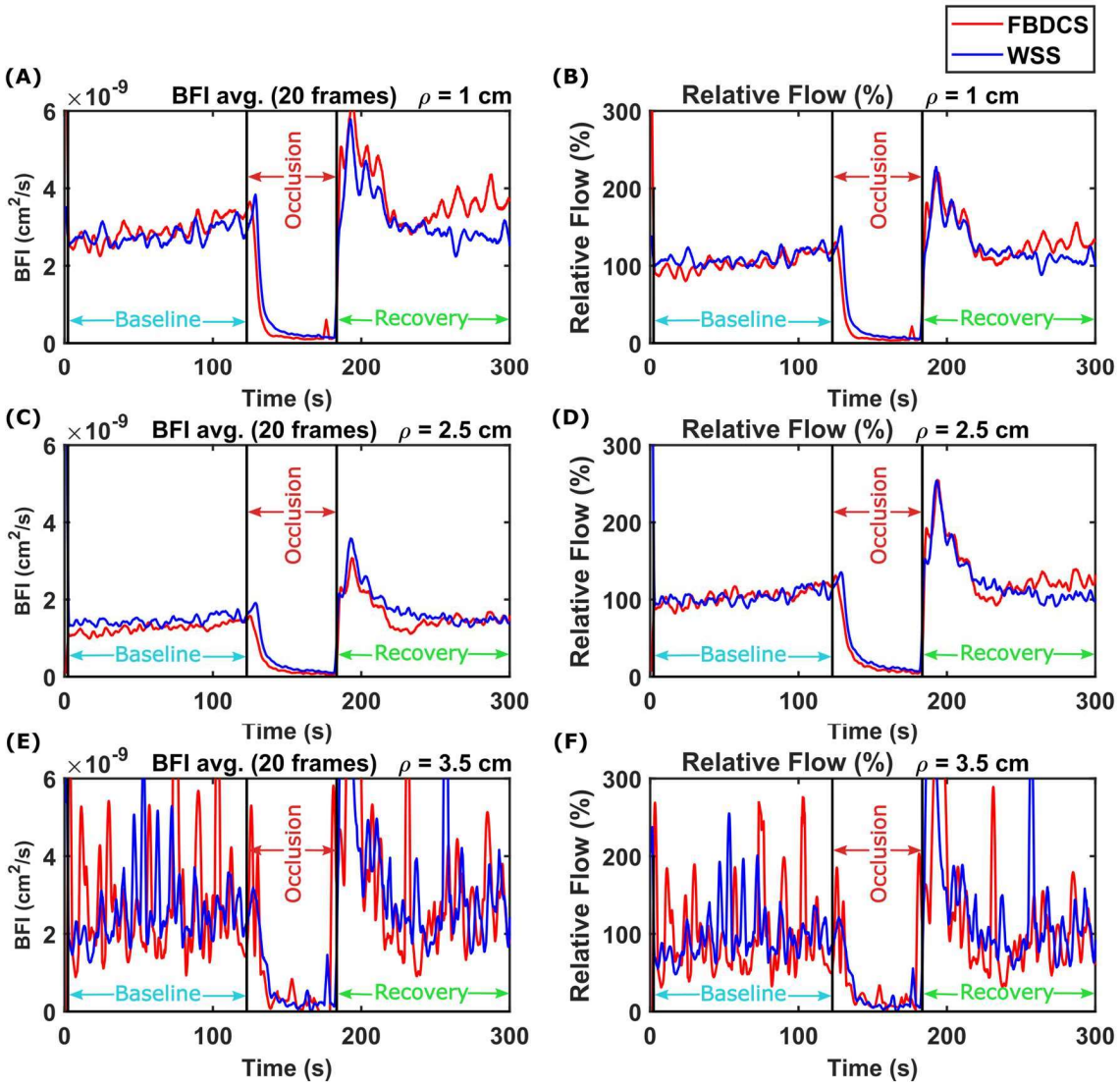

Figure 4.10 Blood flow dynamics due to in-vivo arm cuff occlusion. Panels (A), (C) and (E) show the time courses of blood flow measured source-detector separation of 1 cm, 2.5 cm, and 3.5 cm; panels (B), (D) and (F) show the corresponding relative blood flow changes. In all panels, red lines indicate measurements with the fiber-less DCS source, blue lines indicate measurements with the wavelength stabilized source and vertical black lines indicate occlusion period. The flow indices at SD separation 3.5 cm are noisy due to low photon count rates (both sources). Minor deviations in the flow measured by the two sources can be attributed to the positional difference of the sources relative to the radial artery and asynchronous acquisition.

cm (blue curves) and 2.5 cm (red curves), and a flow response to the QRS peak along with the dicrotic notch is clearly resolved. These results are similar to previous pulsatile arm blood flow [36], [91] measured with traditional fast DCS instruments and highlight the FBDCS source's sensitivity to dynamic blood flow changes *in-vivo*. Figure 4.10 shows the blood flow dynamics measured due to the cuff-occlusion experiment. Here, the blood flow time courses have been smoothed with a 20-frame moving average filter. Figures 4.10 (A), (C) and (E) show the measured blood flow at 1, 2.5 and 3.5 cm source-detector separations, while Figures 4.10 (B), (D) and (F) show the respective relative blood flow changes. In all panels, blood flow measured with the FBDCS source is depicted in red, while those measured with the WSS source are in blue. Two black vertical lines denote the occlusion period. Flow measurements realized by the FBDCS source accurately track a nearly 100% reduction in blood flow due to cuff-occlusion and a transient hyperemic response. These results are similar to those obtained in related studies, as well as the comparison flow changes measured with the WSS source on the validation probe. Minor deviations may be explained by the two sources sampling slightly different tissue volumes. Note that the cuff-occlusion and hyperemic response is resolved at the 3.5 cm source-detector separation despite the significant noise presence.

4.4 Discussion

Traditionally, DCS instruments have used laser sources with very high coherence lengths to compensate for light traveling through multiple path lengths in long fiber optic cables. While these wavelength stabilized laser diode modules are relatively easy to use (often fiber-coupled and 'turnkey'), they can be bulky and expensive. Recently, a few studies have utilized fiber-less designs for DCS blood flow measurements, albeit using traditional long coherence length lasers. For example, Lin et al. reported the development of a dual-wavelength non-contact DCS flow-

oximeter system [92], where the laser source was collimated and projected to the tissue surface via a scanning mechanism. In this contribution, I have demonstrated that DCS blood flow measurements can be reliably and accurately performed with a low coherence length (less than 5 m), off-the-shelf, single mode diode laser. To our knowledge, this is the first time such lasers have been rigorously tested and validated for DCS blood flow measurements.

By direct comparisons to fiber-coupled long coherence length wavelength stabilized lasers, I show that the fiber-less source (a) is accurate in estimating DCS blood flow indices, (b) measures DCS intensity autocorrelation functions at signal-to-noise ratios comparable to wavelength stabilized sources, and (c) can measure dynamic changes in blood flow in humans. The performance of the two sources is nearly identical for source-detector separations of 1 and 2.5 cm, but deviate slightly at 3.5 cm. This is primarily due to the significantly reduced photon intensity and subsequent increase in noise. When corrected for signal intensity, the signal-to-noise ratio of both sources are identical.

I note a few important design considerations for the fiber-less source. Our approach directly couples light into tissue via a collimation lens placed in front of the laser diode. Using a collimation lens is critical because the natural divergence of laser diodes (LDs) is typically too high to yield a measurable signal at the detector. The width of the collimated beam may result in extended-, rather than point-source illumination, leading to speckle averaging at the detector and reduced β. Therefore, narrow beam diameters are preferable provided the laser irradiation is within ANSI limits [70]. When operated at operating powers of ~100 mW, the heat generated in the laser diodes may cause thermal tissue damage. Therefore, continuous real-time flow monitoring with these sources would require efficient thermal isolation between the laser diode and tissue surface. The

designed collimation setup efficiently provides thermal and electrical isolation – care should be observed to use appropriate materials to fabricate these components.

There are several advantages to using a fiber-less diode source for DCS blood flow measurements. First, it dramatically simplifies instrument design and can reduce the cost of DCS sources by as much as 100-fold. Indeed, our approach brings DCS sources to the cost and accessibility of commercial Near Infrared Spectroscopy devices. Second, since the source design significantly reduces coherence requirements, it can be readily adapted to perform DCS blood flow measurements at longer wavelengths (e.g., 1064 nm [93]), where wavelength stabilized sources may be cost- and technologically restrictive. Third, the cost and size advantages of the fiber-less source make it an attractive alternative for large scale Diffuse Correlation Tomography experiments to image blood flow in tissue. Furthermore, the fiber-less source can readily incorporate newer speckle contrast-based detection technologies to effect portable/wearable deep tissue blood flow monitors.

Chapter 5: Integrated Diffuse Speckle Contrast Spectroscopy (iDSCS)– A Novel Deep Tissue Blood Flow Detection Technique

5.1 Introduction

Diffuse Correlation Spectroscopy (DCS) has been at the forefront of quantitative bedside measurement of deep tissue blood flow for many clinical applications. As described earlier, DCS measures blood flow from temporal fluctuations of diffuse photon intensities detected from the tissue surface. These temporal fluctuations are used to calculate the autocorrelation function of intensities, which yields a Blood Flow Index (F) when fit to a diffusion model. Traditional DCS instruments use single photon counting modules to detect photons that have diffused through the tissue. While this approach is robust, use of single photon counting detectors requires bulky power supplies and long fiber optic cables, making it ill-suited for use as a wearable device.

In Chapter 2, I described Laser Speckle Contrast Imaging (LSCI), an optical imaging technique for imaging superficial blood flow from spatio-temporal speckle intensity fluctuations recorded with a camera. Notably, LSCI instrumentation is simple – it only requires a camera and a single mode diode laser. However, it has limited depth sensitivity, and theoretical LSCI models are restricted to single dynamic scattering measurement geometries. Recently, a few groups have leveraged the simplicity of LSCI instrumentation to measure deep tissue blood flow, using diffusion based multiple dynamic scattering models. Two such implementations are Diffuse

[2]This chapter has been adapted from, A. Biswas and A. B. Parthasarathy, "Fast, compact measurement of deep tissue blood flow with integrated diffuse correlation spectroscopy," in Biomedical Applications of Light Scattering X, San Francisco, United States, Feb. 2020, p. 32. doi: 10.1117/12.2546581. Permission is included in Appendix A.

Speckle Contrast Analysis (DSCA)[40], [80] and Speckle Contrast Optical Spectroscopy (SCOS)[41]. DSCA and SCOS utilize detection systems that are simpler and smaller than traditional DCS. However, these techniques still rely on Single Photon Counting Avalanche Photodiode Arrays (SPAD) or CCD/CMOS cameras that are still quite large for probe level measurements. Here, I introduce integrated Diffuse Speckle Contrast Spectroscopy (iDSCS), a novel optical sensor design for probing deep tissue blood flow with a single unbiased, generic photo diode. In iDSCS, a photodiode is coupled to a custom integration circuit to measure photon intensity fluctuations over multiple integration durations. Since the photodiode is unbiased, it has potential to be an inherently low noise device. I further implement real-time noise correction to improve performance. In this chapter, I first describe the underlying concept of diffusion speckle contrast analysis, followed by instrumentation and *in vivo* experimental data.

5.2 Theory

I briefly review the theory of Diffuse Speckle Contrast Analysis (DSCA)[40], [41], [80]. Speckle contrast-based measurements of blood flow calculate the temporal variance of integrated photon intensities. Let $I_t(T)$ be the intensity measured by an integral detector (*e.g.*, camera, iDSCS detector) at measurement time t for an integration time T. DSCA calculates the normalized temporal variance of $I_t(T)$ to estimate blood flow. If, $\sigma_t(T)$ is standard deviation, and $\langle I_t \rangle$ is the mean of n (typically $n = 30$) temporal samples of integrated intensity, then the normalized variance $v(T)$ is given by: $v(T) = (\sigma_t(T)/\langle I_t \rangle)^2$. Note that $\sqrt{v(T)}$ is typically referred to as speckle contrast [39], [56]. Speckle contrast measurement techniques estimate blood flow by measuring the normalized variance at multiple exposure times [46], [56] and fitting it to a speckle visibility expression:

$$v(T) = \frac{\sigma^2(T)}{(\langle I_t \rangle)^2} = \frac{2\beta}{T}\int_0^T \left(1 - \frac{\tau}{T}\right)[g_1(\rho,\tau)]^2 d\tau \tag{5.1}$$

where, β is an instrumentation constant depending on speckle/detector size, coherence length and polarization of the measurement, $g_1(\rho,\tau)$ is the normalized electric field autocorrelation function appropriate to the measurement geometry, F is the blood flow index, ρ is the source-detector separation, and τ is the correlation lag. For the semi-infinite homogeneous tissue geometry, the solution to $G_2(\rho,\tau)$ is given by,[52], [60]

$$G_1(\rho,\tau) = \frac{3\mu_s'}{4\pi}\left[\frac{\exp(-\kappa_D(\tau)r_1)}{r_1} - \frac{\exp(-\kappa_D(\tau)r_2)}{r_2}\right] \tag{5.2}$$

Further, $g_1(\rho,\tau) = G_1(\rho,\tau)/G_1(\rho,0)$, $\kappa_D(\rho,\tau)$ is a dynamic wave vector given by $\kappa_D(\rho,\tau) = [(v\mu_a + 2v\mu_s' k_0^2 F\tau)/D]^{1/2}$, $r_1 = (l_{tr}^2 + \rho^2)^{1/2}$, $r_2 = ((2z_b + l_{tr})^2 + \rho^2)^{1/2}$, $l_{tr} \approx 1/\mu_s'$, and $z_b \approx 2l_{tr}/3$ for index matched boundaries, D is the tissue diffusion coefficient, μ_s' is the reduced scattering coefficient of tissue, and μ_a is the tissue absorption coefficient. In the diffusion regime a closed from solution for the speckle variance can be expressed as a function of integration time (T), and source detector separation (ρ), by substituting for $g_1(\rho,\tau)$ from Equation 5.2 into Equation 5.1,

$$v(T, BFI, \rho) = \frac{2}{T}v^0\left[\frac{1}{r_1^2}I_{2r_1} + \frac{1}{r_2^2}I_{2r_2} - \frac{2}{r_1 r_2}I_{r_1+r_2}\right] \tag{5.3}$$

Here,

$$I_a(T,\rho) = \frac{2}{b^2T}\left[e^{-a\sqrt{bT+}}\left(\frac{2(bT+c)}{a^2}+\frac{6\sqrt{bT+c}}{a^3}+\frac{6}{a^4}\right)\right. \\ \left. + e^{-a\sqrt{c}}\left(\left(bT-\frac{6}{a^2}\right)\left(\frac{\sqrt{c}}{a}+\frac{1}{a^2}\right)-\frac{2c}{a^2}\right)\right] \tag{5.4}$$

Furthermore, $b = 6{\mu_s'}^2\, k_0^2\, (\alpha D_b\,), c = 3\mu_s'\mu_a\,, v^0 = \left[\frac{1}{G_1(\rho,0)}\right]^2\left[\frac{3\mu_s'}{4\pi}\right]^2, r_1 = \sqrt{\rho^2+z_0^2}, r_2 = \sqrt{\rho^2+(z_0+z_b)^2}, z_0 = \frac{1}{\mu_s'}$ and $z_b = \frac{2(1-R_{eff})}{3\mu_s'(1+R_{eff})}$. Here, R_{eff} is the effective reflection coefficient between the tissue and surrounding medium and D_b is the Brownian flow coefficient. The blood flow index $F = \alpha D_B$. A similar expression has been derived for Diffuse Speckle Contrast Analysis by Lee et. al. [94]

5.3 Instrumentation

As it is depicted in Figure 5.1 an iDSCS measurement uses a wavelength stabilized laser as the illumination source. As shown in Chapter 4 – this can be readily replaced with a fiberless single mode laser diode for wearable measurements. Temporal intensity fluctuation of diffused light is collected at different exposure times (T) by configuring a photodiode and op-amp integrator (shown in Figure 5.3). Multiple frames are then used to compute the speckle variance ($K^2(T)$) curve. Finally, the speckle variance curves are fit to equation 5.3 for computing blood flow index (F). The data processing steps are shown in Figure 5.2. Figure. 5.3 shows a schematic outline of the iDSCS optical blood flow sensor, and a schematic of instrument control and data acquisition. The iDSCS sensor uses a generic photodiode (ODD-1W, Optodiode, USA) that features an active detection area of ~1mm^2. The diode is operated in photovoltaic mode, *i.e.*, it is unbiased. Normally,

this reduces the photon-electron conversion rate and diminishes any amplification that may be achieved in the semiconductor. However, operating the photodiode in an unbiased condition also reduces the effective dark current in the sensor. The loss in photodiode amplification is compensated by the integrator amplifier circuit.

The output of the photodiode, *i.e.*, the current generated by the detected photons, is connected to a switched op-amp for integration. Here, I use a general-purpose precision switched integrator amplifier (IVC102U, Texas Instrument, USA) that features a capacitor bank and a MOSFET switch in feedback loop. The output of the amplifier can be modeled as

$$V_{out} = -\frac{1}{C_{int}} \int I_{IN}(t)dt \tag{5.5}$$

where, $C_{int} = 100\ pF$, and I_{IN} is the current from the photodiode. When the MOSFET switch (S1) is open, the amplifier functions as an integrator, and the capacitor accumulates charge. When the

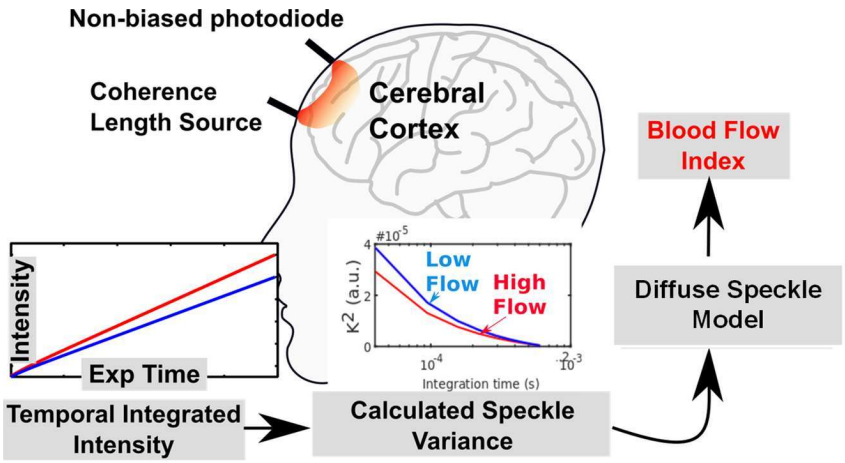

Figure 5.1 Outline of the iDSCS instrumentation. A WSS laser is used as illuminator and an unbiased PN photodiode is configured to temporally integrate light intensity fluctuations. Temporal contrast analysis is performed on data collected following the MESI [55] scheme. Acquired data is then fitted to diffuse speckle model to calculated αD_B

MOSFET switch (S1) is closed by an external control signal, the integration operation is stopped and the capacitor discharges. Thus, the circuit functions as programmable integrator, similar to a camera. Note that the iDSCS circuit can be implemented with *any* operational amplifier with a capacitor and switch in its feedback loop.

Instrument control and data acquisition scheme shown on Figure 5.3 is realized using a multi-function data acquisition board (USB-6341, National Instruments, USA) and custom software on LabVIEW. Two counter/timers on the data acquisition board were configured to generate the necessary timing signals to drive the acquisition process. The first timer was used to operate the integration/reset cycle (shown in red in Figure 5.3(B)). The integration time t_{int} was set to be $500\ \mu s$ and the reset time t_{reset} was set to $100\ \mu s$. This pulse train was used to trigger the second timer and produce a periodic sampling clock, which was used to record the integrated

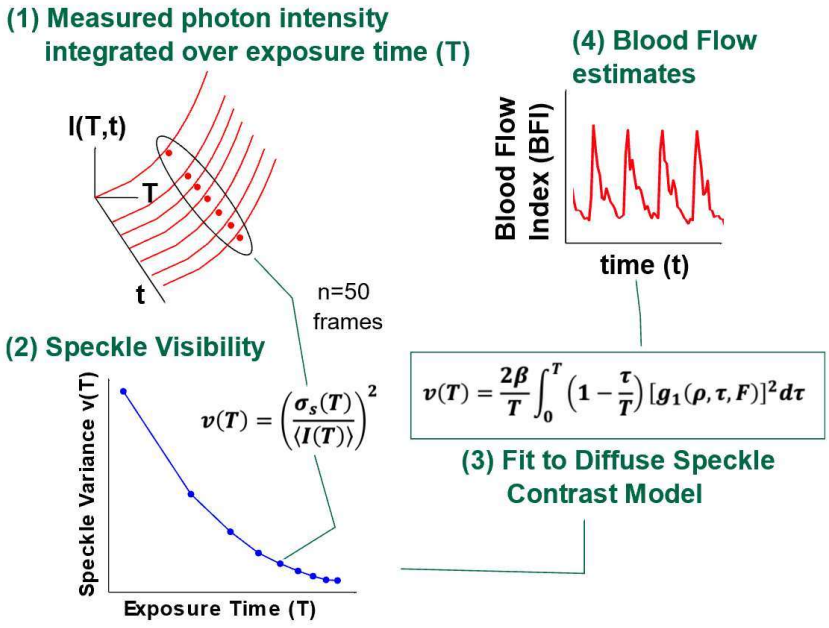

Figure 5.2 During one integration cycle multiple intensity output is sampled following the MESI [55] scheme. Multi-exposure data collected during one integration cycle is defined as one data frame. Multiple data frame is utilized to calculate speckle variance. Finally, fitting these speckle variance curves into the diffuse speckle model results in blood flow information αD_B.

intensities at different exposure/integration times. The sampling clock had a time period of 50 μs, which resulted in *single-shot* measurement of 10 exposures per cycle. A $500\mu s$ integration and $100\mu s$ reset cycle, resulted in an effective measurement frame rate of 1.6 KHz. Note that detection of additional exposures can be readily accomplished by reducing the time period of the sampling clock, without sacrificing data acquisition rates.

Since the iDSCS sensor utilizes an unbiased photodiode, it inherently features the lowest possible dark noise for Si detectors. However, the measurement is susceptible to other environmental and electrical noises such as Johnson noise, shot noise, readout noises etc. I implemented a real-time noise correction procedure to account for the different circuit noises. Note that the first sample acquired per cycle corresponds to a 'zero' integration time measurement, and thus serves as an overall measure of circuit noises. This integrator output measured at zero integration time was subtracted from $I(T)$ to provide a real-time noise corrected integrated

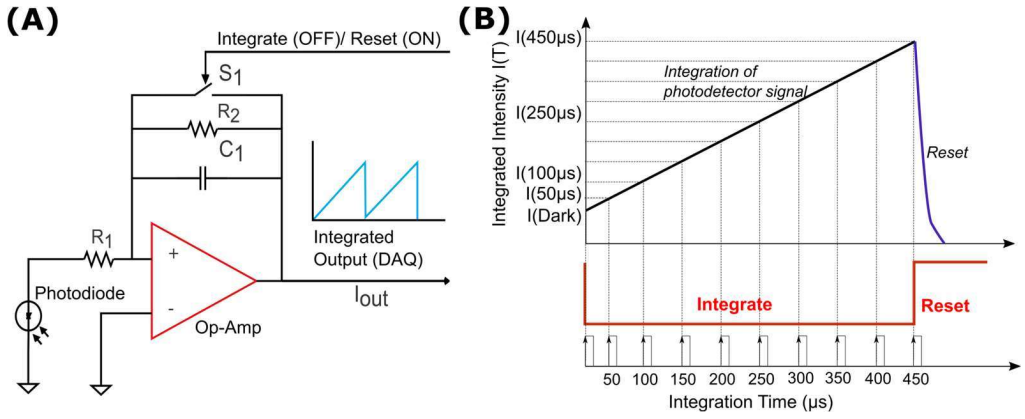

Figure 5.3 (A) Circuit schematic of integrated DCS probe. A generic photodiode is configured in photovoltaic mode. The current generated by incident photons is amplified by a programmable switched op-amp integrator circuit. The operation of the integrator is modulated by a MOSFET switch on the feedback loop (S1), which controls the integration reset cycle (typically $t_{int} = 500\ \mu s$,$t_{reset} = 100\ \mu s$). (B) Sampling and Integration cycle, for single shot measurement of speckle intensity fluctuations at multiple integration times. The maximum integration time is $500\mu s$. Integration and data sampling is realized by a National Instruments data acquisition device controlled using custom software.

intensity data for every cycle. Per data processing, $n = 30$ multi-exposure integrated intensity frames were processed to compute the normalized speckle contrast and variance as a function of measurement time and exposure time. The data was then post-processed by averaging over 100 frames for an effective measurement rate of ~16 Hz. The resulting speckle visibility measurement ($v(T)$) was fit to an analytical solution to equation 5.3, to derive a blood flow index.

5.3.1 Effects of Speckle Averaging and Compensation Techniques

Averaging of multiple speckles over the detection area may reduce the dynamic range of the iDSCS sensor. The size of a speckle is roughly few micrometers [46]. It is a function of observation distance d, central wavelength of light source λ and the detection area a. For a typical deep tissue measurement, the average speckle size is calculated as $s \approx \frac{d\lambda}{a} \approx 300\,\mu m$. If the photosensitive area of the photodiode is larger than the speckle size then the photodiode will experience spatial averaging of multiple speckles. This phenomenon is known as speckle averaging. Now if we model the current generated by the photodiode as $I_t(T)$, then it has a constituent of dc component contributed by the speckle averaging, $I_{dc}(T)$, and an ac component

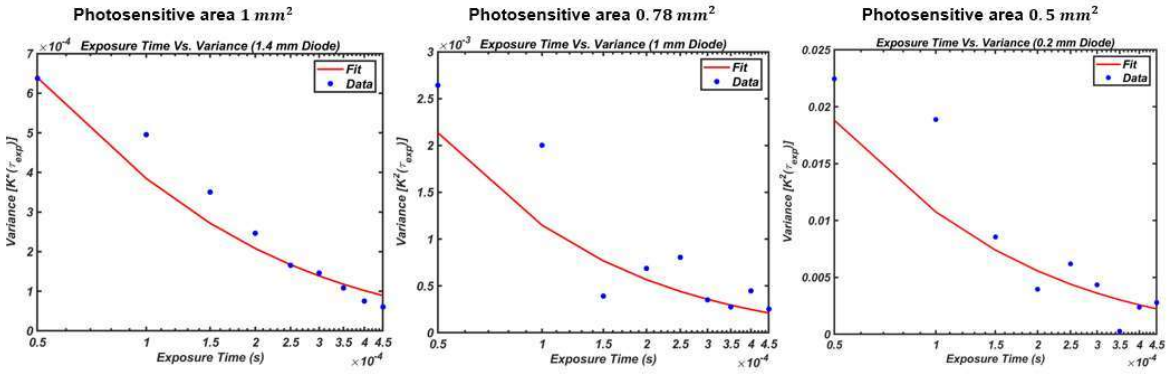

Figure 5.4 Representative curves of speckle variance $K^2(\tau_{exp})$ is plotted for photodiode with different photosensitive area. From left to right the photosensitive area reduces thus reducing the speckle averaging contribution to the signal dynamics. As a result, the speckle variance K^2 and the dynamic range of multi-exposure speckle variance curves improve from left to right.

representative of the dynamic speckle intensities, $I_{sig}(T)$. If the dc current contribution becomes significantly higher that the ac component, i.e., $I_{dc}(T) \gg I_{sig}(T)$, it will cause a reduction in the dynamic range of the speckle visibility curves, thus, reducing the overall sensitivity of the measurement. There are few techniques to tackle speckle averaging. The first technique is to reduce the photosensitive area of the photodetector. Second a current subtraction method designed to negate the $I_{dc}(T)$ component of the total current $I_t(T)$ generated by the photodiode.

A reduced area of photo detection will lessen speckle averaging effects thus improving the speckle contrast. Accordingly, I have prepared three different iDSCS optical probes with three photodiodes of different active area. Next, I measured the speckle visibility curves from a tissue simulating liquid phantom with absorption coefficient $\mu_a = 0.1\ cm^{-1}$ and reduced scattering coefficient $\mu_s' = 10\ cm^{-1}$ at 785 nm. The acquired speckle visibility curves are shown on Figure 5.4 from left to right for photodiode with effective area of 1 mm^2 (ODD-1w, Optodiode, CA), 0.78 mm^2(S9119-01-01, Hamamatsu, Japan) and 0.5 mm^2 (S13337-01, Hamamatsu, Japan) respectively. Here, the measured speckle variance (y-axis) is plotted as a function of exposure time (x-axis). The variance at the shortest exposure time is about an order of magnitude higher for the 0.5 mm^2 active area detector (right most curve) when compared to the 1 mm^2 active area detector (left most curve). It is clearly observed that the overall variance and dynamic range improves as the effective area of the photodiode decreases.

5.3.2 Improving Dynamic Range with Constant Current Sink

Although, reducing the photosensitive area has demonstrated positive results on improving the speckle variance. The photodiode chosen for this experiment were PIN photodiode. PIN photodiode is designed form high speed application in photoconductive mode. Thus, for normal operation a biasing voltage is desired. An added biasing voltage would result in increase in dark

current thus reducing the signal to noise ratio. This reduction in SNR worsens for low light applications. Thus, this detector is not suitable for iDSCS application. iDSCS measurement necessitates a PN diode which features proper photovoltaic mode operation in low light condition with intrinsically low dark and shot noise. This poses a significant dilemma because availability of a PN type photodiode restricted the photosensitive area to be $\geq 1\ mm^2$.

To overcome this limitation, I explored a different strategy to reduce the speckle averaging current in iDSCS acquisition. To reduce the speckle averaging current $I_{dc}(T)$, I designed a custom circuit to sink/drain a current I_d, which when connected to the same node as the photodiode and configured correctly would negate $I_{dc}(T)$. Briefly, an op-amp driven constant current source is connected in the same note as the photodiode. The input terminal of the op-amp is connected to a NI-DAQ 6341 analog output for active current control through a custom LabVIEW program. The

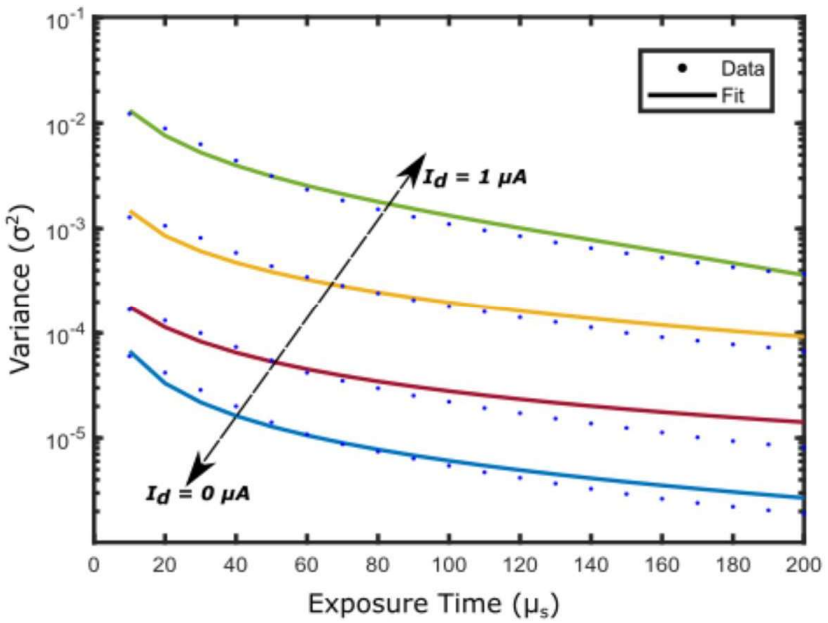

Figure 5.5 Speckle variance curves acquired from a solid phantom experiment by varying the drain current I_d. Different current sink I_d is introduced to the terminal of the photodiode ranging from 0 μA to 1 μA. As the I_d increases the dynamic range of the speckle variance curve improves reaching a peak at $I_d = 1\mu A$, denoting a total subtraction of the speckle averaging current I_{dc}.

output voltage of the NI-DAQ system is converted to the drain current I_d by a series resistance. As I_d approaches I_{dc}, the spackle variance increases consequently increasing the dynamic range of speckle variance curve. In theory, the effect of the dc speckle averaging current should be completely suppressed when I_d becomes equal to I_{dc}.

To validate this approach, I measured diffuse speckle visibility curves from a liquid tissue phantom ($\mu_a = 0.1\ cm^{-1}$, $\mu_s = 10\ cm^{-1}$ at 785 nm) with an optical probe comprising a fiber coupled wavelength stabilized length laser source (Toptica Photonics, 785 nm, 120 mW) and the modified iDSCS detector with a source detector separation of $\rho = 10\ mm$. Multiple integrated speckle intensity curves were recorded as a function of exposure time T from $10\ \mu s\ to\ 200\ \mu s$. A total of 100 such curves were used to calculate the speckle variance. Speckle variance was acquired as a function of exposure time for drain currents ranging from $0\ \mu A$ to $1\ \mu A$; Figure 5.5 outlines

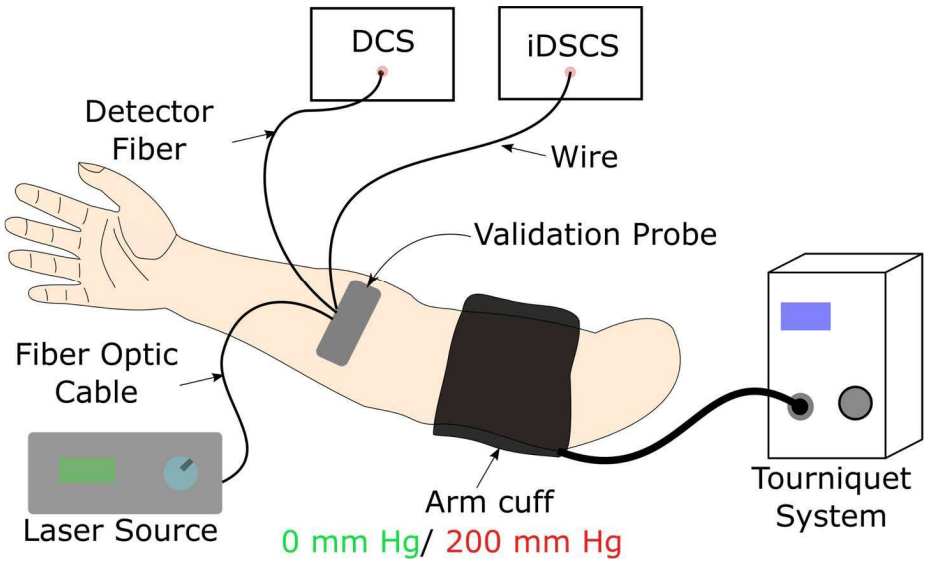

Figure 5.6 Schematic illustrating the in-vivo cuff-occlusion experiment. The iDSCS validation probe was placed on the forearm of a volunteer. An arm cuff (connected to a tourniquet system) was wrapped around the bicep to effect transient cuff-ischemia. The validation probe contains two source fibers placed at an SD of 1 cm and 2.5 cm with the iDSCS detector. A DCS detector fiber is placed at an SD separation of 2.5 cm for comparison study.

speckle variance curves measured with drain currents (I_d) of 0 μA (blue), 0.5 μA (red), 0.9 μA (yellow) and 1 μA (green). The average speckle contrast is lowest when $I_d = 0\ \mu A$ and highest when $I_d = 1\ \mu A$; speckle variance measured at $I_d = 1\ \mu A$ is three orders of magnitude greater than that measured without drain current subtraction. These results clearly show the success of the dynamic contrast enhancement strategy implemented here.

5.4 Experiments and Results

5.4.1 *In-vivo* Arm Cuff Occlusion Study for 1 cm and 2.5 cm with Active Speckle Averaging Drain

Here, I demonstrate the ability of the iDSCS technique to measure deep tissue blood flow using the device with current drain implemented to compensate for the speckle averaging. Figure 5.6 shows the schematic of the *in vivo* experiment. Briefly, the validation probe on Figure 5.6 contains two conventional DCS laser sources (similar as in section 3.5) and one DCS detector fiber, the later provides for comparison with a conventional DCS system. Two source fibers were

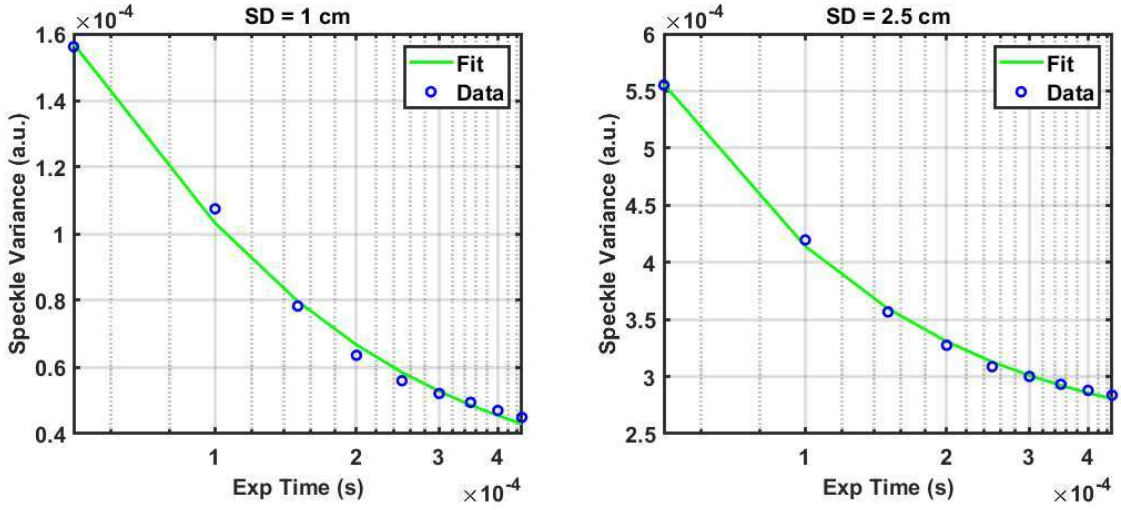

Figure 5.7 Representative variance curve and their fits acquired with the iDSCS validation probe for 1 cm (left) and 2.5 cm (right) SD separation. For the same drain current introduced the variance $K^2(T)$ for SD 1 cm is less in magnitude than the 2.5 cm due to the higher contribution of speckle averaging at shorter SD separation.

placed maintaining a SD separation of 1 cm and 2.5 cm with the iDSCS detector. Asynchronous opeation of the two laser source would probe different depths inside the tissue. A tourniquet system is configured to induce transient arm-cuff ischemia during experiment.

First baseline BFI indices were measured with both devices at SD of 1 cm and 2.5 cm for 1 minute. For iDSCS, the overall time period of acquisition of one frame was set to be $t_{acquisition} = 600\ \mu s$ where the integration time t_{int} was set to be $500\ \mu s$ and the reset time t_{reset} was set to be $100\ \mu s$. In each frame, 10 multi-exposure intensity/contrast measurements were collected for exposure times ranging from $0\ \mu s$ to $450\ \mu s$. Intensities from 50 frames were used to calculate the variance $K^2(\tau)$ curves thus making the effective frame rate to 33 Hz. Before fitting to the speckle variability model 100 frames of speckle contrast were averaged. Figure 5.7 shows representative speckle variance curves (blue dot) and fit (green solid line) for source detector separations of 1 cm (left) and 2.5 cm (right). Here, the data were fit to the diffuse speckle contrast

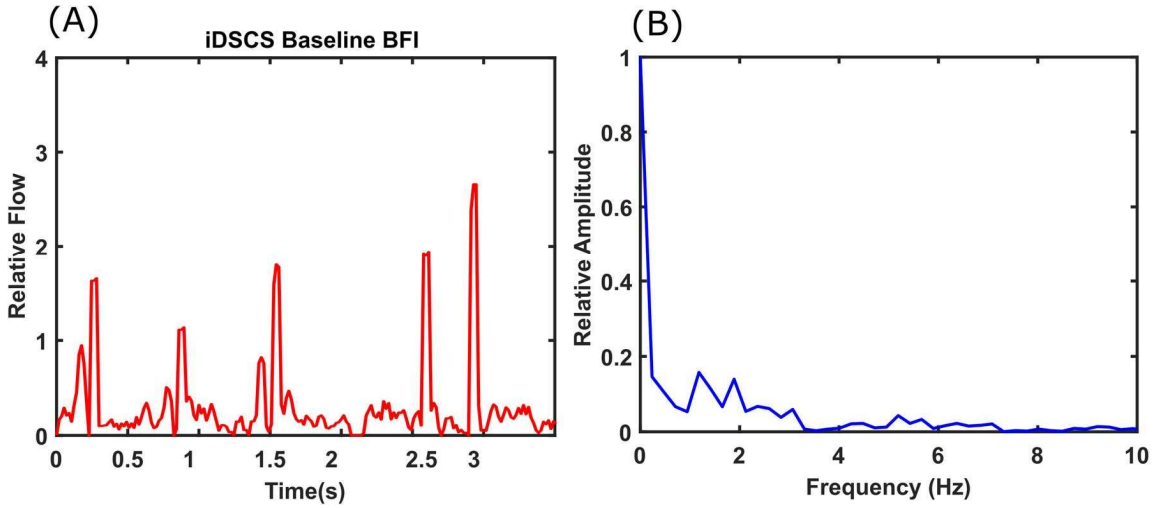

Figure 5.8 (A) Baseline relative blood flow indices showing pulsatile blood flow measured on a subject's forearm measured using the iDSCS detector at an effective frequency of 33 Hz. (B) FFT of the baseline flow showing intensity peak at 1-2 Hz frequency, indicating pulsatility in the detected signal.

model in Equation 5.3. The speckle variance at SD of 1 cm is slightly lower than 2.5 cm due to high intensity detected at lower SD separation reducing signal variability.

Figure 5.8 (A) shows the baseline relative blood flow for a source-detector separation of 1 cm, over a 3.5 second temporal window. At baseline condition the heart rate pulsatility is clearly visible with QRS peak. Figure 5.8 (B) shows the corresponding frequency spectrum of the blood flow; the pulsatile frequencies are resolved in the 1-2 Hz range. This suggests the iDSCS has sufficient sensitivity to measure pulsatile flow at 1 cm SD separation. However, note that typical high frequency features such as the dicrotic notch are not clearly resolved. Better noise correction will help improve iDSCS' sensitivity to small flow changes.

After acquiring the baseline data, a cuff occlusion study was performed for both SD separations. The cuff-occlusion protocol consisted of a 1-minute baseline, followed by a 1-minute cuff ischemia where the blood pressure cuff was inflated to 200mmHg, and finally a 1-minute post occlusion recovery. Cuff occlusion experiments were performed for both SD separation in sequence, allowing for a 10 minute rest period in between. Blood flow indices were computed with

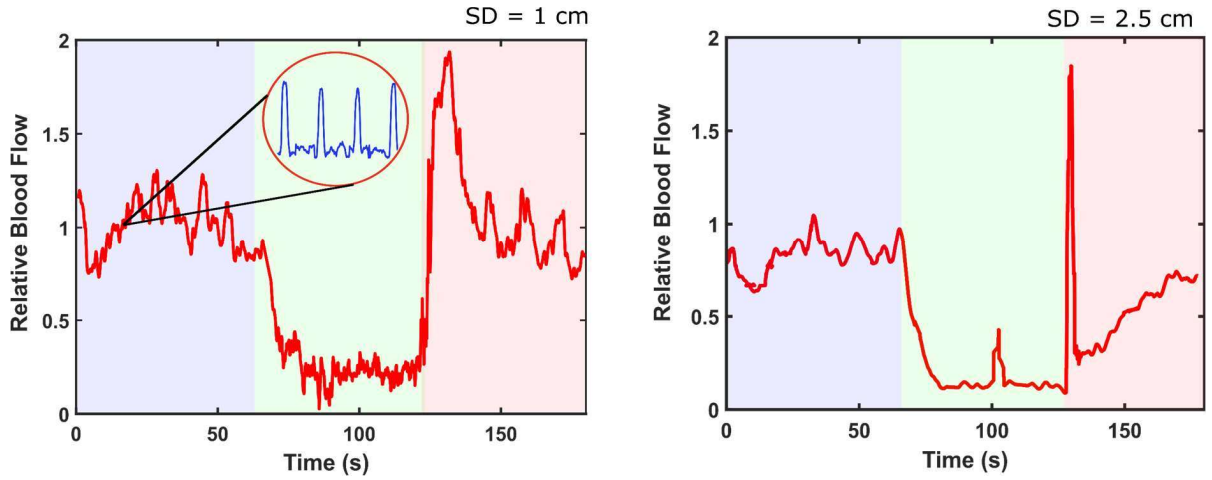

Figure 5.9 Relative BFI plots of arm-cuff occlusion study performed with the iDSCS validation probe. The effective acquisition frequency was 16.7 Hz. For SD separation of 1 cm(left) a ~100% occlusion was detected and for SD of 2.5 cm (right) a ~90% occlusion is visible.

iDSCS using the methods descried above. The time trace of the blood flow was smoothed with a. 20-frame moving average window. Relative blood flow was computed by normalizing to the mean baseline blood flow. The result of this study is shown in Figure 5.9. During the arm cuff occlusion period, a close to 100% occlusion was observed at 1 cm SD separation, whereas ~90% occlusion for SD of 2.5 cm.

I compared the temporal time trace of relative blood flow measured with iDSCS measurement against a conventional DCS instrument. As mentioned earlier, a DCS detector fiber and an iDSCS detector was placed within the validation probe maintaining an equal SD separation of 2.5 cm from a fiber collimated WSS source. A picture of the realized probe can be seen in Figure 5.10(left). I briefly describe the DCS acquisition parameters here. The DCS acquisition frequency was set to 20 Hz and average of 20 frames was taken to demonstrate the relative change in blood flow. The surface illumination power was 70 mW. For each SD separation 3 channels of DCS data

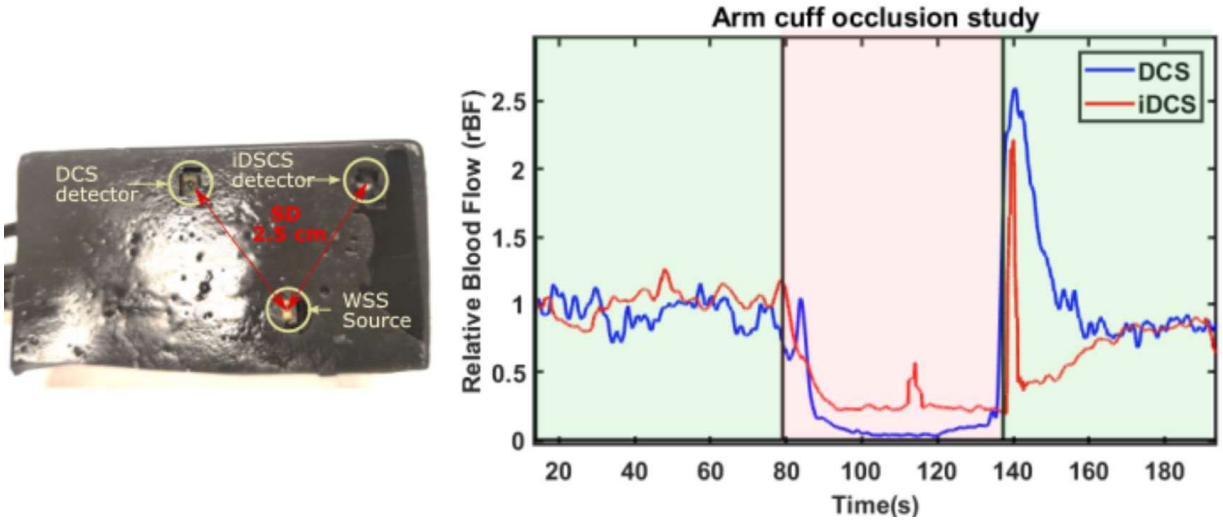

Figure 5.10 A realized validation probe of the modified iDSCS system with comparison study with DCS. A DCS detector fiber and iDSCS detector is molded maintaining a SD of 2.5 cm from a fiber coupled wavelength stabilized source. On right the relative BFI index of an arm-cuff occlusion study is shown. During occlusion the relative BFI is in well agreement with both the measurement iDSCS and DCS.

were averaged to increase the SNR. The iDSCS analysis is similar as described earlier and iDSCS data was acquired synchronously with the DCS measurement. For both measurements the flow indices were normalized with the mean of baseline flow to compute the relative blood flow (rBF). The resultant comparison is shown in Figure 5.10. Both iDSCS and DCS track the blood flow reduction due to the arm-cuff occlusion. DCS, clearly shows a 100% reduction in blood flow, while that measured with iDSCS is ~90%. This discrepancy could arise from the positional difference and iDSCS' lack of sensitivity due to speckle averaging and other measurement noises. As with the previous experiment, better noise correction will help improve iDSCS' dynamic range.

5.4.2 Sensitivity iDSCS Blood Flow Changes Measured in Tissue Simulating Liquid Phantoms

Finally, I experimentally measured the sensitivity of the iDSCS system to flow changes in a controlled liquid phantom. Tissue simulating liquid phantoms were prepared from distilled water,

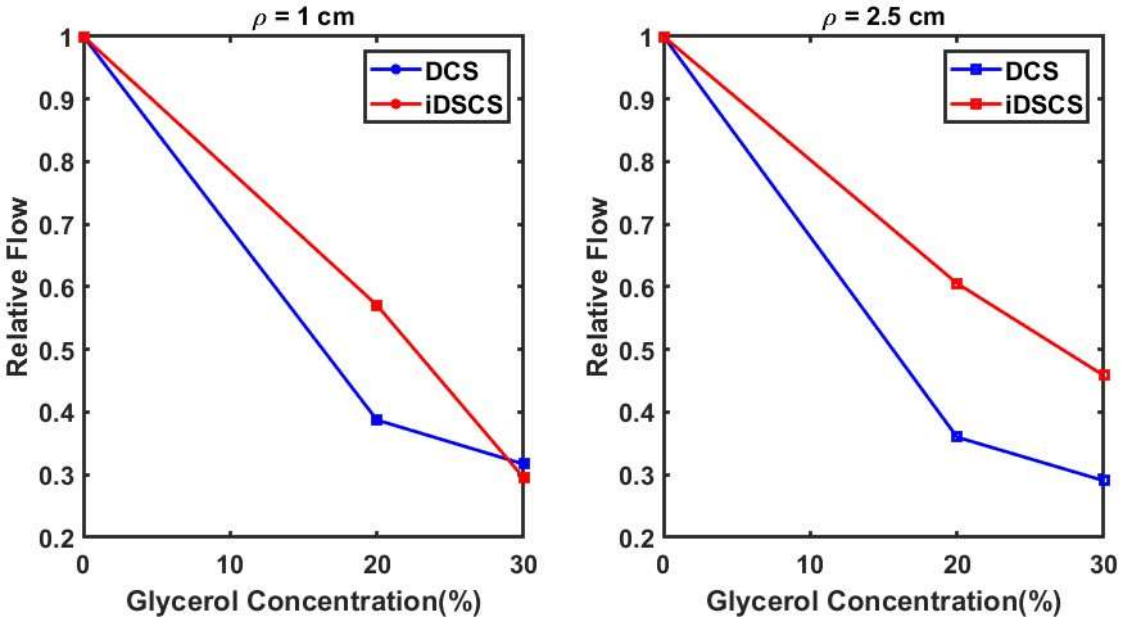

Figure 5.11 In the panel the relative flow is shown as a function of glycerol concentration (%) at wavelength 785 nm measured with iDSCS (red) and DCS (blue). Flow decreased with increasing glycerol concentration from left to right. The sensitivity of iDSCS compare well with DCS at SD of 1 cm (left). However, sensitivity of iDSCS at 2.5 cm (right) reduces compared to DCS.

Intralipid (20% emulsion, Sigma-Aldrich, MO) and glycerol (≥ 99.5%, Sigma-Aldrich Co., USA). The intralipid was used as a scattering element whereas different concentration of glycerol was used to change the viscosity of the phantoms, thus changing the diffusion coefficient of scatterers. Three different phantoms were prepared with 0%, 20% and 30% glycerol with 0.75%, 0.89% and 1.3% intralipid concentrations respectively. The amount of intralipid in phantoms for each glycerol concentration was varied to hold the scattering coefficient of the phantoms constant following prior literature [95].

In these experiments I measured 'flow' in these phantoms with both DCS and iDSCS synchronously for all three phantoms, using the probe/experimental procedure described in the previous section. DCS data acquisition was performed at an effective rate of 10 Hz whereas for iDSCS the acquisition rate was 33 Hz. For each phantom 1 minute of data was acquired, DCS autocorrelation functions or iDSCS speckle visibility curves were averaged, and the data were fit to respective models to obtain a blood flow index. Figure 5.11 displays the change in flow index due to addition of glycerol to the phantom, relative to the flow index at 0% glycerol (left/right, for source detector separation of 1 cm/2.5 cm respectively). In both curves, data acquired with DCS is shown in blue, while those measured with iDSCS is shown in red. In all cases (both techniques, both source detector separations), the flow index decreases with glycerol concentration. At 1 cm (Figure 5.11 left) the change in flow index measured with iDSCS is comparable to DCS, while at at 2.5 cm (Figure 5.11 right) the sensitivity of the iDSCS is lower than that of DCS. . The decrease in sensitivity at higher SD separation can be attributed to reduced SNR at low intensities caused by dynamic electrical noise affecting measured variance. An effective technique to correct dynamic electrical noise in the acquisition circuit could help improve the sensitivity at higher SD

separation. We also note that the sensitivity if iDSCS is compared to DCS and the true change in 'flow' is unknown.

5.5 Discussion

In this contribution, I have developed and implemented integrated Diffuse Speckle Contrast Spectroscopy, a photodiode-based method for deep tissue blood flow measurement. iDSCS combines the instrumental simplicity of Laser Speckle Contrast Imaging, with mathematical models from Diffuse Correlation Spectroscopy, to yield a small, wearable detector for deep-tissue blood flow measurements. The iDSCS sensor is realized using an off-the-shelf photodiode and a custom electronic integrator, all controlled with signals from a standard data acquisition device. By operating the photodiode in a photo-voltaic (unbiased) mode, iDSCS achieves the lowest dark noise. Further, with no electronics associated with CCD/CMOS charge transfers, iDSCS has negligible readout noise. These noises are lowest in the class of diffuse speckle contrast instruments, especially when compared to SPAD arrays or CMOS cameras. Nevertheless, several challenges need to be overcome to practically implement the sensor. Most significantly, the sensitivity of iDSCS instrument is affected by speckle averaging effect, i.e., the large detector area of the photodiode averages multiple detected speckles, thus reducing the effective dynamic range of the signal that could be recorded. While the detrimental effects of speckle averaging could be avoided by reducing the photosensitive area, I developed an active current-negation circuit to reduce/eliminate the average photodiode current due to speckle averaging. This ensures that the iDSCS sensor integrates and detects primarily the fluctuating dynamic speckle intensities. The efficacy of this current subtraction approach was validated in experiments on tissue simulating phantoms; notably the current subtraction provides speckle variance measurements three orders of magnitude higher than conventional iDSCS.

In representative *in vivo* experiments on the human forearm, I compared the performance of the iDSCS sensor with a conventional fiber based DCS instrument. In an in-*vivo* arm cuff occlusion experiment, iDSCS recorded a nearly 80% reduction in blood flow, marginally higher than the 100% reduction in blood flow measured with DCS. iDSCS is also able to resolve blood flow pulsatility in the human arm, although the fidelity of the waveform is not as robust as DCS. iDSCS compares favorably with DCS in measuring tissue perfusion. The iDSCS method is sensitive to flow changes *in-vivo* for both 1 cm and 2.5 cm source detector separation, with results comparable to DCS.

While iDSCS has low dark, shot and readout noises, dynamic electrical noise generated by circuit components (i.e., power supply, parasitic capacitance etc.) could affect the detected speckle variance. In the instrument presented here, this electronic noise is not accounted for – which is a possible explanation for the reduction in sensitivity of the iDSCS measurements to blood flow changes. At lower SD separation (i.e., 1 cm) the signal intensity detected $I(t)$ is higher thus relativity unaffected by dynamic electrical noise, however at higher SD separation due to low intensity detected the dynamic electrical noise compromises measurement sensitivity. An effective correction for this dynamic electrical noise is necessary to improve the sensitivity and dynamic range of blood flow estimates with iDSCS.

I conclude by mentioning some advantages of the iDSCS sensor. First, due to its small footprint, the iDSCS sensor can be readily incorporated within an wearable probe for fiber-less detection of blood flow. Second, the iDSCS sensor permits single-shot measurement of speckle variance at multiple exposure times, which is an advantage over similar camera-based devices. Third, the unbiased operation of the photodiode and dark current measurements provides for real-time noise correction. Finally, the sensor's low power/bandwidth requirements permit embedded

measurements with microcontrollers. These significant advantages could permit wearable deep tissue blood flow measurements with DCS.

Chapter 6: Conclusion and Future Work

In this dissertation, I have presented and validated three technological innovations to reduce the instrumentation burden for wide adoption of deep tissue blood flow measurements with Diffuse Correlation Spectroscopy (DCS).

In chapter 3, I have introduced compressed DCS (CDCS), a hardware data compression technique for DCS. In traditional fast DCS instruments, 32-bit counters are used to sample and count TTL pulses generated by the single photon counting detectors; this limits the number of channels in any given DCS instrument to 16. To achieve simple multi-channel operation, I leveraged the fact that the number of photon-counts per sample/channel in DCS range between 1-4. Since this number can be easily represented by readily available binary coded counter, I realized a hardware compressed DCS instrument with chained BCD-based TTL pulse counting circuit for multi-channel DCS acquisition. I validated the efficacy of the embedded system against traditional hardware counters used in a typical DCS instrument. In solid phantom, liquid phantom and *in-vivo* studies the CDCS system showed excellent agreement with embedded 32-bit counters of NI-DAQ used for fast DCS measurement[47]. I further characterized the system noise as a function of delay time τ and intensity I to provide an operation standard for this technique. Overall, this system achieved an 87.5% data compression efficiency for DCS counting operation.

In Chapter 4, I developed fiberless DCS, a compact low power laser system for DCS blood flow measurements. One of the major components in typical diffusion and speckle-based measurements is a high bandwidth laser source. Although the actual coherence requirement of these technologies for probing deep inside the tissue (~2.5 cm) is few hundred centimeters, most

instruments currently use light sources with around 50 m coherence length. Since these highly stabilized sources also require power intensive circuitry for cooling and bandwidth overhead for fiber collimation, they are in general bulky and expensive. In chapter 4, I highlight the minimum coherence requirement of a laser source for these diffuse dynamic speckle measurements. Considering these requirements, I developed a custom miniature laser source using just a single mode diode laser, and 3D printed assembly for collimation and electrical/thermal isolation. I characterized the coherence length of this FBDCSS laser system to be ~50 cm. In tissue simulating phantoms and *in vivo* experiments, the FBDCS source met the benchmarks set by conventional wavelength stabilized DCS sources in terms of accuracy in detecting blood flow, sensitivity and dynamic range of flow changes, and SNR.

Finally in chapter 5, I introduced integrated Diffuse Speckle Contrast Spectroscopy (iDSCS), a novel deep tissue hemodynamics measurement technique. Here, I leveraged the simplicity of the LSCI instrumentation in combination with multi-scattering principles of Diffuse Correlation Spectroscopy to realize a small, low power instrument capable of probing deep in the tissue for localized microvasculature flow. iDSCS is built using a single off-the-shelf photodiode in unbiased configuration, with good sensitivity to low light conditions and with intrinsically reduced dark current. Meager power consumption and small form factor of this device makes it suitable for portable and wearable operation. In preliminary in-vivo arm cuff occlusion study, the iDSCS sensor performs comparably to DCS, although its sensitivity and dynamic range can be improved with better characterization of the system electronic noise.

6.1 Future Work

A successful demonstration of deep tissue blood flow sensitivity is achieved with a simple instrumentation of iDSCS, which is a significant improvement over existing technology, paving

the road for a wearable deep-tissue blood flow monitor. In combination, the iDSCS, FBDCS and CDCS techniques introduced in this dissertation should improve the adoptability and affordability of DCS instruments. Critically, FBDCS and iDSCS can be combined to create the world's first fully wearable deep tissue blood flow monitor. Such a realized prototype should be capable of experimental work outside laboratory setting and permit in real-time clinical functional monitoring of disease stated.

I hereby note some imminent technical challenges need to be addressed for reliable continuous operation of the iDSCS method. The sensitivity of the iDSCS needs to be characterized in liquid phantom. This is particularly hard to achieve because prototyping water-resistant probe containing sensitive electronics to drive the system is technically challenging. However, a 1:1 comparison with DCS technique would provide better direction toward improving the SNR of the device.. Moreover, a combined circuit system consisting of an FBDCS compact laser and iDSCS sensor could be developed for portable wearable use. I believe these improvements would lead to a new avenue in optical based hemodynamics and associated biomedical research.

References

[1] N. A. Lassen and M. S. Christensen, “Physiology of Cerebral Blood Flow.”

[2] N. A. Lassen, D. H. Ingvar, and E. Skinhøj, “Brain Function and Blood Flow,” *Scientific American*, vol. 239, no. 4, pp. 62–71, 1978.

[3] S. Strandgaard and O. B. Paulson, “Regulation of Cerebral Blood Flow in Health and Disease,” *Journal of Cardiovascular Pharmacology*, vol. 19, p. S89, 1992.

[4] G. Bouma and J. Muizelaar, “Cerebral blood flow, cerebral blood volume, and cerebrovascular reactivity after severe head injury,” *Journal of neurotrauma*, vol. 9 Suppl 1, pp. S333-48, Apr. 1992.

[5] F. E. Gump, J. J B Price, and J. M. Kinney, “Whole body and splanchnic blood flow and oxygen consumption measurements in patients with intraperitoneal infection.,” *Annals of Surgery*, vol. 171, no. 3, p. 321, Mar. 1970, doi: 10.1097/00000658-197003000-00001.

[6] R. M. Bryan, L. Cherian, and C. Robertson, “Regional Cerebral Blood Flow After Controlled Cortical Impact Injury in Rats,” *Anesthesia & Analgesia*, vol. 80, no. 4, pp. 687–695, Apr. 1995.

[7] T.-Y. Xu *et al.*, “Blood Flow Pattern in the Middle Cerebral Artery in Relation to Indices of Arterial Stiffness in the Systemic Circulation,” *American Journal of Hypertension*, vol. 25, no. 3, pp. 319–324, Mar. 2012, doi: 10.1038/ajh.2011.223.

[8] B. Andresen *et al.*, “Cerebral oxygenation and blood flow in normal term infants at rest measured by a hybrid near-infrared device (BabyLux),” *Pediatric Research*, p. 1, Jun. 2019, doi: 10.1038/s41390-019-0474-9.

[9] E. C. Peterson, Z. Wang, and G. Britz, “Regulation of Cerebral Blood Flow,” *International Journal of Vascular Medicine*, vol. 2011, p. e823525, Jul. 2011, doi: 10.1155/2011/823525.

[10] U. Quinn, L. A. Tomlinson, and J. R. Cockcroft, “Arterial stiffness,” *JRSM Cardiovascular Disease*, vol. 1, no. 6, pp. 1–8, Sep. 2012, doi: 10.1258/cvd.2012.012024.

[11] M. E. Safar and P. Laurent, “Pulse pressure and arterial stiffness in rats: comparison with humans,” *American Journal of Physiology-Heart and Circulatory Physiology*, vol. 285, no. 4, pp. H1363–H1369, Oct. 2003, doi: 10.1152/ajpheart.00513.2003.

[12] A.-C. Ehlis, S. Schneider, T. Dresler, and A. J. Fallgatter, “Application of functional near-infrared spectroscopy in psychiatry,” *NeuroImage*, vol. 85, pp. 478–488, Jan. 2014, doi: 10.1016/j.neuroimage.2013.03.067.

[13] P. F. Liddle, K. J. Friston, C. D. Frith, S. R. Hirsch, T. Jones, and R. S. J. Frackowiak, "Patterns of Cerebral Blood Flow in Schizophrenia," *The British Journal of Psychiatry*, vol. 160, no. 2, pp. 179–186, Feb. 1992, doi: 10.1192/bjp.160.2.179.

[14] P. Le Roux, "Physiological monitoring of the severe traumatic brain injury patient in the intensive care unit," *Curr Neurol Neurosci Rep*, vol. 13, no. 3, p. 331, Mar. 2013, doi: 10.1007/s11910-012-0331-2.

[15] "Multimodal Monitoring in Subarachnoid Hemorrhage." https://www.ahajournals.org/doi/epub/10.1161/STROKEAHA.111.639906 (accessed Oct. 15, 2022).

[16] M. Oddo, F. Villa, and G. Citerio, "Brain multimodality monitoring: an update," *Curr Opin Crit Care*, vol. 18, no. 2, pp. 111–118, Apr. 2012, doi: 10.1097/MCC.0b013e32835132a5.

[17] S. Sinha, E. Hudgins, J. Schuster, and R. Balu, "Unraveling the complexities of invasive multimodality neuromonitoring," *Neurosurg Focus*, vol. 43, no. 5, p. E4, Nov. 2017, doi: 10.3171/2017.8.FOCUS17449.

[18] J. M. Perlman, "White matter injury in the preterm infant: an important determination of abnormal neurodevelopment outcome," *Early Hum Dev*, vol. 53, no. 2, pp. 99–120, Dec. 1998, doi: 10.1016/s0378-3782(98)00037-1.

[19] A. J. du Plessis and J. J. Volpe, "Perinatal brain injury in the preterm and term newborn," *Curr Opin Neurol*, vol. 15, no. 2, pp. 151–157, Apr. 2002, doi: 10.1097/00019052-200204000-00005.

[20] A. K. Dunn, H. Bolay, M. A. Moskowitz, and D. A. Boas, "Dynamic Imaging of Cerebral Blood Flow Using Laser Speckle," *Journal of Cerebral Blood Flow & Metabolism*, vol. 21, no. 3, pp. 195–201, Mar. 2001, doi: 10.1097/00004647-200103000-00002.

[21] A. B. Parthasarathy, "Quantitative cerebral blood flow measurement with Multi Exposure Speckle Imaging," thesis, 2010. Accessed: Feb. 14, 2019. [Online]. Available: https://repositories.lib.utexas.edu/handle/2152/ETD-UT-2010-05-996

[22] A. H. Van and H. J. Van, "Influence of anesthesia on cerebral blood flow and cerebral metabolism: an overview," *Agressologie*, vol. 32, no. 6–7, pp. 303–306, Jan. 1991.

[23] H. K. Shin *et al.*, "Normobaric hyperoxia improves cerebral blood flow and oxygenation, and inhibits peri-infarct depolarizations in experimental focal ischaemia," *Brain*, vol. 130, no. Pt 6, pp. 1631–1642, Jun. 2007, doi: 10.1093/brain/awm071.

[24] S. Ogawa, T. M. Lee, A. R. Kay, and D. W. Tank, "Brain magnetic resonance imaging with contrast dependent on blood oxygenation," *PNAS*, vol. 87, no. 24, pp. 9868–9872, Dec. 1990, doi: 10.1073/pnas.87.24.9868.

[25] L. Axel, “Cerebral blood flow determination by rapid-sequence computed tomography: theoretical analysis.,” *Radiology*, Dec. 1980, doi: 10.1148/radiology.137.3.7003648.

[26] C. C. Bishop, S. Powell, D. Rutt, and N. L. Browse, “Transcranial Doppler measurement of middle cerebral artery blood flow velocity: a validation study.,” *Stroke*, vol. 17, no. 5, pp. 913–915, Sep. 1986, doi: 10.1161/01.STR.17.5.913.

[27] T. Durduran and A. G. Yodh, “Diffuse correlation spectroscopy for non-invasive, micro-vascular cerebral blood flow measurement,” *NeuroImage*, vol. 85, pp. 51–63, Jan. 2014, doi: 10.1016/j.neuroimage.2013.06.017.

[28] E. M. Buckley *et al.*, “Cerebral hemodynamics in preterm infants during positional intervention measured with diffuse correlation spectroscopy and transcranial Doppler ultrasound,” *Opt. Express, OE*, vol. 17, no. 15, pp. 12571–12581, Jul. 2009, doi: 10.1364/OE.17.012571.

[29] M. N. Kim *et al.*, “Noninvasive Measurement of Cerebral Blood Flow and Blood Oxygenation Using Near-Infrared and Diffuse Correlation Spectroscopies in Critically Brain-Injured Adults,” *Neurocritical Care*, vol. 12, no. 2, pp. 173–180, Apr. 2010, doi: 10.1007/s12028-009-9305-x.

[30] V. Jain *et al.*, “Cerebral Oxygen Metabolism in Neonates with Congenital Heart Disease Quantified by MRI and Optics,” *Journal of Cerebral Blood Flow & Metabolism*, vol. 34, no. 3, pp. 380–388, Mar. 2014, doi: 10.1038/jcbfm.2013.214.

[31] E. M. Buckley *et al.*, “Early postoperative changes in cerebral oxygen metabolism following neonatal cardiac surgery: Effects of surgical duration,” *The Journal of Thoracic and Cardiovascular Surgery*, vol. 145, no. 1, pp. 196-205.e1, Jan. 2013, doi: 10.1016/j.jtcvs.2012.09.057.

[32] C. G. Favilla *et al.*, “Optical Bedside Monitoring of Cerebral Blood Flow in Acute Ischemic Stroke Patients during Head of Bed Manipulation,” *Stroke*, vol. 45, no. 5, pp. 1269–1274, May 2014, doi: 10.1161/STROKEAHA.113.004116.

[33] M. T. Mullen *et al.*, “Cerebral Blood Flow Response During Bolus Normal Saline Infusion After Ischemic Stroke,” *J Stroke Cerebrovasc Dis*, vol. 28, no. 11, p. 104294, Nov. 2019, doi: 10.1016/j.jstrokecerebrovasdis.2019.07.010.

[34] G. Yu *et al.*, “Time-dependent blood flow and oxygenation in human skeletal muscles measured with noninvasive near-infrared diffuse optical spectroscopies,” *JBO*, vol. 10, no. 2, p. 024027, Mar. 2005, doi: 10.1117/1.1884603.

[35] G. Yu *et al.*, “Validation of diffuse correlation spectroscopy for muscle blood flow with concurrent arterial spin labeled perfusion MRI,” *Opt. Express, OE*, vol. 15, no. 3, pp. 1064–1075, Feb. 2007, doi: 10.1364/OE.15.001064.

[36] A. S. Kogler *et al.*, “Fiber-optic Monitoring of Spinal Cord Hemodynamics in Experimental Aortic Occlusion,” *Anesthesiology*, vol. 123, no. 6, pp. 1362–1373, Dec. 2015, doi: 10.1097/ALN.0000000000000883.

[37] R. C. Mesquita *et al.*, “Optical Monitoring and Detection of Spinal Cord Ischemia,” *PLoS ONE*, vol. 8, no. 12, p. e83370, Dec. 2013, doi: 10.1371/journal.pone.0083370.

[38] D. R. Busch *et al.*, “Towards rapid intraoperative axial localization of spinal cord ischemia with epidural diffuse correlation monitoring,” *PLoS One*, vol. 16, no. 5, p. e0251271, 2021, doi: 10.1371/journal.pone.0251271.

[39] D. A. Boas and A. K. Dunn, “Laser speckle contrast imaging in biomedical optics,” *JBO, JBOPFO*, vol. 15, no. 1, p. 011109, Jan. 2010, doi: 10.1117/1.3285504.

[40] R. Bi, J. Dong, and K. Lee, “Deep tissue flowmetry based on diffuse speckle contrast analysis,” *Opt. Lett., OL*, vol. 38, no. 9, pp. 1401–1403, May 2013, doi: 10.1364/OL.38.001401.

[41] C. P. Valdes, H. M. Varma, A. K. Kristoffersen, T. Dragojevic, J. P. Culver, and T. Durduran, “Speckle contrast optical spectroscopy, a non-invasive, diffuse optical method for measuring microvascular blood flow in tissue,” *Biomed. Opt. Express, BOE*, vol. 5, no. 8, pp. 2769–2784, Aug. 2014, doi: 10.1364/BOE.5.002769.

[42] T. Dragojević *et al.*, “Compact, multi-exposure speckle contrast optical spectroscopy (SCOS) device for measuring deep tissue blood flow,” *Biomed. Opt. Express, BOE*, vol. 9, no. 1, pp. 322–334, Jan. 2018, doi: 10.1364/BOE.9.000322.

[43] D. J. Pine, D. A. Weitz, J. X. Zhu, and E. Herbolzheimer, “Diffusing-wave spectroscopy: dynamic light scattering in the multiple scattering limit,” *Journal de Physique*, vol. 51, no. 18, pp. 2101–2127, 1990, doi: 10.1051/jphys:0199000510180210100.

[44] K. Murari, N. Li, A. Rege, X. Jia, A. All, and N. Thakor, “Contrast-enhanced imaging of cerebral vasculature with laser speckle,” *Appl Opt*, vol. 46, no. 22, pp. 5340–5346, Aug. 2007, doi: 10.1364/ao.46.005340.

[45] C. Ayata, A. K. Dunn, Y. Gursoy-OZdemir, Z. Huang, D. A. Boas, and M. A. Moskowitz, “Laser speckle flowmetry for the study of cerebrovascular physiology in normal and ischemic mouse cortex,” *J Cereb Blood Flow Metab*, vol. 24, no. 7, pp. 744–755, Jul. 2004, doi: 10.1097/01.WCB.0000122745.72175.D5.

[46] R. Bandyopadhyay, A. S. Gittings, S. S. Suh, P. K. Dixon, and D. J. Durian, “Speckle-visibility spectroscopy: A tool to study time-varying dynamics,” *Review of Scientific Instruments*, vol. 76, no. 9, p. 093110, Sep. 2005, doi: 10.1063/1.2037987.

[47] D. Wang *et al.*, “Fast blood flow monitoring in deep tissues with real-time software correlators,” *Biomed. Opt. Express, BOE*, vol. 7, no. 3, pp. 776–797, Mar. 2016, doi: 10.1364/BOE.7.000776.

[48] C. Cheung, J. P. Culver, K. Takahashi, J. H. Greenberg, and A. G. Yodh, "In vivocerebrovascular measurement combining diffuse near-infrared absorption and correlation spectroscopies," *Phys. Med. Biol.*, vol. 46, no. 8, pp. 2053–2065, Jul. 2001, doi: 10.1088/0031-9155/46/8/302.

[49] M. D. Stern, "In vivo evaluation of microcirculation by coherent light scattering," *Nature*, vol. 254, no. 5495, p. 56, Mar. 1975, doi: 10.1038/254056a0.

[50] D. Magatti and F. Ferri, "Fast multi-tau real-time software correlator for dynamic light scattering," *Applied Optics*, vol. 40, no. 24, p. 4011, Aug. 2001, doi: 10.1364/AO.40.004011.

[51] A. Biswas and A. B. Parthasarathy, "Fast Diffuse Correlation Spectroscopy with a low-cost, fiberless embedded diode laser," in *Biophotonics Congress: Biomedical Optics 2020 (Translational, Microscopy, OCT, OTS, BRAIN)*, Washington, DC, 2020, p. JW3A.7. doi: 10.1364/TRANSLATIONAL.2020.JW3A.7.

[52] T. Durduran, R. Choe, W. B. Baker, and A. G. Yodh, "Diffuse optics for tissue monitoring and tomography," *Reports on Progress in Physics*, vol. 73, no. 7, p. 076701, Jul. 2010, doi: 10.1088/0034-4885/73/7/076701.

[53] P.-A. Lemieux and D. J. Durian, "Investigating non-Gaussian scattering processes by using nth -order intensity correlation functions," *Journal of the Optical Society of America A*, vol. 16, no. 7, p. 1651, Jul. 1999, doi: 10.1364/JOSAA.16.001651.

[54] G. Yu *et al.*, "Noninvasive Monitoring of Murine Tumor Blood Flow During and After Photodynamic Therapy Provides Early Assessment of Therapeutic Efficacy," *Clin Cancer Res*, vol. 11, no. 9, pp. 3543–3552, May 2005, doi: 10.1158/1078-0432.CCR-04-2582.

[55] S. Han *et al.*, "Non-contact scanning diffuse correlation tomography system for three-dimensional blood flow imaging in a murine bone graft model," *Biomed. Opt. Express, BOE*, vol. 6, no. 7, pp. 2695–2712, Jul. 2015, doi: 10.1364/BOE.6.002695.

[56] A. B. Parthasarathy, W. J. Tom, A. Gopal, X. Zhang, and A. K. Dunn, "Robust flow measurement with multi-exposure speckle imaging," *Opt. Express, OE*, vol. 16, no. 3, pp. 1975–1989, Feb. 2008, doi: 10.1364/OE.16.001975.

[57] T. G. Shaw, K. F. Mortel, J. S. Meyer, R. L. Rogers, J. Hardenberg, and M. M. Cutaia, "Cerebral blood flow changes in benign aging and cerebrovascular disease," *Neurology*, vol. 34, no. 7, pp. 855–855, Jul. 1984, doi: 10.1212/WNL.34.7.855.

[58] D. J. Duncker, A. Koller, D. Merkus, and J. M. Canty, "Regulation of Coronary Blood Flow in Health and Ischemic Heart Disease," *Progress in Cardiovascular Diseases*, vol. 57, no. 5, pp. 409–422, Mar. 2015, doi: 10.1016/j.pcad.2014.12.002.

[59] C. J. Pournaras, E. Rungger-Brändle, C. E. Riva, S. H. Hardarson, and E. Stefansson, "Regulation of retinal blood flow in health and disease," *Progress in Retinal and Eye Research*, vol. 27, no. 3, pp. 284–330, May 2008, doi: 10.1016/j.preteyeres.2008.02.002.

[60] D. A. Boas and A. G. Yodh, "Spatially varying dynamical properties of turbid media probed with diffusing temporal light correlation," *Journal of the Optical Society of America A*, vol. 14, no. 1, p. 192, Jan. 1997, doi: 10.1364/JOSAA.14.000192.

[61] E. M. Buckley, A. B. Parthasarathy, P. E. Grant, A. G. Yodh, and M. A. Franceschini, "Diffuse correlation spectroscopy for measurement of cerebral blood flow: future prospects," *Neurophotonics*, vol. 1, no. 1, p. 011009, Jun. 2014, doi: 10.1117/1.NPh.1.1.011009.

[62] S. A. Carp, P. Farzam, N. Redes, D. M. Hueber, and M. A. Franceschini, "Combined multi-distance frequency domain and diffuse correlation spectroscopy system with simultaneous data acquisition and real-time analysis," *Biomed. Opt. Express*, vol. 8, no. 9, p. 3993, Sep. 2017, doi: 10.1364/BOE.8.003993.

[63] D. Tamborini, P. Farzam, B. B. Zimmermann, K.-C. Wu, D. A. Boas, and M. A. Franceschini, "Development and characterization of a multidistance and multiwavelength diffuse correlation spectroscopy system," *NPh*, vol. 5, no. 1, p. 011015, Sep. 2017, doi: 10.1117/1.NPh.5.1.011015.

[64] W. Lin, D. R. Busch, C. C. Goh, J. Barsi, and T. F. Floyd, "Diffuse Correlation Spectroscopy Analysis Implemented on a Field Programmable Gate Array," *IEEE Access*, vol. 7, pp. 122503–122512, 2019, doi: 10.1109/ACCESS.2019.2938085.

[65] A. B. Parthasarathy *et al.*, "Dynamic autoregulation of cerebral blood flow measured non-invasively with fast diffuse correlation spectroscopy," *J Cereb Blood Flow Metab*, vol. 38, no. 2, pp. 230–240, Feb. 2018, doi: 10.1177/0271678X17747833.

[66] D. R. Busch *et al.*, "Noninvasive optical measurement of microvascular cerebral hemodynamics and autoregulation in the neonatal ECMO patient," *Pediatr Res*, vol. 88, no. 6, pp. 925–933, Dec. 2020, doi: 10.1038/s41390-020-0841-6.

[67] J. Selb *et al.*, "Prolonged monitoring of cerebral blood flow and autoregulation with diffuse correlation spectroscopy in neurocritical care patients," *Neurophotonics*, vol. 5, no. 4, p. 045005, Oct. 2018, doi: 10.1117/1.NPh.5.4.045005.

[68] W. B. Baker *et al.*, "Noninvasive optical monitoring of critical closing pressure and arteriole compliance in human subjects," *J Cereb Blood Flow Metab*, vol. 37, no. 8, pp. 2691–2705, Aug. 2017, doi: 10.1177/0271678X17709166.

[69] J. Yang, A. Ruesch, J. M. Kainerstorfer, and J. M. Kainerstorfer, "Optical Methods for Non-Invasive Assessment of Arteriole Flow Impedance," in *Biophotonics Congress: Biomedical Optics 2020 (Translational, Microscopy, OCT, OTS, BRAIN) (2020), paper SW2D.5*, Apr. 2020, p. SW2D.5. doi: 10.1364/OTS.2020.SW2D.5.

[70] C. Zhou, G. Yu, D. Furuya, J. H. Greenberg, A. G. Yodh, and T. Durduran, "Diffuse optical correlation tomography of cerebral blood flow during cortical spreading depression in rat brain," *Optics Express*, vol. 14, no. 3, p. 1125, Feb. 2006, doi: 10.1364/OE.14.001125.

[71] J. P. Culver, T. Durduran, D. Furuya, C. Cheung, J. H. Greenberg, and A. G. Yodh, "Diffuse optical tomography of cerebral blood flow, oxygenation, and metabolism in rat during focal ischemia," *J Cereb Blood Flow Metab*, vol. 23, no. 8, pp. 911–924, Aug. 2003, doi: 10.1097/01.WCB.0000076703.71231.BB.

[72] M. Pagliazzi *et al.*, "Time domain diffuse correlation spectroscopy with a high coherence pulsed source: in vivo and phantom results," *Biomedical Optics Express*, vol. 8, no. 11, p. 5311, Nov. 2017, doi: 10.1364/BOE.8.005311.

[73] A. Biswas, S. Moka, A. Muller, and A. B. Parthasarathy, "Fast diffuse correlation spectroscopy with a low-cost, fiber-less embedded diode laser," *Biomed. Opt. Express*, vol. 12, no. 11, p. 6686, Nov. 2021, doi: 10.1364/BOE.435136.

[74] "ANSI Z136.1 - Safe Use of Lasers," *The Laser Institute*, Aug. 11, 2017. https://www.lia.org/resources/laser-safety-information/laser-safety-standards/ansi-z136-standards/z136-1 (accessed Oct. 15, 2022).

[75] J. Dong, R. Bi, J. H. Ho, P. S. P. Thong, K.-C. Soo, and K. Lee, "Diffuse correlation spectroscopy with a fast Fourier transform-based software autocorrelator," *J. Biomed. Opt*, vol. 17, no. 9, p. 0970041, Sep. 2012, doi: 10.1117/1.JBO.17.9.097004.

[76] M. Tivnan, R. Gurjar, D. Wolf, and K. Vishwanath, "High Frequency Sampling of TTL Pulses on a Raspberry Pi for Diffuse Correlation Spectroscopy Applications," *Sensors*, vol. 15, no. 8, pp. 19709–19722, Aug. 2015, doi: 10.3390/s150819709.

[77] A. Biswas, D. Buffone, S. Shivanna, and A. B. Parthasarathy, "Fast Diffuse Correlation Spectroscopy with Low-Cost Microcontroller," p. 1.

[78] A. Biswas, D. A. Buffone, and A. B. Parthasarathy, "Fast Diffuse Correlation Spectroscopy with Low-Cost Microcontroller," in *Biophotonics Congress: Biomedical Optics Congress 2018 (Microscopy/Translational/Brain/OTS)*, Hollywood, Florida, 2018, p. JW3A.20. doi: 10.1364/TRANSLATIONAL.2018.JW3A.20.

[79] C. Huang *et al.*, "Low-cost compact diffuse speckle contrast flowmeter using small laser diode and bare charge-coupled-device," *J Biomed Opt*, vol. 21, no. 8, Aug. 2016, doi: 10.1117/1.JBO.21.8.080501.

[80] J. Liu, H. Zhang, J. Lu, X. Ni, and Z. Shen, "Quantitative model of diffuse speckle contrast analysis for flow measurement," *JBO*, vol. 22, no. 7, p. 076016, Jul. 2017, doi: 10.1117/1.JBO.22.7.076016.

[81] A. Biswas and A. B. Parthasarathy, "Fast, compact measurement of deep tissue blood flow with integrated diffuse correlation spectroscopy," in *Biomedical Applications of Light Scattering X*, San Francisco, United States, Feb. 2020, p. 32. doi: 10.1117/12.2546581.

[82] A. Biswas and A. B. Parthasarathy, “An integrated detection scheme for fast, embedded measurement of deep tissue blood flow with Diffuse Correlation Spectroscopy,” in *Biophotonics Congress: Biomedical Optics 2020 (Translational, Microscopy, OCT, OTS, BRAIN) (2020), paper SM3D.5*, Apr. 2020, p. SM3D.5. doi: 10.1364/OTS.2020.SM3D.5.

[83] N. A. Lassen and M. S. Christensen, “Physiology of cerebral blood flow,” *Br J Anaesth*, vol. 48, no. 8, pp. 719–734, Aug. 1976, doi: 10.1093/bja/48.8.719.

[84] M. P. V. Albada and A. Lagendijk, “Observation of Weak Localization of Light in a Random Medium,” *Physical Review Letters*, vol. 55, no. 24, pp. 2692–2695, Dec. 1985, doi: 10.1103/PhysRevLett.55.2692.

[85] P. N. Pusey, J. M. Vaughan, and D. V. Willetts, “Effect of spatial incoherence of the laser in photon-correlation spectroscopy,” *Journal of the Optical Society of America*, vol. 73, no. 8, p. 1012, Aug. 1983, doi: 10.1364/JOSA.73.001012.

[86] M. Hiraoka *et al.*, “A Monte Carlo investigation of optical pathlength in inhomogeneous tissue and its application to near-infrared spectroscopy,” *Phys. Med. Biol.*, vol. 38, no. 12, pp. 1859–1876, Dec. 1993, doi: 10.1088/0031-9155/38/12/011.

[87] H. Dehghani *et al.*, “Near infrared optical tomography using NIRFAST: Algorithm for numerical model and image reconstruction,” *Communications in Numerical Methods in Engineering*, vol. 25, no. 6, pp. 711–732, 2009, doi: https://doi.org/10.1002/cnm.1162.

[88] D. T. Delpy, M. Cope, P. van der Zee, S. Arridge, S. Wray, and J. Wyatt, “Estimation of optical pathlength through tissue from direct time of flight measurement,” *Phys. Med. Biol.*, vol. 33, no. 12, pp. 1433–1442, Dec. 1988, doi: 10.1088/0031-9155/33/12/008.

[89] S. R. Arridge, M. Cope, and D. T. Delpy, “The theoretical basis for the determination of optical pathlengths in tissue: temporal and frequency analysis,” *Phys. Med. Biol.*, vol. 37, no. 7, pp. 1531–1560, Jul. 1992, doi: 10.1088/0031-9155/37/7/005.

[90] S. A. Carp *et al.*, “Diffuse correlation spectroscopy measurements of blood flow using 1064 nm light,” *JBO*, vol. 25, no. 9, p. 097003, Sep. 2020, doi: 10.1117/1.JBO.25.9.097003.

[91] N. Balakrishnan and V. B. Nevzorov, “A Primer On Statistical Distributions,” p. 323.

[92] W. B. Baker *et al.*, “Pressure modulation algorithm to separate cerebral hemodynamic signals from extracerebral artifacts,” *NPh, NEUROW*, vol. 2, no. 3, p. 035004, Aug. 2015, doi: 10.1117/1.NPh.2.3.035004.

[93] Z. Li *et al.*, “Calibration of diffuse correlation spectroscopy blood flow index with venous-occlusion diffuse optical spectroscopy in skeletal muscle,” *JBO, JBOPFO*, vol. 20, no. 12, p. 125005, Dec. 2015, doi: 10.1117/1.JBO.20.12.125005.

[94] K. Lee, “Diffuse Speckle Contrast Analysis (DSCA) for Deep Tissue Blood Flow Monitoring,” *Advanced Biomedical Engineering*, vol. 9, no. 0, pp. 21–30, 2020, doi: 10.14326/abe.9.21.

[95] L. Cortese *et al.*, “Liquid phantoms for near-infrared and diffuse correlation spectroscopies with tunable optical and dynamic properties,” *Biomed. Opt. Express*, vol. 9, no. 5, p. 2068, May 2018, doi: 10.1364/BOE.9.002068.

Appendix A: Copyright Permissions

The permission below is for the use of image in Figure 2.4.

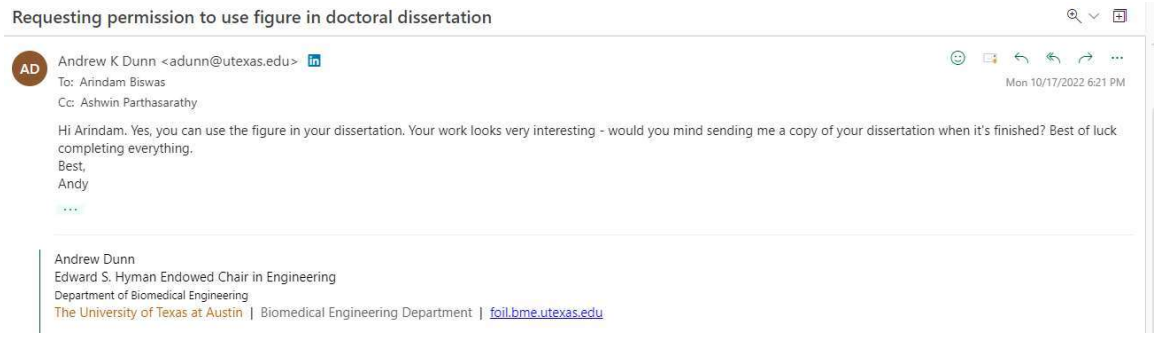

Requesting permission to use figure in doctoral dissertation

AD Andrew K Dunn <adunn@utexas.edu>

To: Arindam Biswas

Cc: Ashwin Parthasarathy

Mon 10/17/2022 6:21 PM

Hi Arindam. Yes, you can use the figure in your dissertation. Your work looks very interesting - would you mind sending me a copy of your dissertation when it's finished? Best of luck completing everything.

Best,

Andy

...

Andrew Dunn

Edward S. Hyman Endowed Chair in Engineering

Department of Biomedical Engineering

The University of Texas at Austin | Biomedical Engineering Department | foil.bme.utexas.edu

The permission below is for the reproduction of material in Chapters 4.

AUTHOR AND END-USER REUSE POLICY

Our policies afford authors, their employers, and third parties the right to reuse the author's Accepted Manuscript (AM) or the final publisher Version of Record (VoR) of the article as outlined below:

Reuse purpose	Article version that can be used under:		
	Copyright Transfer	Open Access Publishing Agreement	CC BY License
Reproduction by authors in a compilation or for teaching purposes short term	AM	VoR	VoR
Posting by authors on arXiv or other preprint servers after publication (posting of preprints before or during consideration is also allowed)	AM	VoR	VoR
Posting by authors on a non-commercial personal website or closed institutional repository (access to the repository is limited solely to the institutions' employees and direct affiliates (e.g., students, faculty), and the repository does not depend on payment for access, such as subscription or membership fees)	AM	VoR	VoR
Posting by authors on an open institutional repository or funder repository	AM after 12 month embargo	VoR	VoR
Reproduction by authors or third party users for non-commercial personal or academic purposes (includes the uses listed above and e.g. creation of derivative works, translation, text and data mining)	Authors as above, otherwise by permission only. Contact copyright@optica.org.	VoR	VoR
Any other purpose, including commercial reuse on such sites as ResearchGate, Academia.edu, etc. and/or for sales and marketing purposes	By permission only. Contact copyright@optica.org.	By permission only. Contact copyright@optica.org	VoR

The permission below is for the reproduction of material in Chapters 5.

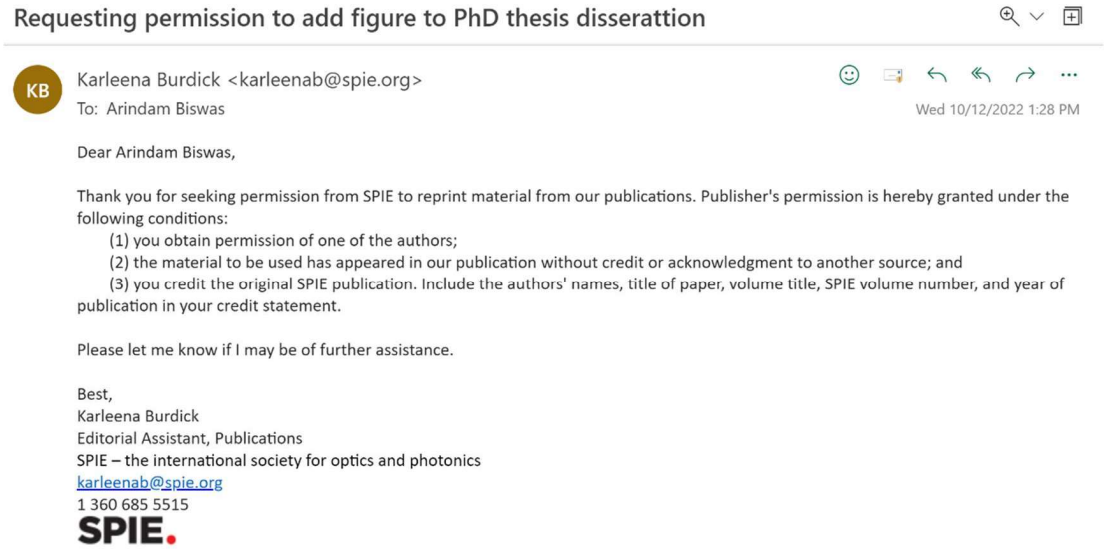

Requesting permission to add figure to PhD thesis disserattion

KB

Karleena Burdick <karleenab@spie.org>

To: Arindam Biswas

Wed 10/12/2022 1:28 PM

Dear Arindam Biswas,

Thank you for seeking permission from SPIE to reprint material from our publications. Publisher's permission is hereby granted under the following conditions:

(1) you obtain permission of one of the authors;

(2) the material to be used has appeared in our publication without credit or acknowledgment to another source; and

(3) you credit the original SPIE publication. Include the authors' names, title of paper, volume title, SPIE volume number, and year of publication in your credit statement.

Please let me know if I may be of further assistance.

Best,

Karleena Burdick

Editorial Assistant, Publications

SPIE – the international society for optics and photonics

karleenab@spie.org

1 360 685 5515

SPIE.

Appendix B: IRB Approval

The copy of IRB approval for the research conducted on this dissertation is attached below.

APPROVAL

November 30, 2021

Ashwin Parthasarathy
4202 E Fowler Ave
ENB 118
Tampa, FL 33620

Dear Dr. Ashwin Parthasarathy:

On 11/16/2021, the IRB reviewed and approved the following protocol:

Application Type:	Continuing Review
IRB ID:	Pro00039832_CR000002
Review Type:	Committee
Title:	Noninvasive monitoring of tissue hemodynamics with diffuse optical techniques
Funding:	None
IND, IDE, or HDE:	None
Approved Protocol and Consent:	• Omnibus_IRB_V2_2_CleanCopy.pdf; • Omnibus Informed Consent V3 Clean Copy.pdf; Approved study documents can be found under the 'Documents' tab in the main study workspace. Use the stamped consent found under the 'Last Finalized' column under the 'Documents' tab.

The IRB approved the protocol from 11/17/2021 to 11/17/2022. Within 45 days of 11/17/2022, submit a continuing review/study closure request in BullsIRB by clicking Create Modification/CR.

If continuing review approval is not granted before the expiration date of 11/17/2022, approval of this protocol expires on that date.

In conducting this protocol you are required to follow the requirements listed in the INVESTIGATOR MANUAL (HRP-103).

UNIVERSITY of SOUTH FLORIDA

Sincerely,

Vanessa Ellis
IRB Manager

About the Author

Arindam Biswas is Doctoral Candidate in Electrical Engineering at the University of South Florida. He graduated with his B.Sc. in Electrical and Electronic Engineering in 2016 from Rajshahi University of Engineering and Technology, Bangladesh. He is an expert on circuit design, optics, and biomedical technologies.

In 2017, he started his Ph.D. in Electrical Engineering. His research focus was wearable optoelectronic system design for non-invasive, continuous hemodynamic measurement aimed at disease diagnostic (i.e., stroke, ICP, hydrocephalus, arterial disease, wound tracking, etc.). During his doctoral program, he led multiple research projects to successful completion and mentored interdisciplinary undergraduate and graduate students. His research work on low form factor deep tissue hemodynamic measurement have been recognized with few national awards which includes CADE innovation award 2021, Optica Technical Group Best Poster presentation award 2020 and Dissertation Fellowship by USF college of graduate studies.

His ambition is to lead a group of engineer and scientists to solve problem in biomedical space with focus in wearable technologies. To gain industry experience, during the summer of 2022, Arindam worked as a research engineer at Apple Inc. in their Touch Sensing Incubation R&D group. After graduation Arindam aims to hold a research and management position in a well reputed company. This experience would pave the way for his career as a leader in wearable and AI space.